

Syracuse University

SURFACE at Syracuse University

Dissertations - ALL

SURFACE at Syracuse University

5-12-2024

MULTIMODE METAMATERIAL RING RESONATOR AS AN ENTANGLING BUS FOR ARTIFICIAL ATOMS

Tianna Carroll
Syracuse University

Follow this and additional works at: <https://surface.syr.edu/etd>



Part of the [Quantum Physics Commons](#)

Recommended Citation

Carroll, Tianna, "MULTIMODE METAMATERIAL RING RESONATOR AS AN ENTANGLING BUS FOR ARTIFICIAL ATOMS" (2024). *Dissertations - ALL*. 1898.
<https://surface.syr.edu/etd/1898>

This Dissertation is brought to you for free and open access by the SURFACE at Syracuse University at SURFACE at Syracuse University. It has been accepted for inclusion in Dissertations - ALL by an authorized administrator of SURFACE at Syracuse University. For more information, please contact surface@syr.edu.

ABSTRACT

Circuit quantum electrodynamics (cQED) systems with superconducting qubits coupled to linear microwave resonators are a prominent platform for realizing scalable quantum information processors. Combining cQED architectures with multimode resonators leads to a broad set of applications for performing analog quantum simulation, implementing dense quantum memory, and generating multimode entangled states between physically distant qubits. Microwave resonators in cQED are typically formed from distributed transmission lines that exhibit conventional dispersion with harmonic mode spacing; in such systems, usually only a single resonant mode can be strongly coupled to a qubit. Superconducting metamaterial resonators comprised of lumped circuit elements can be designed to produce a left-handed dispersion that results in a dense mode structure in the typical frequency range for operating superconducting qubits, thus allowing for a qubit to couple strongly to multiple modes simultaneously. Forming these metamaterial structures into a ring with qubits coupled at certain points around the ring results in a multi-mode bus with a compact physical footprint. In this thesis, we present a review of the design and fabrication of superconducting left-handed metamaterial ring resonators. We show, through low-temperature measurements, that when we couple two flux-tunable transmon qubits to such a ring resonator, the system shows extreme versatility in coupling parameters due to the unique wave structure of the modes in the ring. We measure and model the interactions between the qubits and the ring resonator modes, as well as the inter-qubit entangling interactions mediated by the multimode system. We describe how this platform could be used to implement two-qubit gates and generate entanglement between physically distant qubits.

**MULTIMODE METAMATERIAL RING
RESONATOR AS AN ENTANGLING BUS FOR
ARTIFICIAL ATOMS**

By

Tianna McBroom-Carroll

BS, University of Missouri-St. Louis, 2018

DISSERTATION

SUBMITTED IN PARTIAL FULFILLMENT OF THE REQUIREMENTS

FOR THE DEGREE OF

DOCTOR OF PHILOSOPHY IN PHYSICS

Syracuse University

May 2024

Copyright © Tianna McBroom-Carroll, 2024
All rights reserved.

ACKNOWLEDGMENTS

First, I would like to acknowledge my advisor, Prof. Britton Plourde. His patience in answering even the most mundane question has been invaluable. I am incredibly grateful for his mentorship and guidance as he has allowed me to explore problems, while never allowing me to get lost along the way.

I am thankful to my predecessor, Dr. Indrajeet, for the passing of knowledge on all facets of the metamaterial project. Thank you to my collaborators, Dr. Mohammad Ansari, Arne Schlabe, and Dr. Xuexin Xu for your indispensable work on the theory aspects of the ring resonator project. I thank Dr. Matt Lahaye and the team at the Air Force Research Lab for their stimulating discussions. I thank Brad Cole for his work on the metamaterial project and his hand in fabricating devices. I wish the best to my colleague, Manabputra, as he works on the next phase of the metamaterial project. A special thanks to the Syracuse machine shop; without Phil Arnold and David Pratt, no research would have been done.

I am fortunate to have had excellent mentorship provided by Dr. Yebin Liu, Dr. Jaseung Ku, and Dr. Caleb, Jordan. I am grateful to Andrew Ballard for the long days training me how to cool down the wet dilution refrigerator, and the many hours we spent making repairs. Many thanks to my fellow lab mates; to Dr. Kenneth Dodge for reminding me to take a break, to Dr. Vito Iaia for his wisdom, to Clayton Larson and Eric Yelton for bringing some sunshine and chaos to the sub-basement, and to Kiichi for his independence and work ethic.

To my peers with whom I started graduate school, and with whom I built a community, thank you.

Thank you to my family; to my mom, dad, and my sisters, who have supported and encouraged me.

Finally, and most importantly, thank you to my husband, Louis Carroll. I could not have done it without you.

Contents

List of Tables	viii
List of Figures	xvii
Acknowledgments	i
	ii
1 Introduction	1
2 Quantum Information Processing	6
2.1 Qubits	7
2.2 One-qubit gates	8
2.3 Two-qubit gates	9
2.3.1 CNOT gate	9
2.3.2 CZ gate	10
2.3.3 i SWAP gate	10
3 Superconducting circuit quantum electrodynamics	12
3.1 Superconducting Qubits	12
3.1.1 Josephson junctions	13
3.1.2 Transmons	16
3.1.3 Floating-style, flux-tunable transmons	17
3.2 Circuit Quantum Electrodynamics	18
3.2.1 Jaynes-Cummings Hamiltonian	19
3.3 Superconducting cavities	22
3.3.1 Transmission line quarter-wave resonator	23

3.4	Scattering parameters	27
3.5	Mapping the qubit state to the cavity state	28
3.6	Qubit decoherence	29
3.7	Two-qubit interactions	32
3.7.1	Exchange coupling	33
3.7.2	ZZ Interaction	35
4	Left-handed transmission line resonators	38
4.1	Metamaterials	39
4.2	Right-handed transmission line (RH TL)	42
4.3	Left-handed transmission lines (LH TL)	44
4.3.1	Resonators formed from metamaterials	46
4.3.2	Stray reactance from lumped circuit elements in LH TL	48
4.4	Coupling transmon qubits to a LH TL resonator	49
5	Left-handed metamaterial ring resonators	53
5.1	Left-handed metamaterial ring resonator	54
5.1.1	Stray reactance from lumped circuit elements	56
5.1.2	Stray reactance from wirebonds	57
5.2	Coupling transmon qubits to a ring resonator	60
5.2.1	Theoretical derivation of Hamiltonian and g -coupling	61
6	Device Design	68
6.1	Ring resonator design	68
6.2	Qubit design	70
6.3	Device layout	73
6.4	Fabrication details	75
6.5	Measurement setup	75
7	Ring resonator mode structure and g-coupling	79
7.1	Measurement of ring resonator spectrum	79
7.2	Measurement of g -coupling	82
7.3	Extraction of g -coupling from spectroscopy	83
7.4	Theoretical g -coupling	85

8	<i>J</i>-coupling between qubits	87
8.1	Measurement of J	88
8.2	Extraction of J -coupling from spectroscopy	89
8.3	Non-perturbative J calculations	90
8.4	Predicting the sign of J	92
9	ZZ Interaction between qubits	94
9.1	Measurement of the ZZ interaction	94
9.2	Extraction of ZZ	96
9.3	Theoretical ZZ calculations	97
10	Future and ongoing work	100
10.1	Implementing a two-qubit gate with a ring resonator bus	100
10.2	Coupling in more qubits to the ring resonator bus	101
10.3	Symmetry-breaking around the ring resonator	102

List of Tables

1	Ring resonator cell parameters obtained via finite element simulation. Unit cell capacitance C_L , total center disk capacitance C_D , and coupling capacitance C_C of the ring to external feedline are obtained using Ansys Q3D software. Unit cell inductance and wirebond inductance, L_L determined using InductEx software. The stray inductance and capacitance, L_R and C_R , were found using Sonnet software to identify the self resonances of the lumped-element unit-cell structures. The values in the theory column come from modeling of the device and adjusting parameters to match the measured ring resonator spectrum. The discrepancy between the theoretical and simulated values for L_L are likely due to imperfect grounding and approximations used in estimating the inductive contributions of the wirebonds based on extracted lengths from microscope images.	69
2	Parameters for two transmon qubits, Q_A and Q_B . Method of determination for each parameter is given in the text.	71
3	Magnitude of qubit-ring resonator g -coupling parameters for Q_A and Q_B	86
4	Magnitude of qubit-ring resonator g -coupling parameters and parity for Q_A and Q_B . Here, the parity of the g -coupling values between the two qubits is determined by comparing measured versus perturbative theoretical calculations of the exchange coupling for Q_A and Q_B , as described in the main text.	91

List of Figures

1	Bloch sphere representation of the quantum state $ \psi\rangle$	7
2	The <i>controlled</i> NOT (CNOT) gate and <i>controlled</i> phase (CZ or CPHASE) gate circuit representations and truth tables for the two-qubit basis. Figure modified from [1].	9
3	(a) Parallel <i>LC</i> -circuit realization of a quantum harmonic oscillator (QHO), with L_r and C_r being the circuit inductance and capacitance. (b) Quadratic energy potential well for the QHO with respect to the superconducting phase across the inductor, with evenly spaced energy eigenvalues separated by $\hbar\omega_r$ shown with blue horizontal lines. Squared moduli of the energy wavefunctions are shown in light blue. (c) Circuit comprised of a Josephson junction element with non-linear inductance L_J and capacitance C_J in parallel with a shunt capacitance C_S . (d) Cosine energy potential for the circuit shown in (c). Horizontal red lines show the unevenly spaced eigenenergies of the system with yellow lines showing the squared moduli of the eigenfunctions. The space between the $ 0\rangle$ and the $ 1\rangle$ state is given by $\hbar\omega_{01}$ and is not equal to the spacing between the $ 1\rangle$ and the $ 2\rangle$ states given by $\hbar\omega_{12}$	14
4	Schematic of a Josephson junction. The superconducting electrodes shown in gray are comprised of aluminum and are separated by a thin AlO_x barrier shown in blue. The macroscopic state of the Cooper pairs for each side of the junction are each given by the wavefunctions $ \Psi_L e^{i\phi_L}$ and $ \Psi_R e^{i\phi_R}$. Cooper pairs tunnel left to right with no dissipation in the presence of an applied current below the critical current with a phase difference $\varphi = \phi_L - \phi_R$	15

5	Eigenenergies E_m , for $m = 0, 1, 2, 3$ as a function of the effective offset charge n_g shown in black, red, blue, and green, respectively, for E_J/E_C ratios of (a) 1 (b) 5 (c) 10 and (d) 50. As the ratio of E_J/E_C increases, the charge dispersion decreases, making the qubit insensitive to fluctuations in offset charge for sufficiently large E_J/E_C	16
6	Circuit diagram of a flux-tunable asymmetric transmon. The gate voltage V_g is coupled via gate capacitor C_g . A dc SQUID, comprised of two asymmetric Josephson junctions with Josephson energies E_{J1} , E_{J2} with associated capacitances C_{J1} , C_{J2} , is inductively coupled to a current-bias line. The dc SQUID is shunted by capacitor C_S	17
7	Avoided level crossing in the transition frequency for a system comprised of a tunable frequency qubit and a microwave cavity shown with solid black lines. The state vector is written as $ q; c\rangle$, where q denotes the qubit state and c denotes the cavity state. The uncoupled $0 \rightarrow 1$ base transition frequency of the qubit, ω_q , is shown with a red dotted line. The uncoupled cavity frequency, ω_c , is shown with a black dashed line.	19
8	Geometry of a CPW. The center conductor has width w , and the gaps have width s . The film has a thickness t , and the substrate has a thickness h	22
9	(a) Quarter-wave resonator comprised of a CPW transmission line with one end open and one end shorted to ground. (b) Near resonance, the quarter-wave CPW can be modeled by a simple driven parallel RLC circuit.	23
10	(a) Quarter-wave CPW resonator inductively coupled to a CPW feedline. (b) Circuit modeling a quarter-wave CPW near resonance as a parallel RLC circuit inductively coupled to an external load. The inductance L of the RLC circuit is split such that $L = L_r + L_m$, where L_r comprises the majority of the inductance, and L_m comprises the portion of the total inductance that contributes to the coupling. The mutual inductance between the RLC oscillator and external load resistance R_0 is given by M . (c) Equivalent circuit model with the mutual coupling replaced with inductive elements.	26

11	Transmitted (a) amplitude and (b) phase for a cavity resonator coupled to a transmon qubit showing qubit-state dependent cavity frequency shift. The renormalized cavity frequency ω'_c , shown with a gray dashed line, is shifted by $\pm\chi$ when the qubit is in the ground state $ 0\rangle$ (excited state $ 1\rangle$), shown with blue (red) lines.	28
12	Longitudinal relaxation measurement for a transmon qubit as a function of time. Measured data is shown in red circles. Exponential decay fit is shown with a solid black line. The pulse sequence is shown as an inset. The measurement sequence consists of applying an X gate on the qubit, calibrated to excite the qubit to the $ 1\rangle$ state, then implementing a variable delay before reading out the qubit state. The x-axis is the delay time τ	29
13	Measured one-state population as a function of delay time, τ , for Ramsey interferometry pulse sequence depicted. Red circles show measured data and black line shows exponentially decaying sinusoidal function fit. For this measurement, the midpoint of the oscillations is below 0.5, suggesting that the calibration of the X pulse results in a one-state probability of less than unity.	30
14	One-state occupation for a Ramsey interferometry measurement as a function of detuning frequency, δ and delay time between $X/2$ pulses. The dashed line shows the zero detuning point.	31
15	Measured one-state population as a function of delay time, τ , for Hahn echo pulse sequence depicted. Red circles show measured data and black line shows exponential decay fit.	32
16	Theoretical plot of an avoided level crossing in the transition frequency of two qubits, Q_A and Q_B , when the transition frequency of Q_A is tuned through the fixed transition frequency of Q_B . The uncoupled $0 \rightarrow 1$ transition frequency of $Q_A(Q_B)$, $f_A(f_B)$, is shown with a red(blue) dotted line. The avoided crossing between Q_A and Q_B is shown in black.	33

17	Theoretical energy spectrum for two transmon qubits coupled via a resonator bus at frequency $\omega_c/2\pi$ as a function of the magnetic flux on one of the qubits, Q_A , while the other qubit, Q_B , is fixed with its $0 \rightarrow 1$ frequency near 4 GHz. (a) Spectrum showing $ 01\rangle$, $ 10\rangle$, $ 11\rangle$, $ 02\rangle$, and $ 20\rangle$ in blue, red, purple, teal, and orange respectively. Flux location on Q_A at which i SWAP and CZ gates may be implemented are indicated. (b) Zoom in of the $ 20\rangle$, $ 11\rangle$ avoided crossing. Gray dashed line shows $ 10\rangle + 01\rangle$. The ZZ interaction strength is indicated by ζ/\hbar .	36
18	Electromagnetic waves incident on the boundary between two materials. \mathbf{S} , \mathbf{k} are shown in blue for the wave incident θ_0 from normal, \mathbf{S}' , \mathbf{k}' are shown in red for the the reflected wave θ_1 from normal, and \mathbf{S}'' , \mathbf{k}'' are shown in green for the refracted wave θ_2 from normal. The first material has positive permittivity ϵ_1 and permeability μ_1 , and the second has (a) positive permittivity ϵ_2 and permeability μ_2 or (b) negative permittivity ϵ_2 and permeability μ_2 . Figure is adapted from Ref. [2].	39
19	(a) Equivalent lumped-element CPW circuit comprised of series inductors L_R shunted by capacitors to ground C_R . (b) Voltages and currents for a single unit cell of length Δx .	42
20	Right-handed dispersion relation as a function of normalized wavenumber shown with a solid blue line. The maximum resonance frequency, given by ω_{UV} , is shown with a dashed blue line.	44
21	(a) LH TL circuit model comprised of series capacitors C_L shunted to ground by inductors L_L . (b) Definition of current and voltage for a LH TL at cell n .	44
22	Dispersion relation for a discrete RH TL and LH TL as a function of the normalized absolute value of the wavenumber shown in blue and orange, respectively. The infrared cutoff frequency ω_{IR} for the LH TL is show with a orange dashed line. The ultraviolet cutoff frequency ω_{UV} for the RH TL is shown with a blue dashed line.	46

23	(a) LHTL resonator with 24 unit cells comprised of series capacitors C_L and parallel inductors L_L and input and output capacitances C_C at each end of the LHL. (b) Resonance frequency as a function of mode number for the 24-cell LHTL resonator. Orange data points show the discrete resonance frequency for each mode.	47
24	Circuit diagram of a composite LHRHTL, where the left-handed lumped circuit elements are C_L and L_L and the stray reactances that form the right-handed circuit are C_R and L_R	48
25	Dispersion relation for a discrete RHTL and LHTL as a function of normalized mode number shown in blue and orange, respectively. The infrared cutoff frequency ω_{IR} for the LHTL is show with an orange dashed line. The self-resonance frequencies for the lumped-element capacitors $\omega_C/2\pi$ and inductors $\omega_L/2\pi$ create a band gap with no propagating wave solutions, shown with gray dashed lines.	50
26	Voltage in arbitrary units as a function of node position for a 24-cell LHTL resonator for modes 1, 12, and 23, shown in orange, green, and blue, respectively, with an arbitrary offset in voltage added between modes. The circles correspond to the voltage amplitude of the standing wave at a given node across the LHTL resonator. The only node position at which the modes would be maximally coupled to a qubit correspond to the $n = 0$ and $n = 25$ node positions of the input/output capacitors to the LHTL resonator.	51
27	Left-handed metamaterial ring resonator with 24 unit cells with cell length Δx , comprised of series capacitors C_L and parallel inductors L_L	54
28	Resonance frequency as a function of mode number for a 24-cell LHTL metamaterial ring resonator. Orange data points show the discrete resonance frequency for each mode. Gray lines connect degenerate resonance modes, only differentiable by phase in an ideal ring resonator	55
29	Ring resonator circuit with 24 cells, including parasitic stray reactances. The inset shows a single cell comprised of a series capacitor C_L and inductor L_R shunted to ground by parallel inductor L_L and capacitor C_R	57

30	Dispersion relation for a composite left-handed/right-handed ring resonator as a function of normalized mode number with left-handed branches and right-handed branches shown in solid blue and orange lines, respectively. The IR-cutoff frequency ω_{IR} for the ring resonator is shown with an orange dotted line. Orange dashed lines show pure left-handed ring resonator dispersion. The self-resonance of the lumped-element capacitors and inductors, ω_L and ω_C , are shown with gray, dotted lines.	58
31	Single-cell circuit schematics for a ring resonator with (c), (d) and without (a), (b) stray inductance from wirebonds and with (b), (d) and without (a), (c) stray parasitic reactance included for the lumped circuit elements.	59
32	Ring resonator schematic and mode structure for two pairs of degenerate ring resonator modes. The ring resonator model consists of 24 unit cells, shown with gray squares, with each cell containing a capacitor shunted to ground by two inductors. One pair of even (odd) modes with $k\Delta x = 10\frac{2\pi}{N}$ is shown in solid (dashed) orange lines, labeled $m_E^{(10)}(m_O^{(10)})$; a second pair with $k\Delta x = 5\frac{2\pi}{N}$ is depicted with solid (dashed) green lines, labeled $m_E^{(5)}(m_O^{(5)})$. The coupling strength of Q_A and Q_B to each mode is determined by the amplitude of the wave at the cell where the qubit is capacitively coupled to the resonator. . . .	60
33	Theoretical g -coupling values for Q_A and Q_B , coupled to a hypothetical 240-cell ring resonator with qubit separation $n_{AB} = 6$. Simulated data points at which the coupling for Q_A , $g_i^A/2\pi$, and for Q_B , $g_i^B/2\pi$, share the same sign for a given mode are shown in purple. Points at which the g_i^A and g_i^B coupling to Q_A and Q_B , respectively, have opposite signs are shown in gray.	67
34	Characteristic transmon curve fit for f_{01} transition of (a) Q_A and (b) Q_B , shown in solid red and blue lines, respectively. Red(blue) circles show spectroscopy data for $Q_A(Q_B)$ used in the fit. Gray, dashed lines denote bare ring resonator mode frequencies.	72

35	Full circuit schematic. Microwave readout is performed via right-handed transmission lines labeled R_{in}/R_{out} and F_{in}/F_{out} in green and yellow, respectively. The 24-cell ring-resonator circuit is shown in orange. Capacitively coupled qubits, Q_A and Q_B , are shown in red and blue, respectively, and are separated by a distance of $n_{AB} = 6$. Qubit readout cavities are comprised of quarter-wave coplanar waveguide resonators.	73
36	(a) Chip layout for metamaterial ring-resonator device. (b-e) Optical micrographs of device with false-color highlighting. (f) SEM image of Josephson junction in qubit.	74
37	Schematic of the wiring within the dilution refrigerator.	76
38	Wiring diagram for standard heterodyne setup used for readout.	78
39	Measured ring resonator spectrum.	80
40	(a) Image of wirebonds used for grounding the device, as well as attachments to signal traces. (b) GDS of device layout including approximate wirebond positions shown with white lines. (c) Theoretical circuit model accounting for aluminum wirebonds.	81
41	Measured ring resonator mode frequencies are shown with gray dashed lines. Theoretical mode frequencies are shown with green dashed-dotted lines when stray inductance due to wirebonds is not included and any degeneracy lifting is due to the qubits or feedline. Solid blue lines show large degeneracy lifting effect of wirebonds on the ring resonator mode frequencies.	82
42	Vacuum Rabi splittings measured via R_{in}/R_{out} , between three ring resonator modes and (a) Q_A , (b) Q_B . Dashed lines in red (blue) show fits to splitting data for Q_A (Q_B) obtained from reduced Hamiltonian including one qubit and the three modes. Horizontal dotted lines show dressed mode frequencies. (c-f) Splittings and reduced Hamiltonian fits for two single modes for each qubit. For all measurements, the spectator qubit is fixed at its upper flux insensitive sweet spot ($\Phi_q/\Phi_0 = 0$). As shown in (c), Q_A has effectively zero coupling to the ring resonator mode at 4.553 GHz, while (d) shows Q_B has a coupling strength of 26.6 MHz.	83

43	Extracted and theoretical $ g_i^q /2\pi$ values for each ring-resonator mode i . Error bars on experimental data computed from 95% confidence intervals in g -coupling fits. Vertical dashed lines show bare ring resonator mode frequencies.	85
44	J -coupling spectroscopy data as a function of flux on Q_A . Red dashed lines show fits to splitting data from effective Hamiltonian. The blue dashed line shows the fixed frequency of Q_B . (a) Avoided level crossing between Q_A and Q_B at 4.2 GHz. (b) Avoided level crossing between Q_A and Q_B at 5.5 GHz.	88
45	Experimental and theoretical J -coupling values as a function of frequency. Diamonds show experimental values for $J/2\pi$, with error bars computed from 95% confidence intervals in fits. Gray lines and purple crosses show theoretical $J/2\pi$ values calculated using Schrieffer-Wolff and Least Action, respectively. Dotted vertical lines show bare ring-resonator mode frequencies.	90
46	Comparison of experimental and theoretical J -coupling values as a function of frequency when g -coupling parity for Q_A and Q_B is changed for a single mode. Diamonds show experimental values for $J/2\pi$, with error bars computed from 95% confidence intervals in fits. Dotted gray vertical lines show bare ring-resonator mode frequencies. (a) Gray lines show theoretical $J/2\pi$ values calculated using Schrieffer-Wolff. (b) Red dotted line denotes ring resonator mode that has swapped parity of the g -coupling for Q_A and Q_B . Red lines show the theoretical $J/2\pi$ values calculated using Schrieffer-Wolff when the g -coupling is swapped for this single ring resonator mode.	92

- 47 Measurement sequence for obtaining ZZ interaction strength. (a) A Ramsey pulse sequence is performed on Q_A at variable drive frequencies while Q_B is idle. (b) A second Ramsey fringe measurement is performed on Q_A after a π -pulse is applied to Q_B . (c) Horizontal slices of Ramsey fringe measurements are fit to obtain the Ramsey oscillation frequency, f_{Ramsey} , at each drive frequency. The ZZ interaction, denoted $\zeta/2\pi$, is the change in the dressed transition frequency for Q_A , \tilde{f}_A , depending on whether Q_B is in the ground or excited state. (d-f) Three example plots of Ramsey frequency as a function of Q_A drive frequency (f_A drive) for different Q_A bias points with linear fit lines for ZZ measurements taken when Q_B is at 5.04 GHz. 95
- 48 $\zeta/2\pi$ as a function of the dressed frequency of Q_A , \tilde{f}_A , when the dressed frequency of Q_B , \tilde{f}_B , is (a) 5.04 GHz, (b) 5.81 GHz. Measured and theoretical values are shown as diamonds and gray lines, respectively. Vertical dashed lines in blue and gray show the location of Q_B and the ring resonator modes in frequency space, respectively. Insets show Ramsey oscillation frequency fit data as a function of Q_A drive frequency taken from Ramsey fringe measurements. Red data points and fit lines generated by performing a simple Ramsey pulse sequence (shown in red box) on Q_A at multiple detunings and extracting oscillation frequency. Data resulting from pulse sequence in which a π -pulse is applied to Q_B , followed by a Ramsey on Q_A (shown in purple box). Error bars computed from 95% confidence intervals for both Ramsey oscillation fits. Intersection of fit lines where Ramsey oscillation frequency vanishes indicate Q_A frequency, from which we compute $\zeta/2\pi$. 97
- 49 Uncertainty in theoretical ZZ values due to energy level anti-crossings. (a) Experimental and theoretical ZZ interaction $\zeta/2\pi$ as a function of \tilde{f}_A shown with diamonds and grey lines, respectively, with shading added to show region of uncertainty. (b) Multi-photon energies as a function of \tilde{f}_A . The light grey region denotes uncertainty in the theoretical ZZ calculation. The discontinuity of the ZZ interaction around 5.25 GHz is caused by an anti-crossing of the $|11\rangle$ and $|20\rangle$ states. 98

Chapter 1

Introduction

Quantum computing is an emergent field that leverages quantum mechanics to solve complex problems that are not practically solvable by a classical computer. The modern premise of classical computation was developed by Alan Turing in 1936 when he conceptualized an abstract machine, now called the Turing machine for his namesake, that could be programmed to perform a task. He asserted, in what is now known as the Church-Turing thesis, that there exists a universal Turing machine that could simulate any other Turing machine and completely capture the meaning of algorithmically performing a task [3]. The premise of the Turing machine laid the groundwork for the first electrical computers. The fundamental unit of computation in a modern classical computer is the transistor bit, a digital semiconducting device that encodes a binary bit of information. The rapid scaling of the processing power of classical computers was codified by Moore's law in 1965, which predicted that, for constant cost, computational power would double approximately once every two years [4]. Moore's Law held true for decades after his prediction [5]. Over time, transistors have shrunk in size and the density of transistors on a processing chip has risen exponentially. Single transistors are now on the nanometer scale, and face fabrication limitations and undesired quantum effects that make it challenging to scale transistor size down or, equivalently, scale the density higher. Even as these limitations arise, innovations in transistors, such as fabricating 3D stacked arrays of transistors using complementary metal oxide semiconductor (CMOS) methods [6], mean that such a fundamental limit has not been reached. But, despite these innovations, the quantum effects and scaling of transistors remains a challenge. There are also fundamental limitations on

problems that are solvable by classical computers. Quantum computers are being developed as an alternative to classical computers for solving specific classes of problems that are particularly challenging for classical computers.

Early conceptualization of a quantum computer began in the 1980s [7]. Richard Feynman gave a talk in 1981 in which he proposed using a quantum computer to solve certain difficult problems that are too complex for classical computers to solve [8]. In 1985, David Deutsch formally developed the notion of a quantum computer and posed the question of what advantage a quantum computer could practically have over classical computers [9]. One early conceptual answer to this question was developed by Peter Shor in 1994, who showed that factoring large numbers into primes, a problem where the computational time scales exponentially with the size of the number for a classical computer, could be solved in polynomial time with a quantum computer [10]. Physical implementations of a quantum computer utilize qubits, or quantum bits, in place of classical transistor bits. The field is still relatively young, and there are many competing platforms working towards developing a fault-tolerant quantum computer capable of implementing algorithms like the one proposed by Shor. Qubits have been implemented in quantum systems using a range of systems, including superconducting qubits [11, 12, 13], ion traps [14], photons [15, 16], neutral atoms [17, 18], and semiconductors [19, 20]. Superconducting qubits are a promising platform because of their compatibility with existing microfabrication techniques. Superconducting qubits are fabricated as integrated circuits that can have wires directly connected to quantum processor chips allowing for fast gate times and readout. These properties have made superconducting qubits a focus of many large industrial computing labs and state-of-the-art quantum processors have been made with more than 1000 qubits on a single chip [21]. In 2019, a processor with 53 operational qubits, called Sycamore, was shown to perform a computation on the scale of minutes that would require at least days for the fastest known classical algorithm at the time running on the most powerful existing supercomputer to solve [22]. This experimental demonstration of quantum supremacy is an important milestone in the field of quantum computing, but this experiment also shows the current limitations of quantum computation. The infidelities compound as the number of qubits in a quantum processor increases, meaning that for an experiment with 53 qubits, millions of repetitions are needed to obtain statistically useful output. In the current era of quantum computing, the noisy

intermediate-scale quantum (NISQ) era [7], initial steps towards implementing quantum error correction have been made, but the limited current state-of-the-art qubit coherence makes implementation of fault-tolerant quantum computation a daunting challenge [23]. Additionally, quantum algorithms are often derived under the assumption that gates can be implemented between arbitrary pairs of qubits in a quantum processor, but scaling quantum computers to allow for all-to-all connectivity between large numbers of qubits is a challenge, particularly for most solid-state qubit systems.

Circuit Quantum Electrodynamics (cQED) involves the coupling of circuit-based qubits to quantized photonic modes in linear resonant structures. In cQED, waveguide resonators are commonly used for readout of artificial atom qubits, and in some cases, as bus cavities for coupling between qubits [24, 25]. Variants on this architecture are the dominant paradigm for current superconductor-based quantum processors. The superconducting resonators are often formed from planar transmission lines with a single mode near the frequency range of the qubits. In general, coupling between superconducting qubits and resonators is designed to be in the strong regime, where the coupling strength of the qubit to a mode, g , is larger than the cavity and qubit linewidths. Coupling can also be scaled to the ultra-strong regime, such that the coupling strength is comparable to the transition energy scales of the cavity or qubits [26, 27]. Implementing a single resonance cavity in the frequency range of the qubit requires a physically large footprint of several millimeters. Utilizing an even larger physical footprint, devices with dense mode spectra near the qubit frequency range have been realized using ultra-long resonators [28]. Superstrong coupling is achievable in a multimode system if the modes are sufficiently closely grouped and a single qubit is engineered to couple strongly to multiple modes simultaneously [29]. These multimode cQED systems have been studied for implementing quantum memories [30] and quantum simulations [31, 32].

Metamaterials, formed from lumped-element inductors and capacitors, allow for the implementation of transmission lines with unconventional wave dispersion. In the case of left-handed dispersion [33], the wave frequency is a falling function of wavenumber above an infrared cutoff frequency f_{IR} , below which waves are unable to propagate [34, 35]. In the context of cQED, left-handed metamaterials produce a dense spectrum of orthogonal microwave modes above f_{IR} , which can be engineered

to fall in the frequency range of conventional superconducting qubits [36]. Superconducting qubits coupled to a resonator formed from a left-handed metamaterial have predictable coupling to the dense set of resonant modes [37].

Ring resonators have been used in integrated photonics systems to form compact optical resonances, called whispering gallery modes, for a broad range of applications including microwave-optical transducers, microwave frequency combs, and multimode nonlinear optics [38, 39, 40, 41, 42]. Superconducting ring resonators with right-handed dispersion have also been used in cQED applications for implementing non-nearest neighbor qubit coupling for multiqubit systems [43]. These superconducting ring resonators require a large footprint, as the circumference of the ring must be a minimum of one wavelength of the resonant frequency.

In this thesis, a superconducting left-handed metamaterial ring resonator is described, formed from a left-handed metamaterial transmission line with two transmon qubits coupled at different points around the ring. Detailed modeling of the standing-wave structure and degeneracy breaking in the ring resonator is performed, allowing the coupling energy scales between the qubits and each ring resonator mode to be predicted [44]. The multimode coupling between the qubits with the ring resonator serving as a bus results in significant variations in both the transverse exchange coupling between the qubits as well as higher order ZZ interactions as the qubits are tuned between different frequency regimes. This architecture has broad applications for quantum random access memory, multipartite entanglement, and, as we will describe, as an entangling bus for performing two-qubit gates on physically distant qubits. In the next chapter, Ch. 2, qubits and quantum information are described from an abstract perspective, with an explanation of quantum logic and quantum gates for one- and two-qubit systems. In Chapter 3, a practical description of a qubit realized with a superconducting transmon is given, as well as a discussion of cQED and superconducting cavities. Chapter 4 introduces the concept of a metamaterial fabricated using lumped circuit elements, and shows that some metamaterials exhibit left-handed dispersion. Following this general discussion of metamaterials, in Ch. 5, a left-handed metamaterial ring resonator is introduced and an expression is derived for the coupling of two transmon qubits to the modes of the ring resonator. The next chapter, Ch. 6 describes the device design, while Ch. 7, Ch. 8, and Ch. 9 detail the measurement and analysis of the device. Finally, in Ch. 10, a discussion of future

work and applications is presented.

Chapter 2

Quantum Information Processing

Since its conceptualization in the 1980s, quantum computing has expanded into an interdisciplinary pursuit studied by countless research programs and organizations. Quantum computing can potentially solve certain problems that are intractable on classical supercomputers including factoring large prime numbers, which has relevance for cryptography and data security, as well as simulating quantum systems in fields such as quantum chemistry and pharmaceutical sciences. At the heart of quantum computing's transformative technology lie qubits. In classical computing, bits are the fundamental unit for information processing, and these bits must be manipulated by gates. Qubits are the fundamental units of a quantum computer, and the gates used to manipulate the state of the qubit must also preserve the coherence while being arranged in such a way to take advantage of superposition states, quantum interference, and entanglement to do meaningful computation [5, 8]. To obtain information about a quantum system, we must have a control architecture for performing these operations on qubits.

This chapter deals in broad strokes with the fundamentals of quantum computation for systems comprising one or two qubits. We will discuss the concept of a qubit and the gates we can implement to control one- and two-qubit systems. We focus on one- and two-qubit gates because a universal quantum processor can be implemented with the ability to do arbitrary single-qubit gates between pairs of qubits as well as entangling two-qubit gates between pairs of qubits.

2.1 Qubits

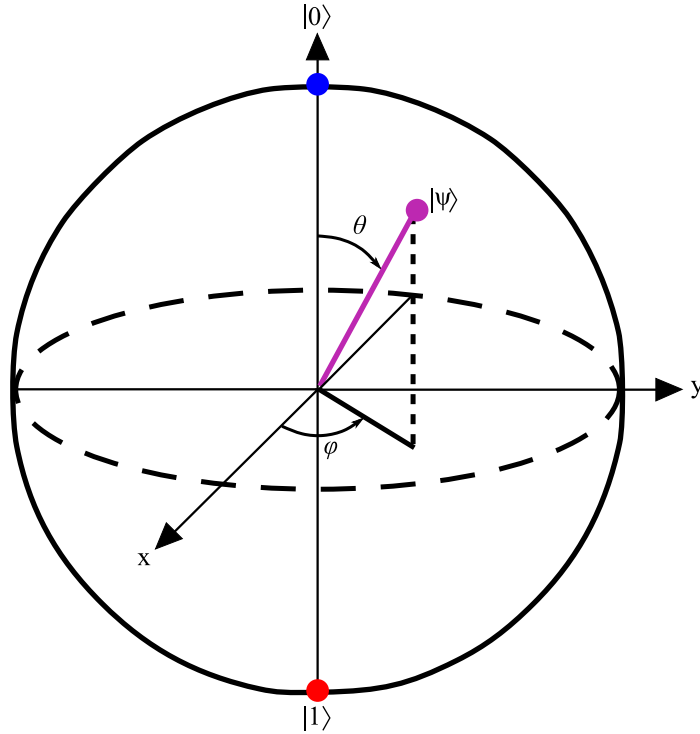


Figure 1: Bloch sphere representation of the quantum state $|\psi\rangle$.

The realization of a quantum computer requires a quantum equivalent to the digital transducer bit used in classical computers. The quantum bit, or qubit, is a two-state system that allows for the quantum phenomenon of superposition. We can describe a coherent superposition of the two-state system as $|\psi\rangle = \alpha|0\rangle + \beta|1\rangle$, where the eigenstates $|0\rangle$ and $|1\rangle$ constitute the two states that comprise our computational basis and α and β are complex probability amplitudes, with the property $|\alpha|^2 + |\beta|^2 = 1$. Unlike the classical bit, which we can measure to be in the state 0 or 1, for the qubit we can only obtain the probability $|\alpha|^2$ ($|\beta|^2$) for a measurement to yield the result $|0\rangle$ ($|1\rangle$).

A useful representation of the qubit state is the Bloch sphere, which represents the qubit state as a vector on the unit sphere. An arbitrary qubit state is given by

$$|\psi\rangle = \cos\left(\frac{\theta}{2}\right)|0\rangle + e^{i\phi}\sin\left(\frac{\theta}{2}\right)|1\rangle, \quad (2.1)$$

where θ defines the polar angle and ϕ the azimuthal angle on the Bloch sphere, as

shown in Fig. 1. This representation is intuitive in its presentation of the qubit state. The two poles correspond to the two basis states, $|0\rangle$ and $|1\rangle$, and all other vector directions represent a superposition of states.

2.2 One-qubit gates

We use gates to implement logical transformations on our system. For a quantum computer, the only constraint on what constitutes a gate is that it must be described by a unitary matrix, U , such that $U^\dagger U = I$ [5].

One important set from an infinite number of one-qubit gates can be obtained from the Pauli matrices, given by

$$\sigma_x \equiv X \equiv \begin{pmatrix} 0 & 1 \\ 1 & 0 \end{pmatrix}, \quad (2.2)$$

$$\sigma_y \equiv Y \equiv \begin{pmatrix} 0 & -i \\ i & 0 \end{pmatrix}, \quad (2.3)$$

$$\sigma_z \equiv Z \equiv \begin{pmatrix} 1 & 0 \\ 0 & -1 \end{pmatrix}. \quad (2.4)$$

The Pauli matrices can generate a rotation of the qubit state vector on the Bloch Sphere. There is only one non-trivial gate that can be applied to a classical bit, the *NOT* gate, which results in a bit flip from either 0 to 1 or 1 to 0. The equivalent gate for a qubit is given by X , defined in Eq. (2.2). When an X gate operates on the qubit state, it results in a π -rotation about the x -axis of the Bloch sphere. Similarly, the Y and Z gates correspond to π -rotations around the y - and z -axes of the Bloch sphere, respectively.

Another significant one-qubit gate is the Hadamard, given by

$$H = \frac{1}{\sqrt{2}} \begin{pmatrix} 1 & 1 \\ 1 & -1 \end{pmatrix}. \quad (2.5)$$

The Hadamard gate turns $|0\rangle$ to the superposition state $(|0\rangle + |1\rangle)/\sqrt{2}$, and $|1\rangle$ to the superposition state $(|0\rangle - |1\rangle)/\sqrt{2}$. In terms of the Bloch sphere, this is equivalent to a $\pi/2$ -rotation about the y -axis followed by a π -rotation about the x -axis. By

preparing the qubits in a superposition state, it enables quantum interference effects to be used for quantum algorithms [5]. The implementation of quantum gates in practice depends on the particular physical qubits. In the next chapter, we will discuss how gates work for superconducting qubits.

2.3 Two-qubit gates

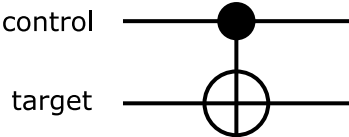
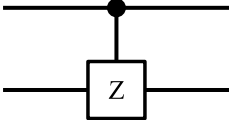
Gate	Circuit representation	Truth table										
CNOT		<table border="1"> <thead> <tr> <th>Input</th> <th>Output</th> </tr> </thead> <tbody> <tr> <td>$00\rangle$</td> <td>$00\rangle$</td> </tr> <tr> <td>$10\rangle$</td> <td>$11\rangle$</td> </tr> <tr> <td>$01\rangle$</td> <td>$01\rangle$</td> </tr> <tr> <td>$11\rangle$</td> <td>$10\rangle$</td> </tr> </tbody> </table>	Input	Output	$ 00\rangle$	$ 00\rangle$	$ 10\rangle$	$ 11\rangle$	$ 01\rangle$	$ 01\rangle$	$ 11\rangle$	$ 10\rangle$
Input	Output											
$ 00\rangle$	$ 00\rangle$											
$ 10\rangle$	$ 11\rangle$											
$ 01\rangle$	$ 01\rangle$											
$ 11\rangle$	$ 10\rangle$											
CZ		<table border="1"> <thead> <tr> <th>Input</th> <th>Output</th> </tr> </thead> <tbody> <tr> <td>$00\rangle$</td> <td>$00\rangle$</td> </tr> <tr> <td>$10\rangle$</td> <td>$10\rangle$</td> </tr> <tr> <td>$01\rangle$</td> <td>$01\rangle$</td> </tr> <tr> <td>$11\rangle$</td> <td>$- 11\rangle$</td> </tr> </tbody> </table>	Input	Output	$ 00\rangle$	$ 00\rangle$	$ 10\rangle$	$ 10\rangle$	$ 01\rangle$	$ 01\rangle$	$ 11\rangle$	$- 11\rangle$
Input	Output											
$ 00\rangle$	$ 00\rangle$											
$ 10\rangle$	$ 10\rangle$											
$ 01\rangle$	$ 01\rangle$											
$ 11\rangle$	$- 11\rangle$											

Figure 2: The *controlled* NOT (CNOT) gate and *controlled* phase (CZ or CPHASE) gate circuit representations and truth tables for the two-qubit basis. Figure modified from [1].

Let us expand our Hilbert space to deal with two-qubit logic that goes beyond simple combinations of single-qubit gates. There is a set of two-qubit gates called *controlled* operations in which one qubit is designated the control qubit and the other is the target on which an action is implemented. The state of the control qubit determines the effect of the action on the target qubit. The underlying principle of these gates is that they can be used to generate entanglement between two qubits [1].

2.3.1 CNOT gate

The prototypical *controlled* operation is the CNOT gate. Figure 2 shows the circuit model in which the control qubit is represented by the top line and the target qubit is represented by the bottom line. The truth table demonstrates the outcome of the

CNOT gate; the CNOT gate flips the state of the target qubit if and only if the control qubit is in the $|1\rangle$ state. The matrix representation of the CNOT gate is given by

$$CNOT = \begin{pmatrix} 1 & 0 & 0 & 0 \\ 0 & 1 & 0 & 0 \\ 0 & 0 & 0 & 1 \\ 0 & 0 & 1 & 0 \end{pmatrix}. \quad (2.6)$$

2.3.2 CZ gate

Figure 2 shows the circuit model for the CZ gate. As can be seen from the truth table, the outcome of the CZ gate is to introduce a phase rotation when both qubits are initially in the $|1\rangle$ state, and to do nothing otherwise; this means that the outcome of the CZ gate is symmetric. The matrix representation of the CZ gate is given by

$$CZ = \begin{pmatrix} 1 & 0 & 0 & 0 \\ 0 & 1 & 0 & 0 \\ 0 & 0 & 1 & 0 \\ 0 & 0 & 0 & -1 \end{pmatrix}. \quad (2.7)$$

2.3.3 i SWAP gate

An interaction that can arise in certain multi-qubit experimental quantum computing systems is the transverse XY interqubit coupling. The time-evolution of a system of two qubits coupled with such an interaction can give rise to an i SWAP or an \sqrt{i} SWAP gate. In terms of the Pauli matrices, the interaction Hamiltonian between two qubits Q_A and Q_B can be generally written

$$H_{A,B}^{X,Y} = \frac{E_{A,B}^{XY}}{4} (\sigma_A^x \sigma_B^x + \sigma_A^y \sigma_B^y), \quad (2.8)$$

where $E_{A,B}^{XY}$ gives the energy scale of the interaction, and $\sigma_q^x(\sigma_q^y)$ is the $X(Y)$ Pauli matrix for qubit $q = A, B$ [1]. In Eq. (2.8), the products of Pauli matrices acting on different qubits corresponds to tensor products leading to a four-dimensional Hilbert space. The matrix representation of the i SWAP gate for XY interaction time $t = \pi\hbar/$

$E_{A,B}^{XY}$ is given by

$$i\text{SWAP} = \begin{pmatrix} 1 & 0 & 0 & 0 \\ 0 & 0 & i & 0 \\ 0 & i & 0 & 0 \\ 0 & 0 & 0 & 1 \end{pmatrix}. \quad (2.9)$$

The matrix representation of the $\sqrt{i\text{SWAP}}$ gate for XY interaction time $t = \pi\hbar/(2E_{A,B}^{XY})$ is given by

$$\sqrt{i\text{SWAP}} = \begin{pmatrix} 1 & 0 & 0 & 0 \\ 0 & 1/\sqrt{2} & i/\sqrt{2} & 0 \\ 0 & i/\sqrt{2} & 1/\sqrt{2} & 0 \\ 0 & 0 & 0 & 1 \end{pmatrix}. \quad (2.10)$$

As is true for one-qubit gates, the physical qubits and system determine how these two-qubit gates are implemented. This will be discussed in the next chapter.

Chapter 3

Superconducting circuit quantum electrodynamics

In this chapter, we move from the abstract to physical in our discussion of qubits and quantum information. Qubits are the fundamental component for a quantum computer, so the choice of a platform for a qubit is important for the applications. Much like a classical computer is not comprised of only bits, a quantum computer is not only comprised of qubits. We will introduce our qubit, the superconducting artificial atom, and the field of circuit quantum electrodynamics (cQED) that provides a framework for implementing and interfacing quantum circuits.

3.1 Superconducting Qubits

There are many platforms for implementing qubits for a quantum computer, including trapped ion, neutral atom, semiconductor spin, photons, and superconducting qubits [45]. Superconducting qubits are promising because they are highly compatible with existing fabrication techniques, and are integrated circuits that can have wires directly connected to the chip allowing for fast gate times and readout. The necessary component of these qubits is superconductivity.

Superconducting metals undergo a second-order phase transition at a critical temperature, T_c , below which electrical resistance goes to zero. At this critical temperature, a phonon-mediated interaction between electrons is able to overcome the electromagnetic repulsion between conduction electrons. Under these conditions, electrons

moving in a given direction distort ions within the material lattice causing charge distortion. This resultant charge distortion attracts another electron moving in the opposite direction within the lattice, and the electrons pair via virtual exchange of phonons [46]. The pairing of electrons results in a gap in the single-particle excitation spectrum of $\pm\Delta_{SC}$ about the Fermi energy that we call the superconducting gap. These stabilized, bound electrons are called Cooper pairs, and their pairing results in no scattering from energy perturbations smaller than $2\Delta_{SC}$ within the lattice, and gives rise to a characteristic zero resistance state in the superconducting medium. The fundamental hallmark of a superconducting state is the existence of a many-particle condensate analogous to the Bose-Einstein condensate, comprised of these Cooper pairs, which exhibit macroscopic phase coherence and carry current without dissipation [47].

3.1.1 Josephson junctions

As we introduced in Ch. 2, qubits are two-state systems that behave quantum mechanically. With that in mind, we can build a superconducting quantum harmonic oscillator using linear circuit elements comprised of an inductor L_r and a capacitor C_r , as shown in Fig. 3 (a). The quadratic potential energy well and energy eigenvalues are shown in Fig. 3 (b) for this device as a function of the phase across the superconducting inductor, which is defined in terms of the flux in the inductor normalized by the flux quantum with a factor of 2π . This harmonic potential results in evenly spaced energy levels at $\hbar\omega_r$ energy intervals. If our goal is to isolate a two-state system, this is not a viable option as the same drive frequency can excite the system to higher energy levels. Instead, we require a device with asymmetric energy level spacing that allows us to isolate a subspace that forms a two state system. Figure 3 (c) shows a modified circuit in which the inductive element has been replaced with a non-linear inductive element, a Josephson junction. To understand the resultant change in the energy potential and energy eigenvalues shown in Fig. 3 (d), we must first discuss the properties of Josephson junctions.

A Josephson tunnel junction is a nonlinear circuit element that can replace the linear inductor in our circuit. Josephson junctions are useful for constructing qubits due to their low dissipation and their ability to be microfabricated using integrated

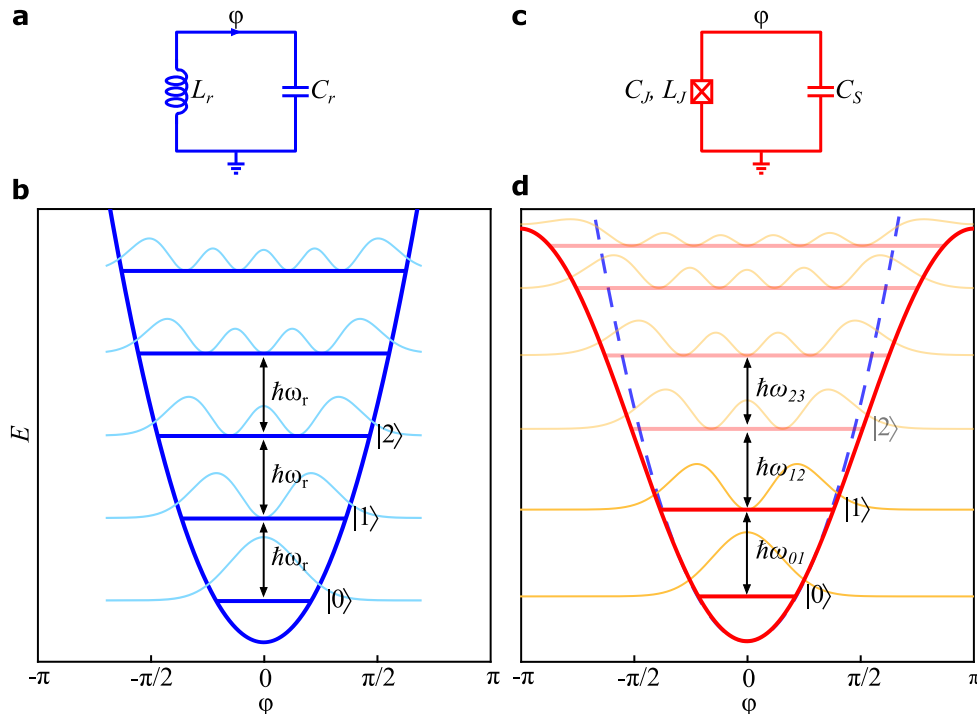


Figure 3: (a) Parallel LC -circuit realization of a quantum harmonic oscillator (QHO), with L_r and C_r being the circuit inductance and capacitance. (b) Quadratic energy potential well for the QHO with respect to the superconducting phase across the inductor, with evenly spaced energy eigenvalues separated by $\hbar\omega_r$ shown with blue horizontal lines. Squared moduli of the energy wavefunctions are shown in light blue. (c) Circuit comprised of a Josephson junction element with non-linear inductance L_J and capacitance C_J in parallel with a shunt capacitance C_S . (d) Cosine energy potential for the circuit shown in (c). Horizontal red lines show the unevenly spaced eigenenergies of the system with yellow lines showing the squared moduli of the eigenfunctions. The space between the $|0\rangle$ and the $|1\rangle$ state is given by $\hbar\omega_{01}$ and is not equal to the spacing between the $|1\rangle$ and the $|2\rangle$ states given by $\hbar\omega_{12}$

circuit processes. A Josephson junction may be formed by separating superconducting electrodes with a thin insulating region. This barrier must be designed with a thickness that allows for a slight overlap of the electron pair wave functions for the two superconducting electrodes, typically corresponding to a thickness of order 1 nm. A schematic of a Josephson junction is shown in Fig. 4, with the gray regions showing superconducting metal (Al) and the blue region showing the oxide barrier (AlO_x).

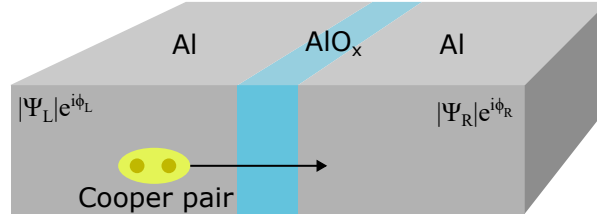


Figure 4: Schematic of a Josephson junction. The superconducting electrodes shown in gray are comprised of aluminum and are separated by a thin AlO_x barrier shown in blue. The macroscopic state of the Cooper pairs for each side of the junction are each given by the wavefunctions $|\Psi_L|e^{i\phi_L}$ and $|\Psi_R|e^{i\phi_R}$. Cooper pairs tunnel left to right with no dissipation in the presence of an applied current below the critical current with a phase difference $\varphi = \phi_L - \phi_R$.

The Josephson tunnel effect can be described with a set of classical equations for the Josephson current I_J and voltage V across the junction:

$$I_J(t) = I_0 \sin \varphi(t) \quad (3.11)$$

$$V(t) = \frac{\Phi_0}{2\pi} \frac{d\varphi(t)}{dt}. \quad (3.12)$$

In these expressions, $\Phi_0 \equiv h/2e$ is the magnetic flux quantum, I_0 is the junction critical current, and $\varphi = \phi_L - \phi_R$ is the superconducting phase difference across the junction [48]. Taking the definition $V = L \frac{dI(t)}{dt}$, we can manipulate Eqs. (3.11) and (3.12) to obtain an expression for the inductance of the Josephson junction, given by

$$L_J = \frac{\Phi_0}{2\pi I_0 \cos \varphi}. \quad (3.13)$$

The inductance is proportional to $1/\cos \varphi$, making this a nonlinear circuit element that we can use to replace the linear inductor in our quantum circuit. The energy stored by the junction over time is given by $E_J = \int I_J V dt$. If we use Eqs. 3.11 and 3.12, we get an expression for the Josephson energy:

$$E_J(\varphi) = \frac{I_0 \Phi_0}{2\pi} \cos \varphi. \quad (3.14)$$

The Ambegaokar- Barratoff relation allows us to relate the Josephson current to measurable, physical properties of the junction, and we can produce another expression for the Josephson energy

$$E_J \approx \frac{\Phi_0 \Delta_{SC}}{4eR_N}, \quad (3.15)$$

where Δ_{SC} is once again the superconducting gap energy and R_N is the normal-state resistance of the Josephson junction [49].

Going back to our discussion of Fig. 3 (d), after substituting a Josephson junction into the QHO circuit, the energy potential is now a cosine function, and the energy eigenvalues are no longer evenly spaced, but get increasingly closer at higher energy levels. This is an anharmonic system, with the anharmonicity defined as $\alpha \equiv \hbar\omega_{12} - \hbar\omega_{01}$. This anharmonicity allows the first two energy states to be isolated and used as the computational basis for a qubit.

3.1.2 Transmons

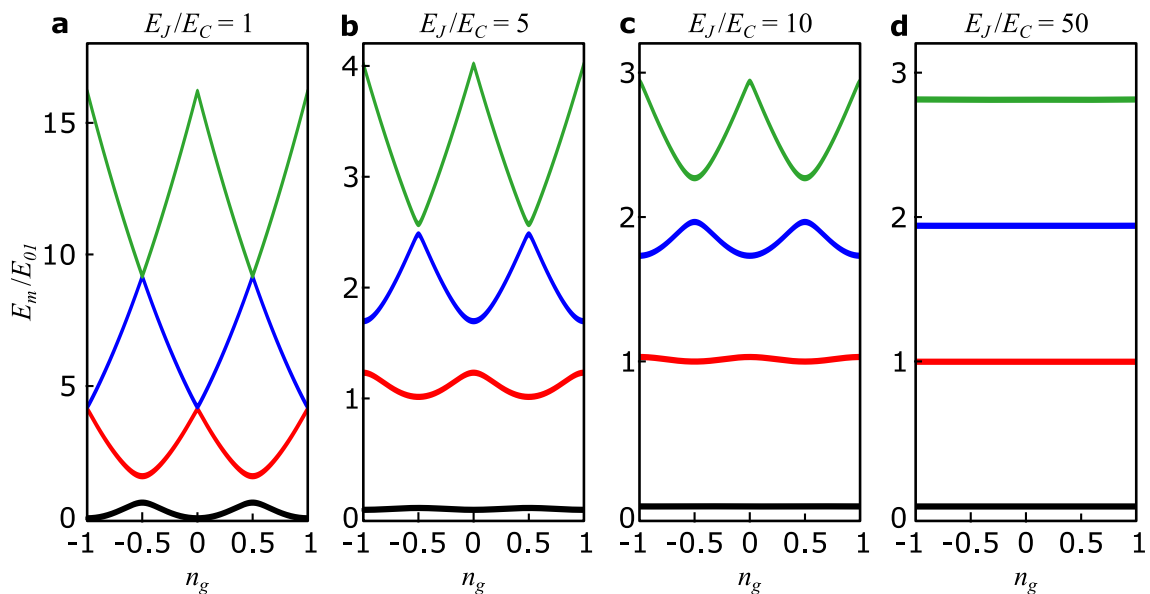


Figure 5: Eigenenergies E_m , for $m = 0, 1, 2, 3$ as a function of the effective offset charge n_g shown in black, red, blue, and green, respectively, for E_J/E_C ratios of (a) 1 (b) 5 (c) 10 and (d) 50. As the ratio of E_J/E_C increases, the charge dispersion decreases, making the qubit insensitive to fluctuations in offset charge for sufficiently large E_J/E_C .

The superconducting transmission-line shunted plasma oscillation qubit, or transmon qubit, is comprised of a superconducting island shunted to ground by a large capacitor and a nonlinear inductance [13]. The total capacitance for this isolated transmon circuit is given by $C_\Sigma = C_J + C_S + C_g$ where C_J is the capacitance of the

Josephson junction and C_S is the shunting capacitance, as shown in Fig. 3. The value C_g in this expression includes any external coupling to the qubit. The Hamiltonian for the transmon is given by

$$\hat{H} = \hat{H}_C + \hat{H}_J = 4E_C (\hat{n} - n_g)^2 - E_J \cos \hat{\varphi} \quad (3.16)$$

where $E_C = e^2/2C_\Sigma$ is the charging energy, and $n_g = Q_r/2e + C_g V_g/2e$ is the effective offset charge that is a function of the induced environmental offset charge Q_r , and the second term represents the offset charge coupled by an external voltage source V_g with a gate capacitance C_g .

Figure 5 shows the eigenenergies for a transmon as a function of the charging energy. To exponentially reduce the sensitivity of the qubit to charge noise, we can increase the ratio of E_J to E_C , as can be seen in Fig. 5(d). In doing so, we must operate in a regime with lower anharmonicity. This sets a lower bound on the duration of control pulses. In general, $E_J/E_C \geq 50$ is considered the transmon regime [13].

3.1.3 Floating-style, flux-tunable transmons

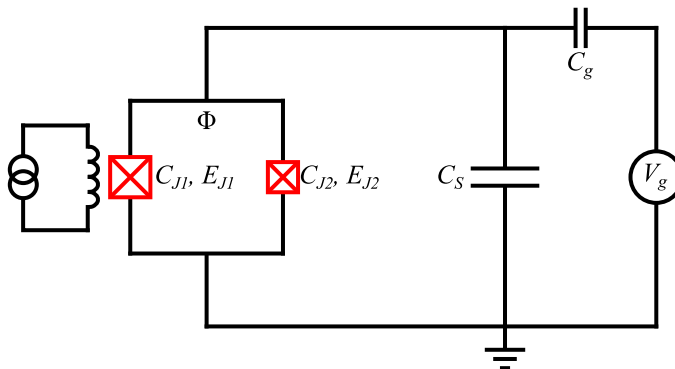


Figure 6: Circuit diagram of a flux-tunable asymmetric transmon. The gate voltage V_g is coupled via gate capacitor C_g . A dc SQUID, comprised of two asymmetric Josephson junctions with Josephson energies E_{J1} , E_{J2} with associated capacitances C_{J1} , C_{J2} , is inductively coupled to a current-bias line. The dc SQUID is shunted by capacitor C_S .

The implementation of a magnetic flux-tunable transmon qubit requires replacing the single Josephson junctions with a superconducting quantum interference device (SQUID), which incorporates two Josephson junctions in parallel in a superconducting

loop. SQUIDs exhibit a periodic modulation of the Josephson energy with a period given by $\Phi_0 \equiv h/2e \approx 2.07 \times 10^{-15}$ Wb, as well as the nonlinear tunneling rate of Cooper pairs through the junctions [50].

Figure 6 shows a circuit model of a flux-tunable transmon. The device includes a dc SQUID comprised of two asymmetric junctions with Josephson energies E_{J1} and E_{J2} [51]. We can quantify the asymmetry with the expression

$$d \equiv \frac{E_{J2} - E_{J1}}{E_{J1} + E_{J2}}. \quad (3.17)$$

The flux coupled to the SQUID loop, Φ , can be manipulated via an inductively coupled current-bias line. The Hamiltonian that describes the Josephson contribution is given by

$$\hat{H}_J = -E_{J1} \cos \hat{\phi}_1 - E_{J2} \cos \hat{\phi}_2, \quad (3.18)$$

with $\phi_1(\phi_2)$ describing the phase difference across junction 1(2). Utilizing flux quantization, we can assert that $\phi_1 - \phi_2 = 2\pi n + 2\pi\Phi/\Phi_0$, where n is an integer. This leads to an expression for the Hamiltonian which describes the flux-tunable, asymmetric transmon, given by

$$\hat{H} = 4E_C (\hat{n} - n_g)^2 - E_{J0} \cos \left(\frac{\pi\Phi}{\Phi_0} \right) \sqrt{1 + d^2 \tan^2 \left(\frac{\pi\Phi}{\Phi_0} \right)} \cos(\hat{\varphi} - \varphi_0), \quad (3.19)$$

where $E_{J0} = E_{J1} + E_{J2}$. The effective phase difference is given by $\varphi = (\phi_1 + \phi_2)/2$, and the value φ_0 can be found using the expression $\tan \varphi_0 = d \tan(\pi\Phi/\Phi_0)$ [13].

For an asymmetric transmon, the minimum transition frequency is greater than zero. As the flux coupled to the SQUID loop is tuned, the transition energy of the transmon modulates periodically. The slope of the transition energy is zero when $\Phi/\Phi_0 = 0$. For an asymmetric transmon, there is a non-zero minimum value for the transition energy when $\Phi/\Phi_0 = 0.5$ at which the slope is also zero, giving two flux-insensitive sweet spots at which we can operate the qubit [51].

3.2 Circuit Quantum Electrodynamics

Circuit Quantum Electrodynamics (cQED) is the coherent integration of nonlinear superconducting circuit elements with quantized electric fields. We have introduced the superconducting transmon qubit as the nonlinear element for our system, but in

order to do meaningful characterization of the quantum state, we must couple the artificial atom to a readout circuit in a controlled manner to minimize the reduction of qubit coherence [25, 52, 24].

First, we look at a simple, analytic model for our circuit by exploring the Jaynes-Cummings Hamiltonian. Then, we will integrate realistic models for our circuit components, including the flux-tunable transmon qubit and microwave cavity.

3.2.1 Jaynes-Cummings Hamiltonian

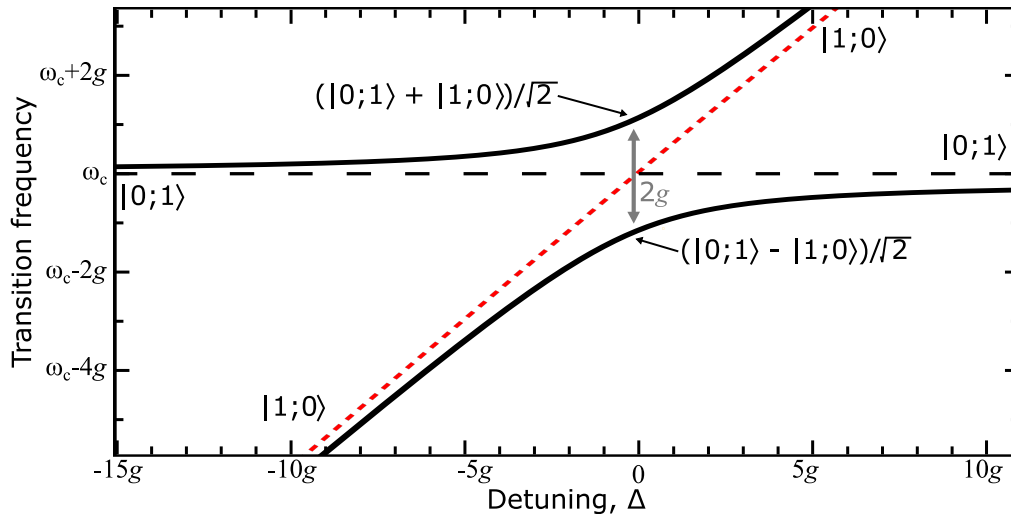


Figure 7: Avoided level crossing in the transition frequency for a system comprised of a tunable frequency qubit and a microwave cavity shown with solid black lines. The state vector is written as $|q; c\rangle$, where q denotes the qubit state and c denotes the cavity state. The uncoupled $0 \rightarrow 1$ base transition frequency of the qubit, ω_q , is shown with a red dotted line. The uncoupled cavity frequency, ω_c , is shown with a black dashed line.

A simple cQED system consists of an artificial atom coupled to a harmonic oscillator. An effective method for analytically studying the interactions between matter and light can be produced by restricting our atom to two levels. This system is described by the Jaynes-Cummings Hamiltonian [53],

$$\hat{H}_{JC} = \hbar\omega_c \hat{a}^\dagger \hat{a} + \frac{1}{2} \hbar\omega_q \hat{\sigma}_z + \hbar g (\hat{a} \hat{\sigma}_+ + \hat{a}^\dagger \hat{\sigma}_-), \quad (3.20)$$

where ω_c is the frequency of the cavity, or harmonic oscillator, ω_q is the frequency of the qubit. The terms a^\dagger and a are the raising and lowering operators for the photons in the cavity, and $\hat{\sigma}_+$ and $\hat{\sigma}_-$ are the raising and lowering operators for the qubit. The first term gives the energy of the resonator, the second term describes the energy contribution of the qubit, and the third term defines the interaction between the qubit and cavity with strength g , which is the rate for an excitation to swap back and forth between the qubit and cavity. This Hamiltonian is a conceptual starting point as it describes a wide range of platforms for a quantum device, and is analytically solvable.

We can use the Jaynes-Cummings Hamiltonian to understand fundamental dynamics in our system. For example, following the derivation in Ref. [5], let us look at the time evolution of this system. First, we can rewrite Eq. 3.20 as

$$\hat{H}_{JC} = \hbar\omega_c \left(\hat{a}^\dagger \hat{a} + \frac{\hat{\sigma}_z}{2} \right) + \frac{\hbar\Delta}{2} \hat{\sigma}_z + \hbar g (\hat{a} \hat{\sigma}_+ + \hat{a}^\dagger \hat{\sigma}_-), \quad (3.21)$$

where $\Delta \equiv \omega_q - \omega_c$ is the detuning frequency between the cavity and qubit. We have grouped the first term as it is a conserved quantity and does not change with time evolution. We can ignore this term when we look at the time evolution of this Hamiltonian as it supplies only a phase contribution. The time evolution operator is given by $\hat{U} = \exp(-i\hat{H}t/\hbar)$. If we restrict the system to at most one excitation in the cavity, the basis states are $|00\rangle$, $|10\rangle$, and $|01\rangle$, where the first digit corresponds to the atom and the second to the cavity excitations. In terms of the basis states from left to right and top to bottom,

$$\hat{H} = \hbar \begin{bmatrix} \Delta/2 & 0 & 0 \\ 0 & \Delta/2 & g \\ 0 & g & -\Delta/2 \end{bmatrix}. \quad (3.22)$$

The time evolution of this system is given by

$$\begin{aligned} \hat{U} = & e^{-i\Delta t/2} |00\rangle\langle 00| \\ & + \left(\cos(\Omega t) - i \frac{\Delta}{2\Omega} \sin(\Omega t) \right) |10\rangle\langle 10| \\ & + \left(\cos(\Omega t) - i \frac{\Delta}{2\Omega} \sin(\Omega t) \right) |01\rangle\langle 01| \\ & - i \frac{g}{\Omega} \sin(\Omega t) (|10\rangle\langle 01| + |01\rangle\langle 10|), \end{aligned} \quad (3.23)$$

where $\Omega/\hbar = \sqrt{g^2 + \Delta^2/4}$. We can see from the last line of this time evolution operator, that the exchange term between the qubit and the cavity has a sinusoidal term with frequency Ω , signifying that the cavity and atom exchange a single quantum of energy at this frequency, referred to as the Rabi frequency. In the case when $\Delta = 0$ and the qubit and cavity are exactly on resonance, Ω/\hbar is exactly g , the coupling strength [5]. Figure 7 shows the transition frequency of a system comprised of a frequency-tunable qubit and a microwave cavity. We can see that on resonance, the qubit and cavity swap an excitation. The cavity and qubit frequencies are split, with the split resonances separated by $2g$ in frequency. When the qubit and cavity are on resonance at the center of the anti-crossing, a hybrid state is formed between the qubit and cavity and the upper and lower branches become symmetric and antisymmetric superpositions of the two single-excitation states. As the detuning increases, the frequency of the Rabi oscillations increases, but the amplitude of the oscillations decreases with Δ .

The dynamics of the system change depending on the respective frequencies of the qubit and resonator, as well as the coupling strength. We have looked at the regime in which $\omega_c \approx \omega_q$. We call this regime the resonant regime. It is also feasible to operate in a regime in which the atom and cavity frequencies are detuned from one another. When $\Delta \gg g$, the system is considered to be in the dispersive regime.

To build a quantum system, it is useful to operate in a regime in which the measurement of the qubit does not flip the quantum state. This is called quantum non-demolition (QND). In the dispersive regime, the principal readout of the qubit state is performed by observing the scattering of a probe tone off of an oscillator coupled to the qubit. We can assume that when the cavity and qubit are sufficiently detuned, there is no direct qubit-cavity interaction. Following the derivation from the 2007 Koch paper [13], the Jaynes-Cummings Hamiltonian in the dispersive regime can be rewritten as

$$\hat{H} = \hbar(\omega'_c + \chi\hat{\sigma}_z)\hat{a}^\dagger\hat{a} + \frac{1}{2}\hbar\omega'_q\hat{\sigma}_z. \quad (3.24)$$

The effective dispersive shift for a transmon qubit is given by

$$\chi = \chi_{01} - \chi_{12}/2, \quad (3.25)$$

where

$$\chi_{ij} = \frac{g_{ij}^2}{\omega_{ij} - \omega_c}, \quad (3.26)$$

and $\omega_{ij} = \omega_j - \omega_i$ is the transition frequency of the qubit between levels i and j and g_{ij} is the associated coupling strength. The cavity and qubit frequencies are renormalized due to the asymmetric state-dependant cavity shift for the transmon, such that $\omega'_q = \omega_{01} - \chi_{01}$ and $\omega'_c = \omega_c - \frac{1}{2}\chi_{12}$. [13]. The grouped term shows that there is an atom-state dependent shift of the cavity in the dispersive regime.

Thus far, we have constrained our system to a two-level qubit and a harmonic oscillator. In the upcoming experiments, we will be utilizing flux-tunable transmons, which are not two-level systems, and in which photons and qubit excitations have finite lifetimes due to leakage. Additionally, the upcoming experiments will involve multimode cavities, which behave like a collection of harmonic oscillators with different frequencies. Next, we will look at a physical layout of a cavity and the limiting factors in photon lifetime in the cavity.

3.3 Superconducting cavities

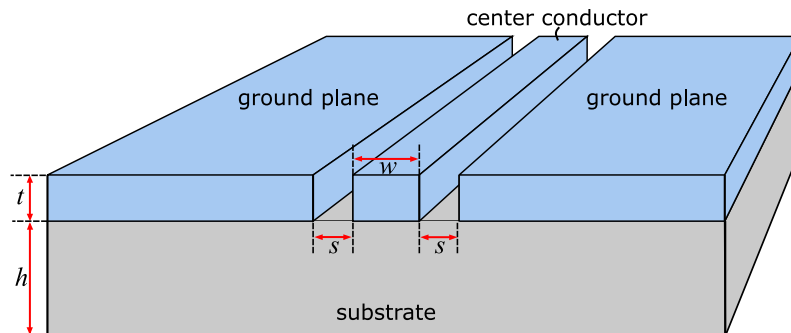


Figure 8: Geometry of a CPW. The center conductor has width w , and the gaps have width s . The film has a thickness t , and the substrate has a thickness h .

A transmission line (or distributed transmission line) of a certain length can be formed into a superconducting cavity by imposing boundary conditions, typically shorts or opens, at the two ends of the transmission line. A superconducting cavity acts as a photon mirror, reflecting photons of a narrow frequency band back and forth. A prominent platform for a superconducting cavity is a coplanar waveguide (CPW) resonator due to the ability to operate at frequencies in the GHz range, simplicity in fabrication, and the ability to realize large internal quality factors [54].

3.3.1 Transmission line quarter-wave resonator

Figure 8 shows the geometry of a CPW transmission line (TL), which consists of a center conductor with width w separated by a gap of width s from the ground plane. The thickness of the metal that comprises the center conductor and ground plane is t , and the thickness of the substrate is given by h . The substrate is, in general, a low loss dielectric crystal, typically Si or sapphire.



Figure 9: (a) Quarter-wave resonator comprised of a CPW transmission line with one end open and one end shorted to ground. (b) Near resonance, the quarter-wave CPW can be modeled by a simple driven parallel RLC circuit.

In this work, we utilize quarter-wave transmission line resonators as microwave cavities, produced when a small capacitor terminates one end of the resonator, and the other end connects to ground, shown in Fig. 9 (a). The experimental device that will be introduced in Ch. 6 has inductively coupled resonators, with a coupling inductor at the shorted end and an open circuit at the other end. For a quarter-wave resonator, the resonance f_r is given by

$$f_c = \frac{\omega_c}{2\pi} = \frac{v_p}{4l}(2n + 1), \quad (3.27)$$

where l is the length of the resonator, and $n = 0, 1, 2, \dots$ is an integer, with $n = 0$ corresponding to the fundamental harmonic. The phase velocity is given by $v_p = c/\sqrt{\epsilon_{eff}}$, where ϵ_{eff} depends on the substrate dielectric constant ϵ_r , the substrate thickness h , the conductor width w , the gap between the conductor and ground plane s , and the frequency [55]. The phase velocity can be calculated from the unit length capacitance C_R and inductance L_R of the CPW using the expression $v_p = 1/\sqrt{L_R C_R}$. This is called a quarter-wave resonator due to the factor of $1/4$ in Eq. (3.27). For a half-wave resonator, with either shorts or opens at both ends of the

CPW transmission line, the factor is $1/2$. Conformal mapping techniques can be used to derive expressions for the unit length inductance L_R and unit length capacitance C_R of a CPW resonator, given by [54]:

$$L_R = \frac{\mu_0}{4} \frac{K(k'_0)}{K(k_0)}, \quad (3.28)$$

$$C_R = 4\epsilon_0\epsilon_{eff} \frac{K(k_0)}{K(k'_0)}, \quad (3.29)$$

for which K denotes the elliptical integral of the first kind. The arguments are defined by

$$k_0 = \frac{w}{w + 2s}, \quad (3.30)$$

$$k'_0 = \sqrt{1 - k_0^2}. \quad (3.31)$$

For these derivations, we are neglecting the contribution of kinetic inductance defined by the kinetic energy of the superconducting electrons per unit length [56]. The characteristic impedance of the CPW resonator is given by $Z_0 = \sqrt{L/C}$.

Following the derivation in Ref. [55], near ω_c , we can approximate the quarter-wave resonator as a parallel RLC circuit, as shown in Fig. 9 (b). The impedance of a parallel RLC circuit is given by

$$Z_{RLC} = \left(\frac{1}{i\omega L} + i\omega C + \frac{1}{R} \right)^{-1}. \quad (3.32)$$

Using the series expansion $1/(x+1) \approx 1 - x + \dots$ and the assumption that $\omega = \omega_c + \delta\omega$ and $\delta\omega$ very small, we can write Eq. (3.32) as:

$$Z_{RLC} \approx \frac{R}{1 + 2i\delta\omega RC}. \quad (3.33)$$

The input impedance of a transmission line of length l and load impedance Z_l is given by

$$Z_{in} = Z_0 \frac{Z_l + Z_0 \tanh(\gamma l)}{Z_0 + Z_l \tanh(\gamma l)}, \quad (3.34)$$

where $\gamma = \alpha + ik$ is the propagation constant for waves in the resonator, defined in terms of the attenuation constant α and wavenumber k . Setting $Z_l = 0$, we get a quarter-wave resonance defined by Eq. (3.27), so Eq. (3.34) simplifies to

$$Z_{in} = Z_0 \tanh(\gamma l). \quad (3.35)$$

Expanding Eq. (3.35) using trigonometric identities and the expression for γ , we obtain an expression for the input impedance,

$$Z_{in} = Z_0 \frac{1 - i \tanh(\alpha l) \cot(kl)}{\tanh(\alpha l) - i \cot(kl)}. \quad (3.36)$$

Again using $\omega = \omega_c + \delta\omega$ under the assumption that $\delta\omega$ is very small, we can expand kl as

$$\cot(kl) = \cot\left(\frac{\pi}{2} + \frac{\pi\delta\omega}{2\omega_c}\right) \approx -\tan\left(\frac{\pi\delta\omega}{2\omega_c}\right) \approx -\frac{\pi\delta\omega}{2\omega_c}. \quad (3.37)$$

Here, we have used the relations $l = \lambda/4$ and $\lambda = 2\pi v_p/\omega_c$. We can simplify $\tanh(\alpha l) \approx \alpha l$ when there is low loss. Plugging these expressions into Eq. (3.36), we get

$$Z_{in} = Z_0 \frac{1 + i\alpha l \pi \delta\omega / (2\omega_c)}{\alpha l + i\pi \delta\omega / (2\omega_c)} \approx \frac{Z_0 / (\alpha l)}{1 + i\pi \delta\omega / (2\alpha l \omega_c)}. \quad (3.38)$$

We have written the right side of the expression in Eq. (3.38) in a similar form to the expression for input impedance for a parallel RLC circuit in Eq. (3.33). We can now write an expression for the equivalent circuit parameters, given by

$$R = \frac{Z_0}{\alpha l}, \quad (3.39)$$

$$L = \frac{1}{\omega_c^2 C}, \quad (3.40)$$

$$C = \frac{\pi}{4\omega_c Z_0}. \quad (3.41)$$

From these expressions, we can characterize the internal quality factor of the resonator. We have shown that a parallel RLC circuit is a good approximation for the CPW resonator near resonance, and the internal quality factor of a parallel RLC circuit is given by $Q_{int} = \omega_c RC$. Using Eqs. (3.39 - 3.41) we get the following expression for the internal quality factor of a quarter-wave CPW resonator,

$$Q_{int} = \frac{(2n+1)\pi}{4\alpha l}, \quad (3.42)$$

where we have accounted for the higher-order harmonics n . The total quality factor Q_{tot} of the resonator depends on Q_{int} as well as the coupling quality factor Q_C , with the relation

$$\frac{1}{Q_{tot}} = \frac{1}{Q_{int}} + \frac{1}{Q_C}. \quad (3.43)$$

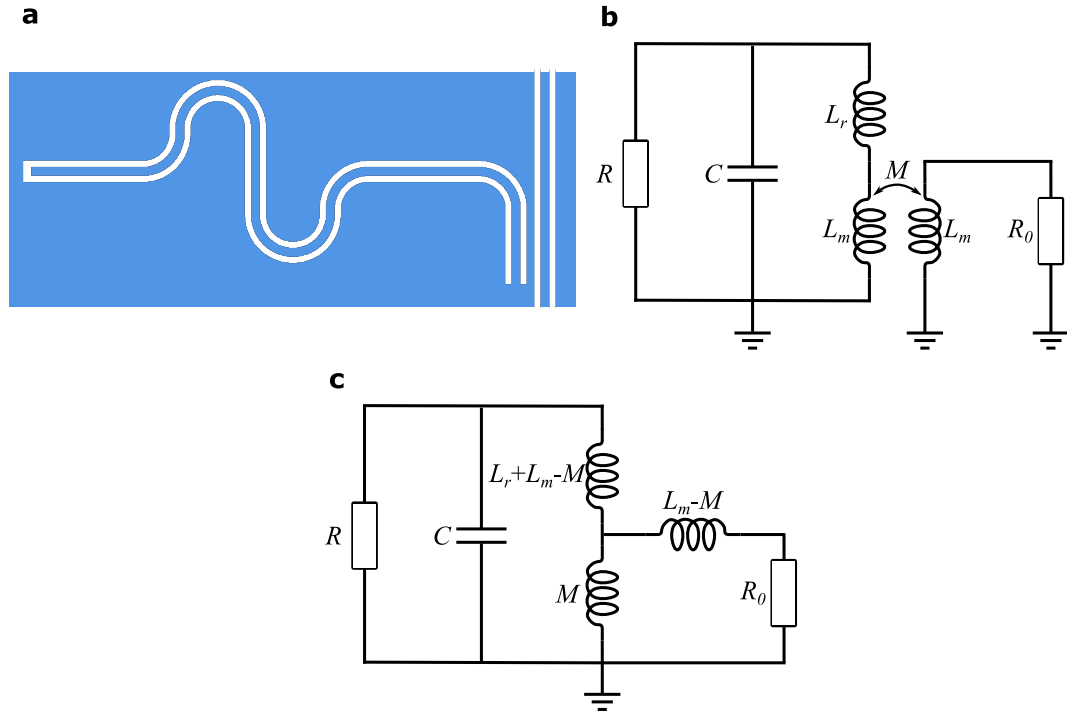


Figure 10: (a) Quarter-wave CPW resonator inductively coupled to a CPW feedline. (b) Circuit modeling a quarter-wave CPW near resonance as a parallel RLC circuit inductively coupled to an external load. The inductance L of the RLC circuit is split such that $L = L_r + L_m$, where L_r comprises the majority of the inductance, and L_m comprises the portion of the total inductance that contributes to the coupling. The mutual inductance between the RLC oscillator and external load resistance R_0 is given by M . (c) Equivalent circuit model with the mutual coupling replaced with inductive elements.

The quality factor relates to the rate of photon decay in the cavity with the expression $\kappa = \omega_c / Q_{tot}$. The internal quality factor depends on the materials that comprise the CPW, while the coupling quality factor depends on the external coupling parameters.

To obtain an expression for Q_C , we must be more specific about the physical coupling of the CPW to the external circuitry. Here, we assume a quarter-wave CPW inductively coupled to a feedline. The derivation of the equivalent circuit parameters was done conforming to the method used by Ref. [55], but this derivation aligns with the resonator design used in the experiment presented in Ch. 6. This structure is shown in Fig. 10(a). Figure 10(b) shows the CPW resonator modeled as a parallel

RLC circuit, inductively coupled to an external load resistance R_0 . The mutual inductance between the parallel RLC circuit and the external load is given by M , and the self-inductances of the coupling inductors are given by L_m . The total inductance of the RLC circuit is $L = L_r + L_m$, where L_r is the bulk of the inductance. since the bulk of the inductance of the CPW resonator does not contribute to the coupling to the external load. Figure 10(c) shows an effective circuit model for Fig. 10(b) [57]. The coupling quality factor gives the ratio of the energy stored by the oscillating RLC circuit per cycle, assuming there is no dissipation from the internal resistance R , to the power dissipated in the external load resistance R_0 . This is given by

$$Q_c = \frac{\frac{1}{2}CV_C^2\omega_c}{V_R^2/R_0}, \quad (3.44)$$

where V_R is the voltage across R_0 , and V_C is the voltage across C [55]. Solving for V_L in terms of V_C results in an expression for the coupling quality factor for a quarter-wave resonator inductively coupled to a feedline:

$$Q_c = \frac{R_0 Z_0}{2\omega^2 M^2}, \quad (3.45)$$

where $Z_0 = \sqrt{L/C}$ is the characteristic impedance of the resonator.

3.4 Scattering parameters

As Fig. 10(a) shows, we can couple superconducting cavities to a feedline comprised of a CPW transmission line to perform a measurement of the qubit. We measure the transmission of microwave signals through these feedlines. Transmission is measured via a scattering parameter matrix. A two-port device has a scattering matrix [55]

$$\begin{bmatrix} b_1 \\ b_2 \end{bmatrix} = \begin{bmatrix} S_{11} & S_{12} \\ S_{21} & S_{22} \end{bmatrix} \begin{bmatrix} a_1 \\ a_2 \end{bmatrix}, \quad (3.46)$$

with a_1 and a_2 denoting incident voltage waves and b_1 and b_2 denoting reflected waves; the S matrix elements are complex quantities. The matrix element S_{21} is used for our measurement setup to characterize transmission through the coupled resonator. In an ideal design, the load impedance matches the source impedance at the input of the resonator, and S_{21} can be written

$$S_{21} = \frac{b_2}{a_1} = \frac{2V_2}{V_1}, \quad (3.47)$$

where V_1 denotes the source voltage at port 1 and V_2 is the measured voltage at port 2.

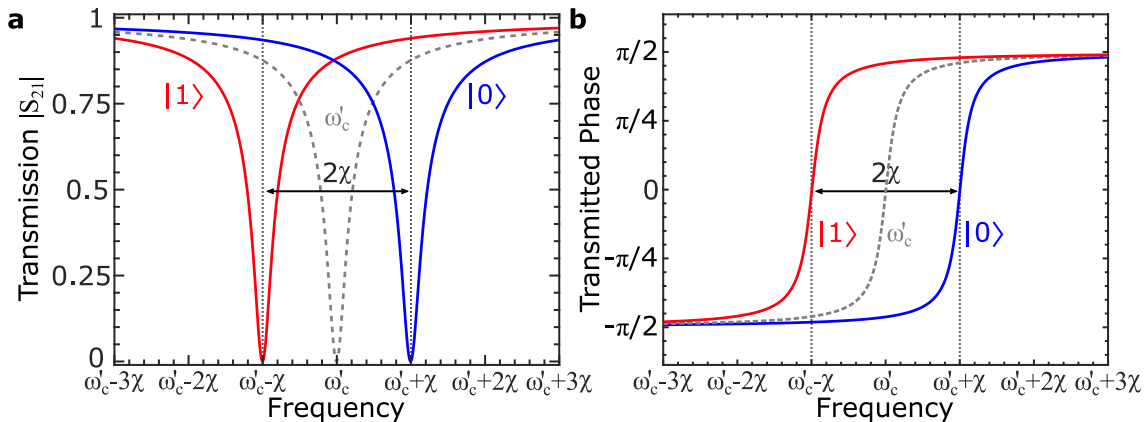


Figure 11: Transmitted (a) amplitude and (b) phase for a cavity resonator coupled to a transmon qubit showing qubit-state dependent cavity frequency shift. The renormalized cavity frequency ω'_c , shown with a gray dashed line, is shifted by $\pm\chi$ when the qubit is in the ground state $|0\rangle$ (excited state $|1\rangle$), shown with blue (red) lines.

3.5 Mapping the qubit state to the cavity state

Quantum non-demolition measurement in cQED allows us to map the qubit state to the cavity frequency and phase while preserving the state the qubit is projected into following the measurement. In the dispersive regime, when the cavity and qubit are far detuned, Eq (3.24) is valid. This expression shows that the cavity dispersively shifts, depending on the state of the qubit [13]. Figure 11 shows the simulated transmitted amplitude, $|S_{21}|$, and transmitted phase of a superconducting cavity as a function of frequency. For a CPW resonator coupled to a feedline, the transmission spectrum has a dip in transmission at the resonant frequency of the CPW resonator. The rate of photon decay κ , which we showed relates to the resonator quality factor in Sec. 3.3.1, gives the full width half maximum (FWHM) of the resonance. Figure 11 shows that when the qubit is in the excited state $|1\rangle$, shown in red, and the ground state $|0\rangle$, shown in blue, the cavity frequency shifts. Here, the cavity frequency has been renormalized so that $\omega'_c = \omega_c - \frac{1}{2}\chi_{12}$, so that the cavity resonance when the qubit is in $|1\rangle$ and $|0\rangle$ is $\omega'_c - \chi$ and $\omega'_c + \chi$, respectively.

3.6 Qubit decoherence

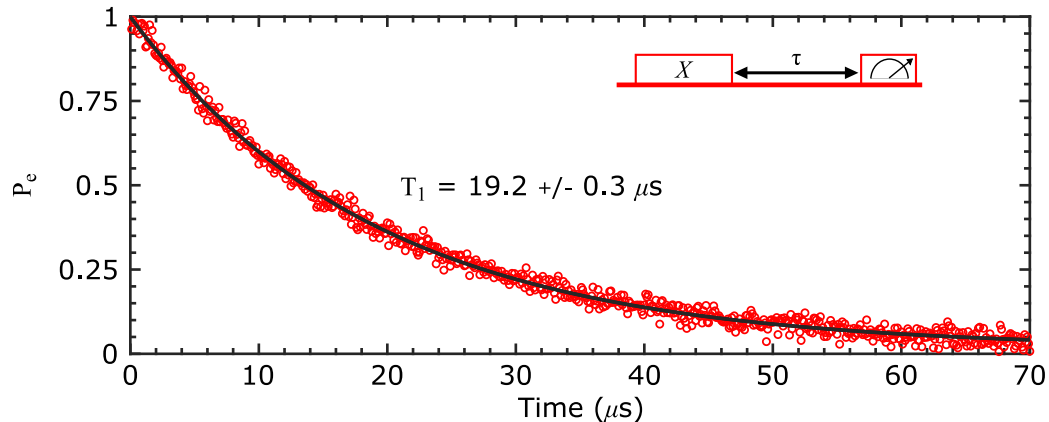


Figure 12: Longitudinal relaxation measurement for a transmon qubit as a function of time. Measured data is shown in red circles. Exponential decay fit is shown with a solid black line. The pulse sequence is shown as an inset. The measurement sequence consists of applying an X gate on the qubit, calibrated to excite the qubit to the $|1\rangle$ state, then implementing a variable delay before reading out the qubit state. The x-axis is the delay time τ .

In Sec. 3.2.1, we introduced the Jaynes-Cummings Hamiltonian and showed that under time evolution we observe Rabi oscillations in which excitations are swapped between the qubit and cavity. Thus far, we have treated our quantum system as deterministic, meaning that if we know the state of the system at $t = 0$, we can predict the state at $t = \tau$, where τ is some arbitrary time later. However, the system is inescapably coupled to uncontrolled degrees of freedom within the environment. There are a variety of noise sources that result in decoherence of a quantum state, and the platform informs which noise sources are most detrimental. For a flux-tunable transmon coupled to a CPW resonator, losses from quasiparticle poisoning, two-level system (TLS) loss, and low-frequency fluctuations of magnetic flux can cause decoherence [58].

There are two primary decoherence channels: relaxation and dephasing. Relaxation is the process by which a qubit exchanges energy with the environment, corresponding to a longitudinal decay of the qubit state in terms of the Bloch sphere (Fig. 1). This type of decay is due to transverse noise sources at the qubit frequency,

with the two most dominant sources being dielectric loss at the device surfaces and quasiparticle losses in the Josephson junctions [59]. The rate at which relaxation occurs is $\Gamma_1 \equiv 1/T_1$, where T_1 is the $1/e$ decay time for the qubit excited state to relax back to the ground state [1]. Figure 12 shows data for the relaxation of a qubit as a function of time in red circles with an exponential decay fit shown in solid black.

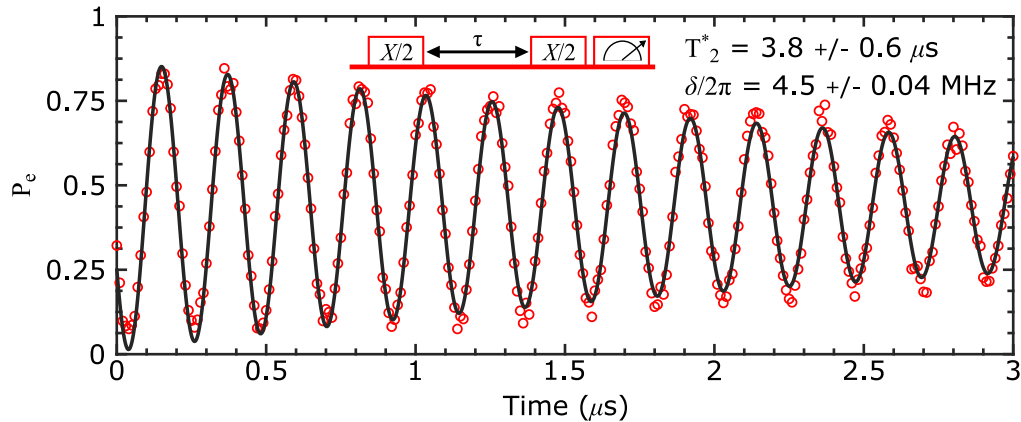


Figure 13: Measured one-state population as a function of delay time, τ , for Ramsey interferometry pulse sequence depicted. Red circles show measured data and black line shows exponentially decaying sinusoidal function fit. For this measurement, the midpoint of the oscillations is below 0.5, suggesting that the calibration of the X pulse results in a one-state probability of less than unity.

The second process that results in non-deterministic evolution of the qubit state is dephasing. Dephasing is a transverse decay in terms of the Bloch sphere. Dephasing is the process by which low-frequency fluctuations in the qubit transition frequency result in random phase shifts of the superposition state. The pure dephasing rate Γ_ϕ of the qubit state results in forward and backward precessions on the Bloch sphere. The cumulative dephasing rate Γ_2 accounts for the dephasing caused by energy relaxation and pure dephasing and is given by

$$\Gamma_2 \equiv \frac{1}{T_2^*} = \frac{\Gamma_1}{2} + \Gamma_\phi. \quad (3.48)$$

Figure 13 shows the measured transverse relaxation time T_2^* of a qubit. This measurement was performed using a standard Ramsey interferometry technique in which the qubit is prepared in the superposition state $(|0\rangle + |1\rangle)/\sqrt{2}$ using an $X/2$ pulse; then, after a variable idle time τ , another $X/2$ pulse is applied and then a readout

pulse is performed. The measured data is shown in red and the solid black line shows a fit to an exponentially decaying sinusoidal function from which we can extract T_2^* . The carrier frequency for the $X/2$ pulse is detuned by an amount δ from ω_q so that the Bloch vector will precess at a rate of the detuning frequency around the z -axis. In Fig. 13, the oscillation frequency is equal to the detuning frequency of 4.5 MHz. In Fig. 14, the normalized one-state occupation is shown for a Ramsey interferometry measurement taken as a function of δ .

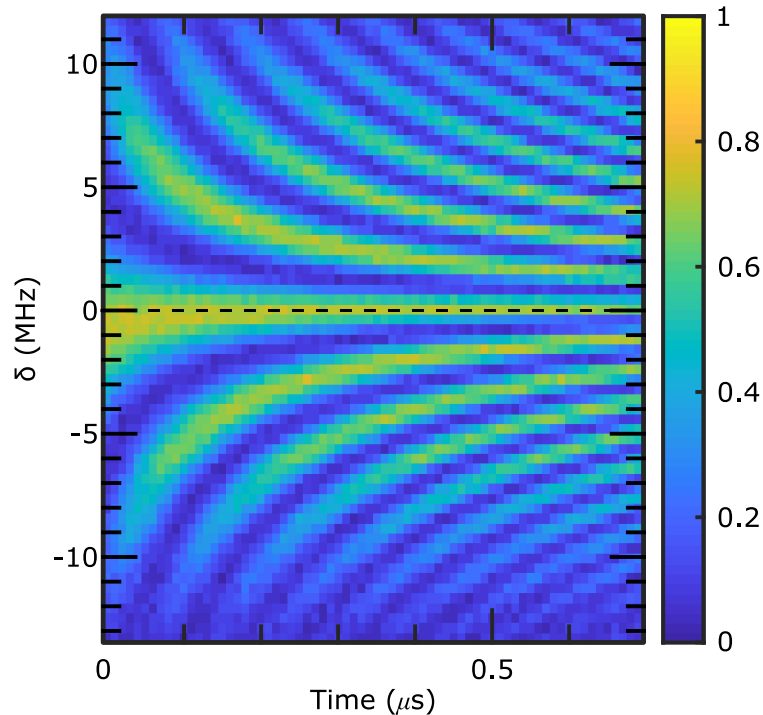


Figure 14: One-state occupation for a Ramsey interferometry measurement as a function of detuning frequency, δ and delay time between $X/2$ pulses. The dashed line shows the zero detuning point.

Another experiment, called the Hahn echo, is shown in Fig. 15. This measurement is similar to Ramsey interferometry, but is less sensitive to quasi-static noise. The Ramsey interferometry pulse sequence is modified such that at $t = \tau/2$, an X gate is applied, refocusing some of the dephasing and reducing inhomogeneous broadening of the state [1]. This decay time is called T_{echo} .

Figures 13, 15 show measurements taken for the same qubit. Comparing the extracted values for T_2^* and T_{echo} , we can see that T_{echo} is around 6 times longer than

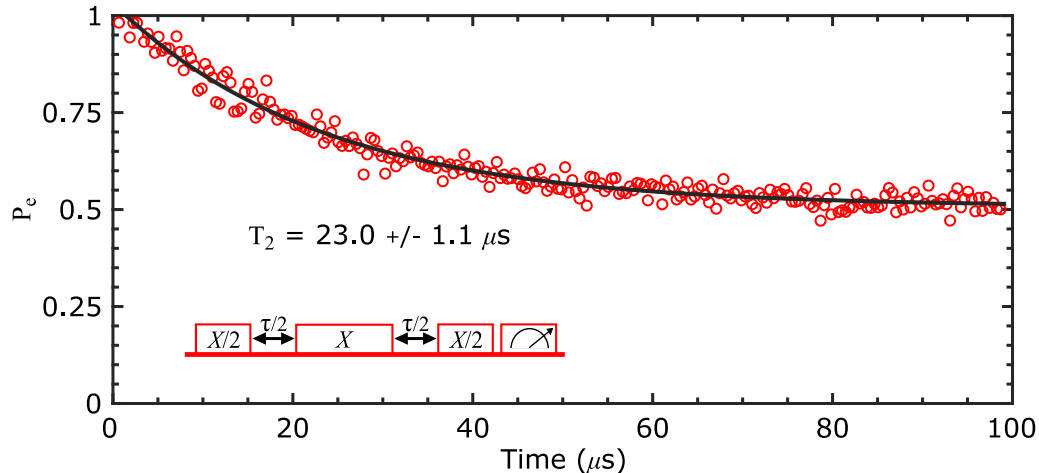


Figure 15: Measured one-state population as a function of delay time, τ , for Hahn echo pulse sequence depicted. Red circles show measured data and black line shows exponential decay fit.

T_2^* . The ratio of T_{echo} to T_2^* gives information about the power spectral density of the noise that causes dephasing. The ratio measured here is consistent with flux noise with a $1/f$ power spectrum.

3.7 Two-qubit interactions

Entangling gates are routinely performed on industrial quantum processors [60, 61], with high gate fidelities, but not as high as for single-qubit gates [62]. The limit of gate fidelities achievable for multi-qubit gates is a barrier to implementing effective quantum error correction. Additionally, existing 2-qubit gate schemes involve gates between nearest neighbor qubits only. Two-qubit operations have been performed in the field of cQED through various approaches, including direct coupling, tunable coupling, and coupling through a shared cavity. Direct two-qubit interactions have been realized on a variety of platforms, including capacitively coupling charge qubits and inductively coupling flux qubits [63, 64]. Tunable couplers can be realized using circuit divider elements [65, 66], couplers that use interference between different real and virtual coupling pathways [67], as well as modular double transmon coupler designs [68]. A quantum bus, generally realized using a cavity resonator, can also be used in quantum circuits to entangle distant qubits [69].

The two-qubit interactions described in this chapter are entangling interactions that allow for the implementation of two-qubit gates. First, we discuss the transverse exchange interaction, which allows for the exchange of excitations mediated by the coupling element between two qubits.

3.7.1 Exchange coupling

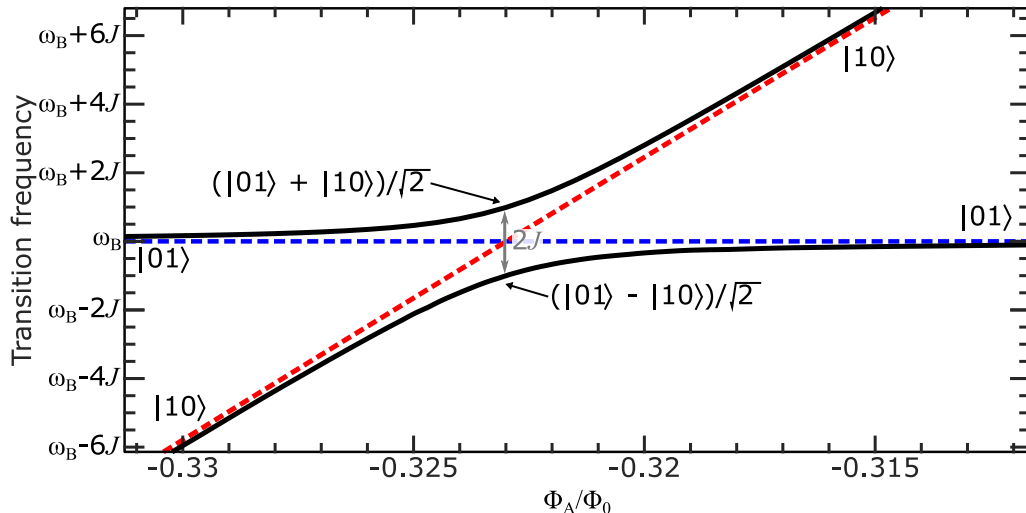


Figure 16: Theoretical plot of an avoided level crossing in the transition frequency of two qubits, Q_A and Q_B , when the transition frequency of Q_A is tuned through the fixed transition frequency of Q_B . The uncoupled $0 \rightarrow 1$ transition frequency of $Q_A(Q_B)$, $f_A(f_B)$, is shown with a red(blue) dotted line. The avoided crossing between Q_A and Q_B is shown in black.

To discuss the exchange coupling, we will focus on a specific platform comprised of two qubits coupled via a common resonator bus. If we have two qubits, Q_A and Q_B , which share a resonator bus, then the Jaynes-Cummings Hamiltonian is given by

$$H/\hbar = \omega_c a^\dagger a + \frac{\omega_A}{2} \sigma_A^z + \frac{\omega_B}{2} \sigma_B^z + g_A (a^\dagger \sigma_A^- + a \sigma_A^+) + g_B (a^\dagger \sigma_B^- + a \sigma_B^+). \quad (3.49)$$

From this expression, it is not immediately clear what form the direct coupling between qubits takes. We can perform a perturbative Schrieffer-Wolff transformation on this Hamiltonian under the dispersive regime assumption that Q_A and Q_B are far detuned from the cavity. In the Schrieffer-Wolff transformation, the Hamiltonian can

be divided into low-energy and high-energy subspaces. In doing so we can obtain a low-energy effective Hamiltonian. Using the unitary transformation [52]

$$U = \exp \left\{ \left[\frac{g_A}{\Delta_A} (a^\dagger \sigma_A^- - a \sigma_A^+) + \frac{g_B}{\Delta_B} (a^\dagger \sigma_B^- - a \sigma_B^+) \right] \right\}, \quad (3.50)$$

where $\Delta_q = \omega_q - \omega_c$ for $q = A, B$, we can adiabatically eliminate the resonant Jaynes-Cummings interaction. A second order approximation in terms of g_A/Δ_A and g_B/Δ_B gives the effective two-qubit Hamiltonian

$$H_{eff}/\hbar = \omega_c a^\dagger a + \frac{\tilde{\omega}_A}{2} \sigma_A^z + \frac{\tilde{\omega}_B}{2} \sigma_B^z + \frac{g_A g_B (\Delta_A + \Delta_B)}{2 \Delta_A \Delta_B} (\sigma_A^+ \sigma_B^- + \sigma_A^- \sigma_B^+). \quad (3.51)$$

In this expression, we assume the resonator cavity is initialized in the vacuum state and $\tilde{\omega}_q = \omega_q + \chi_q$ is the dressed qubit frequency for $q = A, B$. This assumption is valid only in the dispersive regime. The last term in Eq. (3.51) is the direct qubit-qubit exchange interaction, which we can rewrite as [69]

$$J = \frac{1}{2} g_A g_B \left(\frac{1}{\Delta_A} + \frac{1}{\Delta_B} \right). \quad (3.52)$$

This J -coupling interaction depends on the strength of each qubit coupling to the resonator, g_A and g_B , as well as the respective detunings between the qubits and the resonator, Δ_A and Δ_B . Figure 16 shows a model of the avoided level crossing for two qubits, Q_A and Q_B , when the transition frequency f_B of Q_B is fixed and we tune the transition frequency f_A of Q_A such that it crosses f_B . In this model, the two qubits are not directly coupled, capacitively or otherwise, The subsequent splitting shows an exchange coupling exists between the two qubits mediated by the shared cavity bus [69].

We introduced the two-qubit i SWAP and \sqrt{i} SWAP in Ch. 2. The swap of excitations between Q_A and Q_B at an anticrossing mediated by the coupling resonator bus can be used to realize an entangling \sqrt{i} SWAP gate. For a two-qubit system coupled via a resonator bus, moving the qubits to the anticrossing point for a time $t = \pi/(4J)$, or a quarter period of the oscillations in excitation between the qubits results in an \sqrt{i} SWAP gate [69]. It is alternatively possible to generate an exchange interaction between qubits with direct capacitive coupling instead of a common bus cavity [70, 71]. The advantage of using cavity bus coupling over direct capacitive coupling of two qubits is the possibility of long-distance interaction between physically separated qubits.

The J -coupling describes the second-order interaction between the two qubits that exists in the computational basis of two-level qubits. However, non-computational states, resulting from higher order interactions can also lead to entangling interactions between two qubits.

3.7.2 ZZ Interaction

Two qubits coupled to one or more common resonant modes in general will exhibit ZZ interactions between the qubits, where the state of one qubit shifts the transition frequency of the other qubit. We define the ZZ interaction

$$\zeta = E_{00} + E_{11} - E_{10} - E_{01}, \quad (3.53)$$

where E_{ij} corresponds to the energy eigenvalue of state $i(j)$ of $Q_A(Q_B)$. Figure 17 shows the simulated energy spectrum plotted for up to two excitations for two transmon qubits, Q_A and Q_B , as a function of the magnetic flux applied to Q_A while Q_B is positioned at a fixed $0 \rightarrow 1$ transition frequency. As Q_A is biased, its frequency shifts such that $|10\rangle$ and $|01\rangle$ exhibit an anti-crossing. As we discussed in Sec. 3.7.1, at this flux position, one could implement an i SWAP or \sqrt{i} SWAP gate. However, because of the negative anharmonicity of the two qubits, another avoided crossing occurs at a lower flux offset between $|11\rangle$ and $|20\rangle$. In Fig. 17(b), $|01\rangle + |10\rangle$ is shown with a gray dashed line, and the strength of the ZZ interaction $\zeta/2\pi$ is indicated as the difference between $|11\rangle$ and $|01\rangle + |10\rangle$. We can think of ζ in terms of the repulsion between $|11\rangle$ and $|20\rangle$. The Hamiltonian in Eq. (3.51) is truncated to obtain an expression for the exchange coupling between qubits. If we take a two-qubit Hamiltonian and go to fourth order, we can derive an expression for ζ in terms of the respective g -couplings of each of the qubits to the common cavity bus and the detuning of each of the qubits to the bus cavity using fourth-order perturbation theory, given by [72]

$$\zeta = \frac{g_A^2 g_B^2 (\Delta_A + \Delta_B)}{\Delta_A^2 \Delta_B^2}. \quad (3.54)$$

For a system comprised of two transmon qubits coupled via a resonator bus or directly coupled, capacitively or otherwise, the ZZ interaction can be problematic as it can generate unwanted and uncontrolled entanglement [73, 74]. Various approaches have been explored for reducing [75, 76] or nulling [77, 78] these interactions. However,

as we have indicated in Fig. 17, this interaction can also be used to intentionally generate qubit entanglement via the CZ or CPHASE gate that was introduced in Ch. 2.

A simple control mechanism to implement in flux-tunable transmon architectures is fast dc flux pulses to bring qubits in and out of resonance, as is used in Ref. [72]. Using Fig. 17 as a guide, we can conceive of a two-qubit gate that uses the avoided crossing between the non-computational state $|20\rangle$ and the one-excitation manifold state $|11\rangle$. The cavity-mediated shift of $\zeta/2\pi$ results in this avoided crossing which provides the mechanism for implementing the CZ gate. Once the states of the two qubits are initialized, ideally at a magnetic flux at which the two qubits are far detuned from each other and the shared cavity coupling bus, adiabatic (with respect

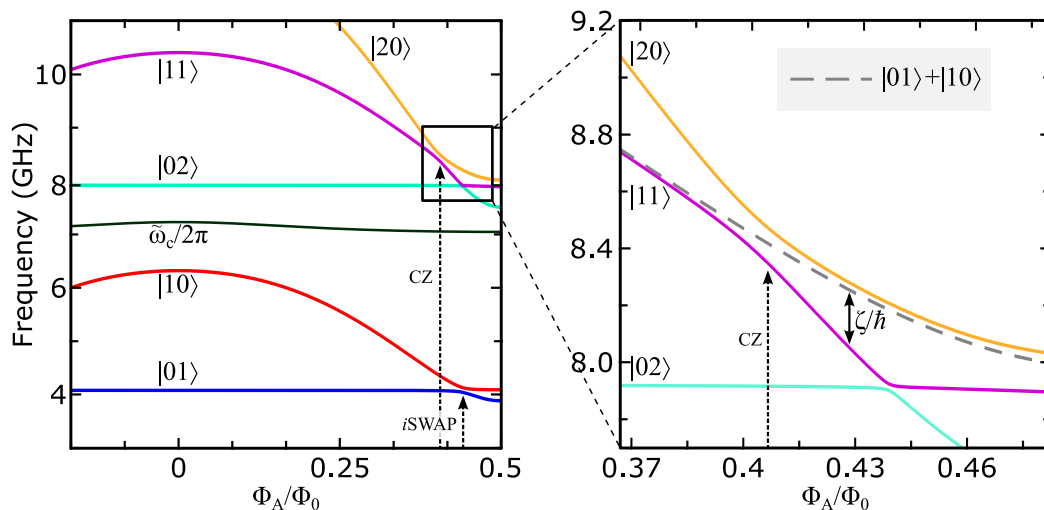


Figure 17: Theoretical energy spectrum for two transmon qubits coupled via a resonator bus at frequency $\omega_c/2\pi$ as a function of the magnetic flux on one of the qubits, Q_A , while the other qubit, Q_B , is fixed with its $0 \rightarrow 1$ frequency near 4 GHz. (a) Spectrum showing $|01\rangle$, $|10\rangle$, $|11\rangle$, $|02\rangle$, and $|20\rangle$ in blue, red, purple, teal, and orange respectively. Flux location on Q_A at which i SWAP and CZ gates may be implemented are indicated. (b) Zoom in of the $|20\rangle$, $|11\rangle$ avoided crossing. Gray dashed line shows $|10\rangle + |01\rangle$. The ZZ interaction strength is indicated by ζ/\hbar .

to the $|11\rangle \rightarrow |20\rangle$ avoided crossing) flux pulses produce phase gates

$$U = \begin{pmatrix} 1 & 0 & 0 & 0 \\ 0 & e^{i\phi_{10}} & 0 & 0 \\ 0 & 0 & e^{i\phi_{01}} & 0 \\ 0 & 0 & 0 & e^{i\phi_{11}} \end{pmatrix}. \quad (3.55)$$

Here, U is written in terms of the basis states $|00\rangle$, $|10\rangle$, $|01\rangle$, and $|11\rangle$ from left to right and top to bottom. The matrix elements $e^{i\phi_{ij}} = 2\pi \int \delta f_{ij}(t) dt$ give the dynamical phase acquired by state $|ij\rangle$, and δf_{ij} gives the deviation of f_{ij} from its initialization point. To implement a CZ gate, the adiabatic flux pulse is designed such that only $|11\rangle$ acquires a phase of -1 . A flux pulse that tunes Q_A to the flux position designated "CZ" in Fig. 17, such that $\int \zeta(t) dt = (2n + 1)\pi$ with integer n , results in a CZ gate. This is because $\phi_{11} = \phi_{10} + \phi_{01} - 2\pi \int \zeta(t) dt$ [79].

In the next two chapters, we will switch our focus to discuss metamaterial transmission lines and resonators. We will describe a multimode metamaterial ring resonator that can be used as a quantum bus to facilitate two-qubit entangling interactions such as the exchange coupling and ZZ interaction discussed.

Chapter 4

Left-handed transmission line resonators

In 1968, Viktor Veselago published a seminal paper that conceived of a material with a simultaneously negative permittivity ϵ and permeability μ [33]. The propagation of electromagnetic waves through matter is defined by ϵ and μ of the medium. The dispersion relation for an isotropic electromagnetic wave in simple matter is given by

$$\mathbf{k} = \frac{\omega}{c} n \hat{\mathbf{k}}, \quad (4.56)$$

where ω is the wave frequency, \mathbf{k} is its wave vector pointing in the direction of unit vector $\hat{\mathbf{k}} = \mathbf{k}/|\mathbf{k}|$, c is the speed of light in a vacuum, and n is the refractive index of the simple medium, with the relationship

$$n = \sqrt{\epsilon_r \mu_r}. \quad (4.57)$$

Here, $\epsilon_r = \epsilon/\epsilon_0$ is the relative permittivity, $\mu_r = \mu/\mu_0$ is the relative permeability, and ϵ_0 and μ_0 are the vacuum permittivity and permeability with the relationship $c = 1/\sqrt{\epsilon_0\mu_0}$. Equations (4.56) and (4.57) suggest that for a lossless medium with real n , ϵ , and μ , if ϵ and μ are both negative, there is no effect on the dispersion relation or on n ; however, Veselago postulates that if a material exists for which ϵ and μ are both negative, then it would not have the same properties as traditional materials.

In this chapter we will discuss Veselago's postulated metamaterials, or materials which have both a negative permittivity and permeability. We will show that

metamaterials have unique properties such as a negative index of refraction. We will also discuss a subset of metamaterials that exhibit fundamentally different dispersion from conventional transmission lines such as the CPW introduced in Ch.3. We will refer to the unique dispersion as "left-handed" in contrast with traditional materials that exhibit "right-handed" dispersion, and we will show that this has important implications for cQED.

4.1 Metamaterials

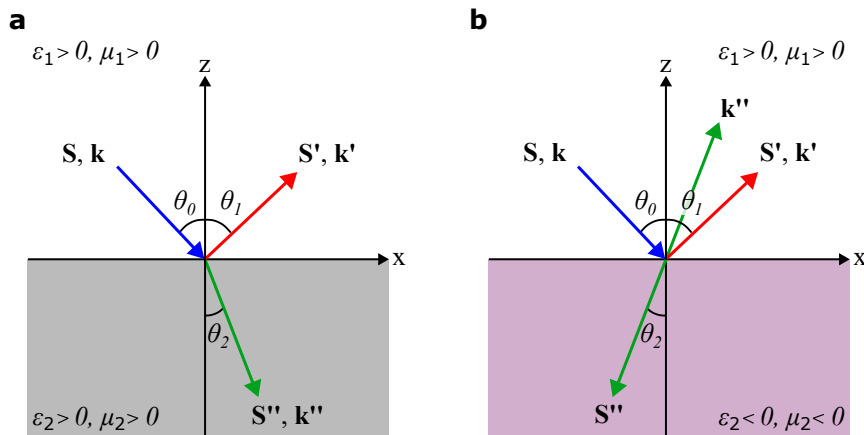


Figure 18: Electromagnetic waves incident on the boundary between two materials. \mathbf{S}, \mathbf{k} are shown in blue for the wave incident θ_0 from normal, \mathbf{S}', \mathbf{k}' are shown in red for the the reflected wave θ_1 from normal, and $\mathbf{S}'', \mathbf{k}''$ are shown in green for the refracted wave θ_2 from normal. The first material has positive permittivity ϵ_1 and permeability μ_1 , and the second has (a) positive permittivity ϵ_2 and permeability μ_2 or (b) negative permittivity ϵ_2 and permeability μ_2 . Figure is adapted from Ref. [2]

A naturally occurring material exhibiting both negative permittivity and permeability has not been found. Instead, to reach this regime, one must construct metamaterials, which are composed of elements derived from conventional materials arranged in repeated patterns with the size and spacing of the elements designed to be shorter than the wavelengths of interest. The applications of metamaterials span many fields, as a metamaterial can be engineered to have unique optical [80], acoustic [81], or mechanical properties [82].

Going back to the discussion from the beginning of this chapter, based on Eq. (4.57),

the following should be true for the refractive index of a metamaterial with simultaneously negative values for ϵ and μ : $n = c\sqrt{\epsilon\mu} = c\sqrt{(-\epsilon)(-\mu)}$. However, following the derivation in [83], we can show that Maxwell's equations require that $n = -c\sqrt{|\epsilon||\mu|}$.

This can be shown by looking at Maxwell's equations when ϵ and μ are not part of a product. Maxwell's equations for an infinite and spatially homogeneous medium are given by

$$\nabla \cdot \mathbf{E} = 0, \quad (4.58)$$

$$\nabla \cdot \mathbf{H} = 0, \quad (4.59)$$

$$\nabla \times \mathbf{E} = -\mu \frac{\partial \mathbf{H}}{\partial t}, \quad (4.60)$$

$$\nabla \times \mathbf{H} = \epsilon \frac{\partial \mathbf{E}}{\partial t}. \quad (4.61)$$

The Poynting vector, which describes the directional flux of energy for the system, is given by

$$\mathbf{S} = \mathbf{E} \times \mathbf{H}, \quad (4.62)$$

and points in the direction of propagation in traditional materials.

We can describe the electric and magnetic field of a monochromatic plane wave by the following equations

$$\mathbf{E}(\mathbf{r}, t) = \mathbf{E}e^{i(\mathbf{k}\cdot\mathbf{r}-\omega t)}, \quad (4.63)$$

$$\mathbf{H}(\mathbf{r}, t) = \mathbf{H}e^{i(\mathbf{k}\cdot\mathbf{r}-\omega t)}. \quad (4.64)$$

Via Maxwell's equations given in Eq. (4.60-4.61), we can formulate two key constraints for the monochromatic plane wave in simple matter, described by Eq. (4.63) and Eq. (4.64), given by

$$\mathbf{k} \times \mathbf{E} = \omega\mu\mathbf{H}, \quad (4.65)$$

$$\mathbf{k} \times \mathbf{H} = -\omega\epsilon\mathbf{E}. \quad (4.66)$$

When ϵ and μ are positive, Eqs. (4.65) and (4.66) form a right-handed triplet, and when ϵ and μ are negative, a left-handed triplet is formed. Thus, a material with simultaneously negative values of ϵ and μ was coined a left-handed substance by Veselago [84]. For a left-handed metamaterial, the propagation vector points in the

negative direction. At the beginning of this chapter, we stated that Maxwell's equations require that $n = -c\sqrt{|\epsilon||\mu|}$ be true, and the fact that \mathbf{k} is negative requires that $n < 0$ for a left-handed metamaterial. The Poynting vector, which follows from Eq. (4.62) and Eq. (4.65), is given by

$$\mathbf{S} = \frac{n}{c\mu} |\mathbf{E}|^2 \hat{\mathbf{k}}, \quad (4.67)$$

and it points in the opposite direction of \mathbf{k} and the phase velocity, given by $\mathbf{v}_p = c\hat{\mathbf{k}}/n$ [83]. The vectors \mathbf{S} , \mathbf{E} , and \mathbf{H} still form a right-handed orthonormal triad, despite the direction of propagation and the phase velocity being negative, meaning that the flow of energy is in the positive direction.

Figure 18(a) shows electromagnetic waves incident at the boundary of two right-handed materials. The wavevectors and Poynting vectors are shown for the incident waves that intersect the boundary at an angle of θ_0 from normal to the interface. The reflected wave is at an angle $\theta_1 = \theta_0$ from the normal, and the transmitted wave that propagates through the boundary is at θ_2 from the normal. Snell's law relates θ_1 and θ_2 to the velocity of the electromagnetic wave in each material v_1 and v_2 with the following expression [85]:

$$\frac{\sin \theta_1}{\sin \theta_2} = \frac{v_1}{v_2} = \frac{n_2}{n_1}. \quad (4.68)$$

Figure 18(b) shows the reflection and refraction of electromagnetic waves at the interface of a normal material and a left-handed metamaterial. The Poynting vector and wavevector point in opposite directions for the refracted wave due to the negative index of refraction of the metamaterial. The relationship between the angle of reflection, refraction, and the refractive indices for Fig. 18(b) are given by the left-handed version of Snell's Law,

$$\frac{\sin \theta_1}{\sin \theta_2} = -\frac{n_2}{n_1}, \quad (4.69)$$

where $n_1 > 0$ and $n_2 > 0$.

As we have shown, metamaterials can exhibit left-handed dispersion while conventional materials only exhibit right-handed dispersion, but the dispersion relation of a material depends on its form. Next, we derive the dispersion for a discrete right-handed transmission line as a basis for comparison to a left-handed transmission line.

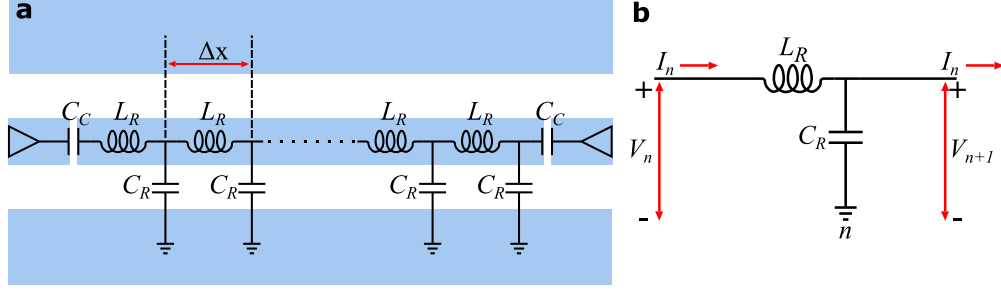


Figure 19: (a) Equivalent lumped-element CPW circuit comprised of series inductors L_R shunted by capacitors to ground C_R . (b) Voltages and currents for a single unit cell of length Δx .

4.2 Right-handed transmission line (RHTL)

In Chapter 3, we introduced the CPW resonator as a superconducting cavity for cQED. We showed that near resonance we can model the distributed CPW as a parallel RLC circuit. In this section, we will show that a CPW transmission line can be modeled as a series of cells comprised of lumped circuit elements. A lumped-element model for a CPW can be constructed with a chain of series of inductors with inductance L_R shunted to ground by capacitors with capacitance C_R . Figure 19 (a) shows the effective, lossless circuit. An expression for the dispersion of such a discrete transmission line can be easily derived by applying Kirchoff's Law for the circuit schematic shown in Fig. 19(b) [83]. Following the derivation from Ref. [2], we obtain the system of equations:

$$V_n - V_{n+1} = I_n(i\omega L_R), \quad (4.70)$$

$$V_{n-1} - V_n = I_{n-1}(i\omega L_R), \quad (4.71)$$

$$I_n - I_{n+1} = V_{n+1}(i\omega C_R), \quad (4.72)$$

$$I_{n-1} - I_n = V_n(i\omega C_R). \quad (4.73)$$

By substituting the admittance of the capacitor $Y = i\omega C_R$ and the impedance of the inductor $Z = i\omega L_R$, these expressions can be rewritten as

$$V_n(2 + ZY) = V_{n-1} + V_{n+1}, \quad (4.74)$$

$$I_n(2 + ZY) = I_{n-1} + I_{n+1}. \quad (4.75)$$

The solution for propagating waves through the transmission line at cell number n can be written in the general form

$$V_n = V_0^+ e^{-ikn\Delta x} + V_0^- e^{ikn\Delta x} \quad (4.76)$$

$$I_n = I_0^+ e^{-ikn\Delta x} + I_0^- e^{ikn\Delta x}, \quad (4.77)$$

where Δx is the length of the unit cell, and $k = 2\pi/\lambda$ is the wavenumber magnitude. Combining Eqs. (4.74) and (4.76), we obtain the relation

$$(V_0^+ e^{-ikn\Delta x} + V_0^- e^{ikn\Delta x}) [2 \cos(k\Delta x) - (2 + ZY)] = 0 \quad (4.78)$$

that leads to the condition $2 \cos(k\Delta x) = 2 + ZY$. From this condition, we get the dispersion relation for a CPW transmission line, given by

$$\omega_{RHTL} = \frac{2}{\sqrt{L_R C_R}} \sin\left(\frac{k\Delta x}{2}\right). \quad (4.79)$$

When $k\Delta x \rightarrow 0$, this corresponds to either long wavelengths, or the continuum limit. In this limit, the dispersion is a linear function given by

$$\omega_{cont} = \frac{k\Delta x}{\sqrt{L_R C_R}}. \quad (4.80)$$

From the dispersion relation in Eq. (4.80), it follows that the maximum frequency corresponding to the shortest wavelength results when $k\Delta x = \pi$. We can write $\lambda = 2\pi/k$, and from this we can see that the shortest wavelength in this discrete model is $2\Delta x$, or 2 unit cells. This is the ultraviolet cutoff frequency and is given by

$$\omega_{UV} = \frac{2}{\sqrt{L_R C_R}}. \quad (4.81)$$

The dispersion relation shown in Eq. (4.80) for a CPW is suggestively labeled ω_{RHTL} as it can be seen that as mode number increases, frequency increases. This type of dispersion is characteristically right-handed, making a CPW a right-handed transmission line (RHTL). Figure 20 shows ω_{RHTL} as a function of mode number with a blue line, with ω_{UV} shown as a blue dashed line.

A RHTL has dispersion such that for larger frequencies, the wavenumber increases. The phase velocity $v_p = \omega/k$ and the group velocity $v_g = d\omega/dk$ for a discrete RHTL point in the same direction, as is typical for materials that exhibit right-handed dispersion.

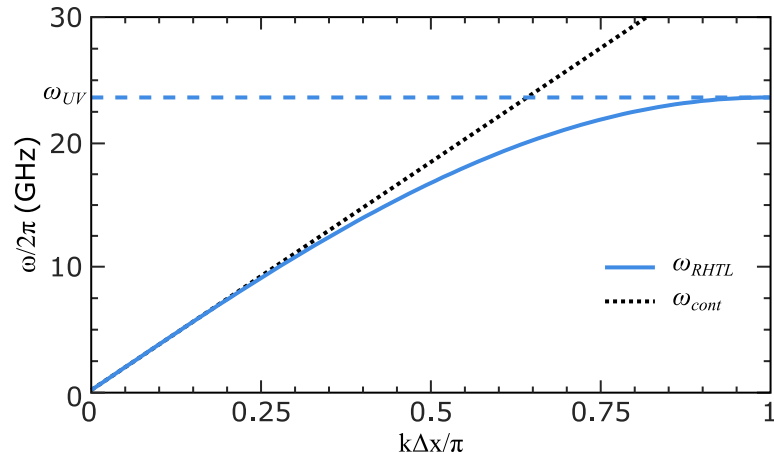


Figure 20: Right-handed dispersion relation as a function of normalized wavenumber shown with a solid blue line. The maximum resonance frequency, given by ω_{UV} , is shown with a dashed blue line.

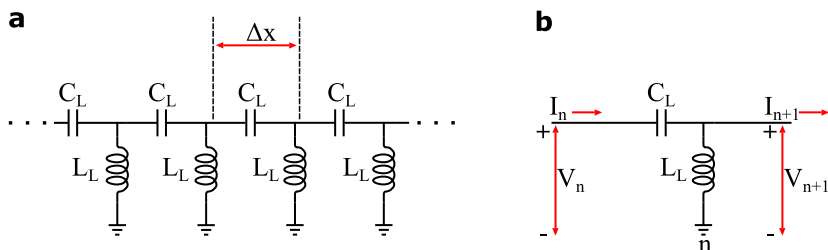


Figure 21: (a) LHTL circuit model comprised of series capacitors C_L shunted to ground by inductors L_L . (b) Definition of current and voltage for a LHTL at cell n .

4.3 Left-handed transmission lines (LHTL)

A circuit-board based metamaterial on the mm scale, fabricated using split rings, was one of the first experiments used to validate Veselago's claims about left-handed metamaterial properties [86]. It is feasible to engineer a microwave transmission line to have left-handed dispersion, in which mode frequency is a falling function of wavenumber and low frequency bandgaps [35, 34]. In order to integrate a metamaterial with qubits, the platform must be compatible with cQED architectures.

A RHTL can be realized using distributed transmission lines such as a CPW, or, as we introduced in Sec. 4.2, with a series of lumped-element inductors capacitively shunted to ground. If instead, the position of the inductors and capacitors is swapped, as is shown in Fig. 21(a), so that the transmission line consists of a chain of series of

capacitors C_L shunted to ground by inductors L_L , we can perform a similar derivation as in Sec. 4.2 to obtain the dispersion relation. Figure 21(b) shows a single cell for which we can apply Kirchoff's Law. As derived by [36], the system of equations is given by

$$V_n - V_{n+1} = I_n \left(\frac{1}{i\omega C_L} \right), \quad (4.82)$$

$$V_{n-1} - V_n = I_{n-1} \left(\frac{1}{i\omega C_L} \right), \quad (4.83)$$

$$I_n - I_{n+1} = V_{n+1} \left(\frac{1}{i\omega L_L} \right), \quad (4.84)$$

$$I_{n-1} - I_n = V_n \left(\frac{1}{i\omega L_L} \right). \quad (4.85)$$

Using the same methods in Eq. (4.74-4.78), we obtain an expression that must be satisfied for all values of $k\Delta x$ for solutions with propogating waves:

$$2 \cos(k\Delta x) = 2 + ZY, \quad (4.86)$$

where $Y = 1/(i\omega L_L)$ and $Z = 1/(i\omega C_L)$ are the admittance and impedance of the inductor and capacitor, respectively. From this expression, the dispersion relation for the transmission line follows:

$$\omega_{LHTL}(k) = \frac{1}{2\sqrt{L_L C_L}} \frac{1}{\sin\left(\frac{|k|\Delta x}{2}\right)}. \quad (4.87)$$

This expression includes an absolute value of k in the sine expression. As introduced at the beginning of this chapter, left-handed metamaterials have a negative index of refraction and \mathbf{S} and \mathbf{k} vectors that point in opposite directions; since the direction of \mathbf{k} corresponds to its sign, if \mathbf{S} is oriented in the positive direction, \mathbf{k} will point in the negative direction. Figure 22 shows the dispersion for the right- and left-handed transmission lines in solid blue and orange lines, respectively. For the left-handed transmission line (LHTL), the frequency decreases as $|k|$ increases. For $k = 0$, the frequency diverges, which is unphysical and will be discussed in more detail later in this chapter. When $|k|\Delta x = \pi$, the wavelength is two unit cells of the left-handed transmission line. This is the shortest wavelength of propagation possible, resulting in an infrared cutoff frequency

$$\omega_{IR} = \frac{1}{2\sqrt{L_L C_L}}, \quad (4.88)$$

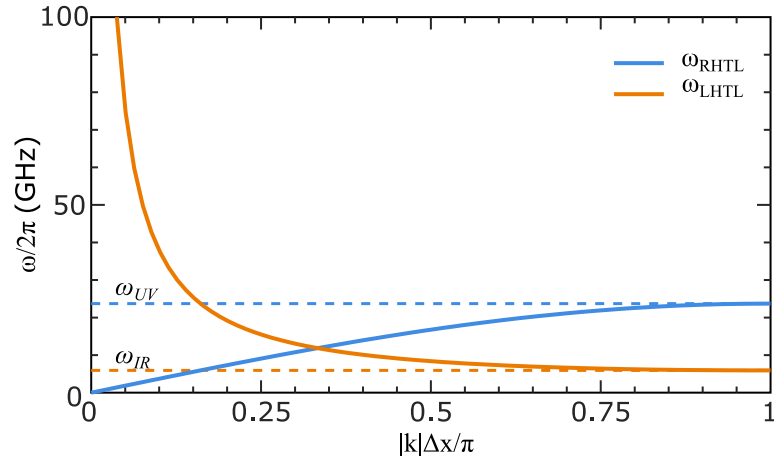


Figure 22: Dispersion relation for a discrete RHTL and LHTL as a function of the normalized absolute value of the wavenumber shown in blue and orange, respectively. The infrared cutoff frequency ω_{IR} for the LHTL is shown with an orange dashed line. The ultraviolet cutoff frequency ω_{UV} for the RHTL is shown with a blue dashed line.

below which, no waves can propagate. The infrared cutoff frequency ω_{IR} for the left-handed transmission line and the ultraviolet cutoff frequency ω_{UV} for the right-handed transmission line are shown in Fig 22 in orange and blue dashed lines, respectively. The characteristic impedance of this left-handed transmission line is given by

$$Z_0 = \sqrt{\frac{L_L}{C_L}}. \quad (4.89)$$

The LHTL formed from the lumped-element circuit shown in Fig 21(a) produces a fundamentally different dispersion to that of a RHTL. A unique feature is the inversion of the standard relationship between wavelength and frequency, such that the shortest wavelength in a LHTL corresponds to the lowest frequency. This behavior was experimentally verified by observing the standing-wave patterns in a LHTL resonator using laser-scanning microscopy (LSM) [36]. We will discuss metamaterial resonators in the next section.

4.3.1 Resonators formed from metamaterials

One can make a resonator from a CPW by coupling a length of CPW to a feedline, as discussed in Ch. 3, or by terminating each end of a CPW with a capacitor. It is

also feasible to make a metamaterial resonator by terminating each end of the metamaterial TL with capacitors. The standing waves that comprise the resonant modes in a metamaterial resonator would be integer multiples of half-waves, with the lowest wavenumber mode having a wavelength of twice the length of the transmission-line. The largest wavenumber mode would have the shortest possible wavelength of 2 unit cells. For a RHTL, the same is true, but the relationship between frequency and wavenumber is fundamentally different. For a RHTL resonator, the shortest wavelength (largest wavenumber) mode corresponds with the highest frequency mode. For a LHTL the shortest wavelength (largest wavenumber) mode corresponds with the lowest frequency mode. A physical implementation of a lumped element metama-

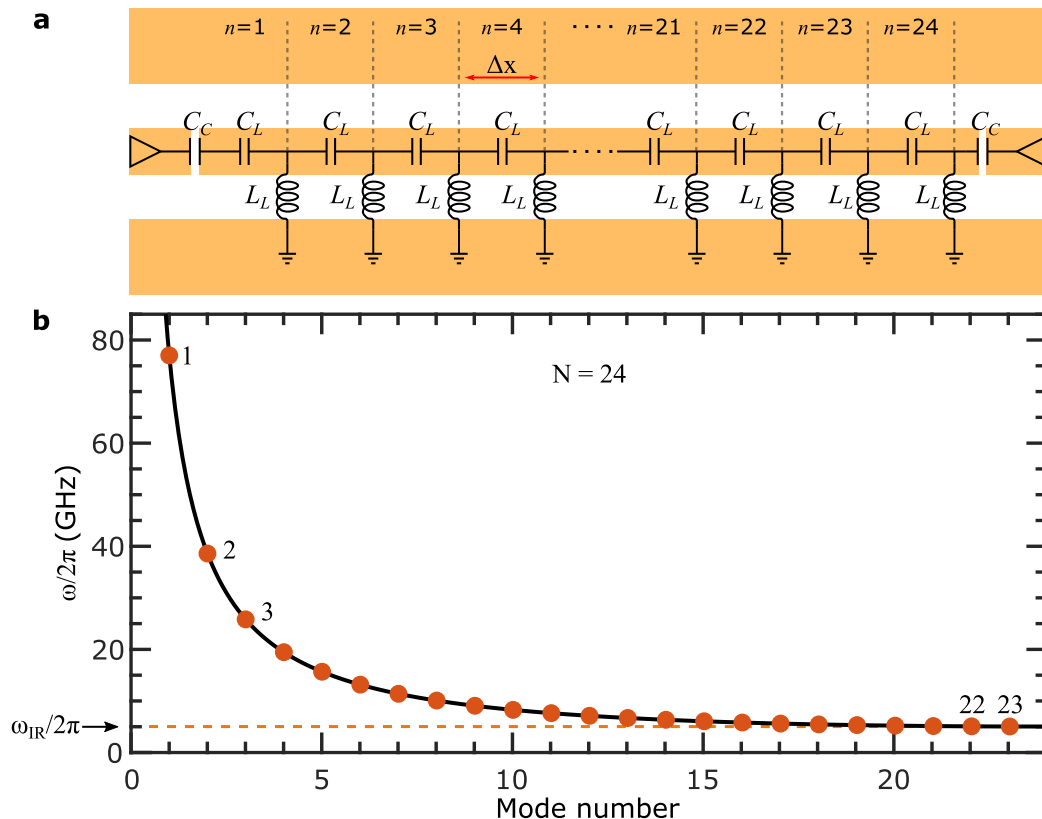


Figure 23: (a) LHTL resonator with 24 unit cells comprised of series capacitors C_L and parallel inductors L_L and input and output capacitances C_C at each end of the LHL. (b) Resonance frequency as a function of mode number for the 24-cell LHTL resonator. Orange data points show the discrete resonance frequency for each mode.

terial LHTL has a finite number of cells and length, and a defined set of boundary

conditions. We can relate the mode number to cell number under the resonance condition that $|k|l = n\pi$ for open boundary conditions when both ends of the LHTL are terminated by capacitors, where $n = 0, 1, 2, \dots, N$ is the relevant cell number and the total length $l = N\Delta x$. This leads to the relation

$$|k\Delta x| = \frac{n\pi}{N}. \quad (4.90)$$

In Fig. 23, mode frequency as a function of mode number for a 24-cell LHTL resonator is shown. There are a discrete number of resonances corresponding to the number of unit cells, as shown by the discrete orange data points. As the mode number increases, the frequency spacing between the modes decreases, resulting in a dense set of modes above the IR cutoff, shown with an orange dashed line in Fig. 23. We have noted that the frequency diverges for the LHTL approaching $n = 0$, meaning that there is no physically measurable resonant mode at $k = 0$. There is also no measurable mode when $n = N$ because the coupling quality factor diverges for this mode number making it unmeasurable [36]. A linear LHTL resonator with N unit cells will have $N - 1$ resolvable modes.

4.3.2 Stray reactance from lumped circuit elements in LHTL

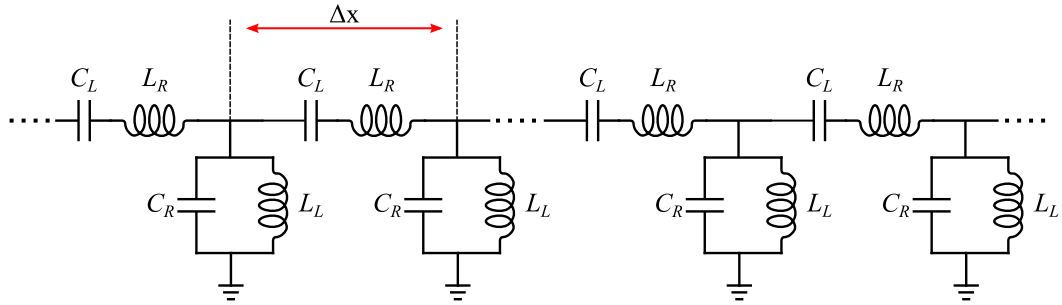


Figure 24: Circuit diagram of a composite LHRHTL, where the left-handed lumped circuit elements are C_L and L_L and the stray reactances that form the right-handed circuit are C_R and L_R .

The divergence of the frequency in the limit of $k \rightarrow 0$ corresponds to a divergence in the group velocity $v_g = \partial\omega/\partial k$; it is unphysical for such a divergence to exist. Any physical implementation of the lumped-element capacitors and inductors that comprise a LHTL will inevitably have parasitic stray reactances which arise from the

physical geometry of the circuit elements. These stray reactances result in a more complex circuit, as shown in Fig. 24, where the series capacitors C_L have stray series inductances L_R and the inductors to ground L_L have stray shunt capacitance C_R . These naming conventions are suggestive, as the stray reactances result in a circuit that is a composite of the lumped-element RHTL and the LHTL resonators, making it a left-handed/right-handed transmission line (LHRHTL) resonator [35]. We can define a self resonance of the lumped-element capacitors and inductors, given by $\omega_L = 1/\sqrt{C_L L_R}$ and $\omega_C = 1/\sqrt{L_L C_R}$, respectively.

A unit length Δx of a composite LHRHTL cell is shown in Fig. 24. Following the derivation in Ref. [2], the impedance and admittance per unit length are given by $Z = i(\omega L_R - 1/\omega C_L)$ and $Y = i(\omega C_R - 1/\omega L_L)$. Extending the derivation for the dispersion relation of a LHTL and substituting these expressions for Z and Y for a composite LHRHTL in Eq. (4.86), we get an expression for the dispersion relation of the LHRHTL given by

$$k(\omega) = \frac{1}{\Delta x} \cos^{-1} \left[1 - \frac{1}{2} \left(\omega L_R - \frac{1}{\omega C_L} \right) \left(\omega C_R - \frac{1}{\omega L_L} \right) \right]. \quad (4.91)$$

This expression has solutions for both positive and negative values of k . In Fig. 22, the dispersion for a LHTL and RHTL are shown as a function of $|k|\Delta x/\pi$. Because of the left-handedness of the metamaterial transmission line, $k < 0$. This is shown explicitly in Fig. 25, which shows the dispersion for the composite LHRHTL and a pure LHTL as a function of $k\Delta x/\pi$. The dispersion for the composite LHRHTL has a discontinuity at $k\Delta x/\pi = 0$ if $\omega_C \neq \omega_L$, where there are no propagating wave solutions. After the zero-crossing point, the dispersion transitions from left-handed to right-handed, where $k > 0$. Conversely, the pure LHTL frequency diverges unphysically as it approaches $k\Delta x/\pi = 0$.

4.4 Coupling transmon qubits to a LHTL resonator

LHTL resonators provide a multi-mode architecture with the capacity for engineering a dense spectrum in the GHz frequency range typical for superconducting qubits. Alternative architectures for coupling qubits to multi-mode systems in the field of cQED include using long RHTL resonators with multiple modes in the frequency range of the qubits [29], introducing Josephson junctions in right-handed circuits

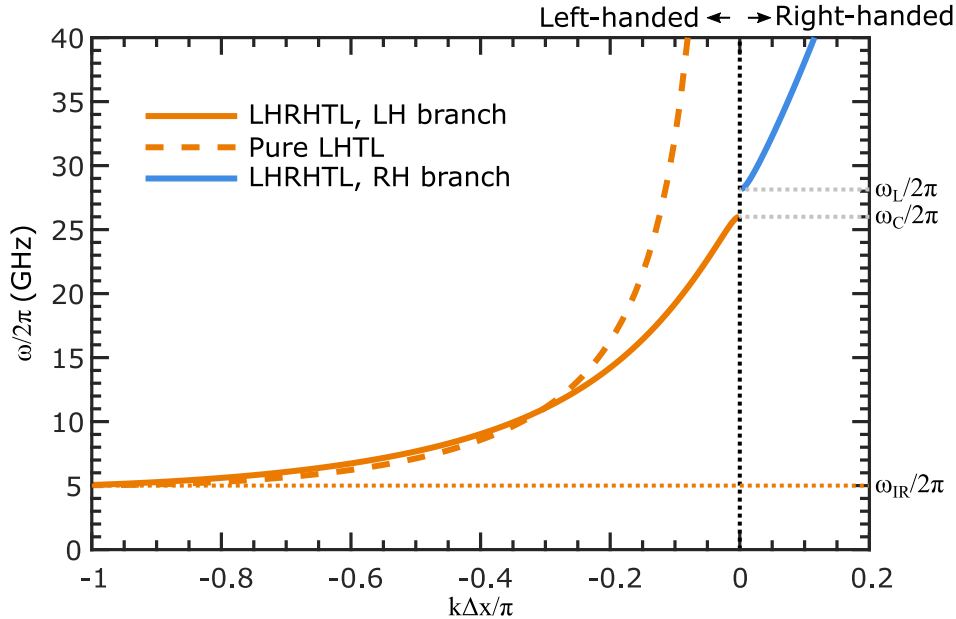


Figure 25: Dispersion relation for a discrete RHTL and LHTL as a function of normalized mode number shown in blue and orange, respectively. The infrared cutoff frequency ω_{IR} for the LHTL is shown with an orange dashed line. The self-resonance frequencies for the lumped-element capacitors $\omega_C/2\pi$ and inductors $\omega_L/2\pi$ create a band gap with no propagating wave solutions, shown with gray dashed lines.

to generate non-linearity [87], and engineering large-scale lumped circuit elements to produce metamaterials [88]. In contrast to these approaches, the LHTL resonator has an IR-cutoff frequency that can be engineered such that tunable qubits coupled to the LHTL resonator have a flux-insensitive lower sweet-spot at a frequency below the IR-cutoff, as opposed to having resonances in the entire qubit frequency range. This allows a location at which the qubit(s) can be detuned from the modes. Additionally, the LHTL resonator has a relative small footprint and does not require as much physical space on the chip to produce multiple modes in the desired frequency range. With these advantages, a LHTL resonator can be a useful cavity for multi-mode cQED with qubits. In cQED, qubits are typically capacitively coupled to resonant circuits at voltage anti-nodes of a particular mode to maximize the coupling strength. However, for a LHTL resonator, there are many modes in the frequency range of interest, and selecting a voltage anti-node for multiple modes simultaneously is more challenging. Figure 26 shows a schematic of a 24-cell LHTL resonator coupled to

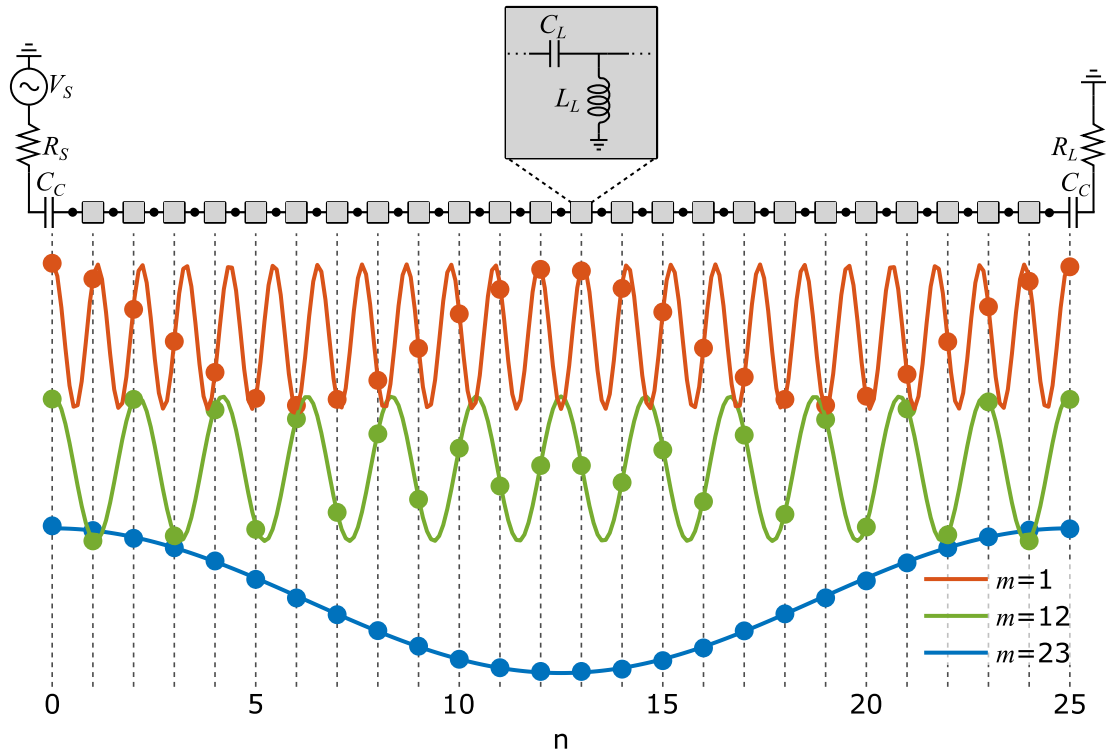


Figure 26: Voltage in arbitrary units as a function of node position for a 24-cell LHTL resonator for modes 1, 12, and 23, shown in orange, green, and blue, respectively, with an arbitrary offset in voltage added between modes. The circles correspond to the voltage amplitude of the standing wave at a given node across the LHTL resonator. The only node position at which the modes would be maximally coupled to a qubit correspond to the $n = 0$ and $n = 25$ node positions of the input/output capacitors to the LHTL resonator.

a voltage source. The theoretical waveforms of three example resonant modes are plotted as a function of cell-number in arbitrary units of voltage, with nodes $n = 0$ and $n = 25$ corresponding to the the location of the input and output coupling capacitors. The only coupling location at which a qubit could be maximally coupled to all of the modes corresponds to the input and output capacitor locations. An alternative scheme for coupling qubits to a LHTL resonator was proposed by [89], in which a LHTL is combined with a RHTL to form a split left-handed, right-handed transmission-line resonator. If qubits are coupled to the right-handed portion of the

resonator, it results in simultaneous non-zero coupling of the qubits to all of the left-handed modes. This structure has been experimentally validated and has been shown to have predictable multi-mode coupling to a superconducting qubit [37]. The ideal coupling scheme depends on the applications. In the next chapter, we will discuss a metamaterial ring resonator. For this device, the coupling mechanism for the qubits to the ring resonator is designed such that the ring resonator acts as a bus for inter-qubit coupling, and the qubits are capacitively coupled directly to particular unit cells of the ring resonator.

Chapter 5

Left-handed metamaterial ring resonators

Resonant structures with ring topology are prominently used in photonic systems to trap and confine light in small volumes, resulting in enhanced light intensity and nonlinear effects in a compact footprint [41]. Many optical applications for ring structures have been explored, including microwave-optical transducers [38], microwave frequency combs [38], and multimode nonlinear optics [40, 42]. Superconducting ring resonators with right-handed dispersion have been used in cQED applications as a resonator bus for multiple qubits [90, 43]. This application requires a large footprint, as the circumference must be a minimum of one wavelength of the resonant frequency of interest. The typical wavespeed for a CPW transmission line with a Si substrate is $v \approx 0.40c$, where c is the speed of light in a vacuum. So for a resonant frequency of 5 GHz, a CPW ring would need to have a circumference of approximately 25 mm. Superconducting metamaterial split-ring resonators have also been explored for applications such as tunable and passband filtering in the microwave frequency range [91]. Ring resonators are produced by connecting two ends of a transmission line to form a closed loop. By wrapping a transmission line onto itself and preserving the symmetry of the structure, the resultant path of a signal inside the ring is unconstrained. Clockwise and counter-clockwise propagation has equal probability, and the distribution of electromagnetic fields is uniform [90]. The combination of clockwise and counter-clockwise propagation leads to degenerate ring resonator modes highly dependent on the symmetry of the ring. Coupling external circuit elements to a ring

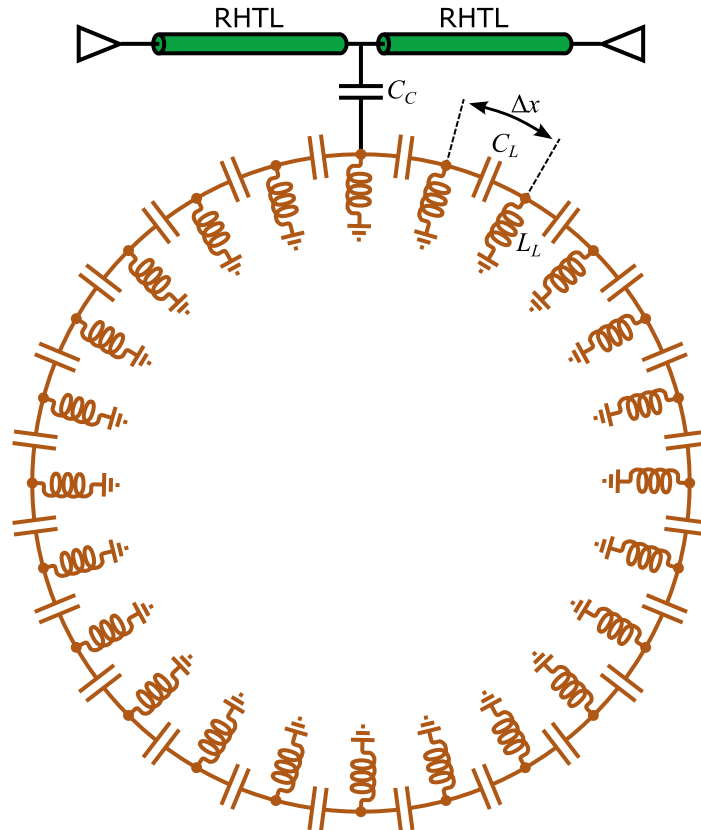


Figure 27: Left-handed metamaterial ring resonator with 24 unit cells with cell length Δx , comprised of series capacitors C_L and parallel inductors L_L .

enforces geometric boundaries, but does not constrain the two modes of propagation. In this chapter, we will discuss a novel metamaterial ring resonator formed from a LHTL that can be used as a multimode bus to facilitate entangling interactions between qubits. We will show that a metamaterial ring resonator produces a multimode spectrum with pairs of degenerate frequency resonances due to the clockwise and counter-clockwise propagation in the ring; we will then describe how these degeneracies can be lifted when circuit elements are placed at particular locations around the ring.

5.1 Left-handed metamaterial ring resonator

Wrapping a linear LHTL resonator, introduced in Ch. 4, into a ring produces a unique dispersion with counter-clockwise and clockwise modes of propagation and a small

physical footprint. Figure 27 shows a circuit schematic for a left-handed metamaterial ring resonator, with cell size given by Δx and unit-cell capacitance and inductance given by C_L and L_L . The dispersion relation for the left-handed material ring is identical to that of the linear LHTL, given by

$$\omega(k) = \frac{1}{2\sqrt{L_L C_L}} \frac{1}{\sin\left(\frac{|k\Delta x|}{2}\right)}. \quad (5.92)$$

A left-handed metamaterial ring resonator with a finite number of cells N has a discrete set of resonant frequencies. This results in periodic boundary conditions, similar to Born-von Karman boundary conditions imposed on a wave function in a lattice [92]. The lattice in the case of the left-handed metamaterial ring resonator, or ring resonator for short, is the discrete set of cells. As we have stated, these

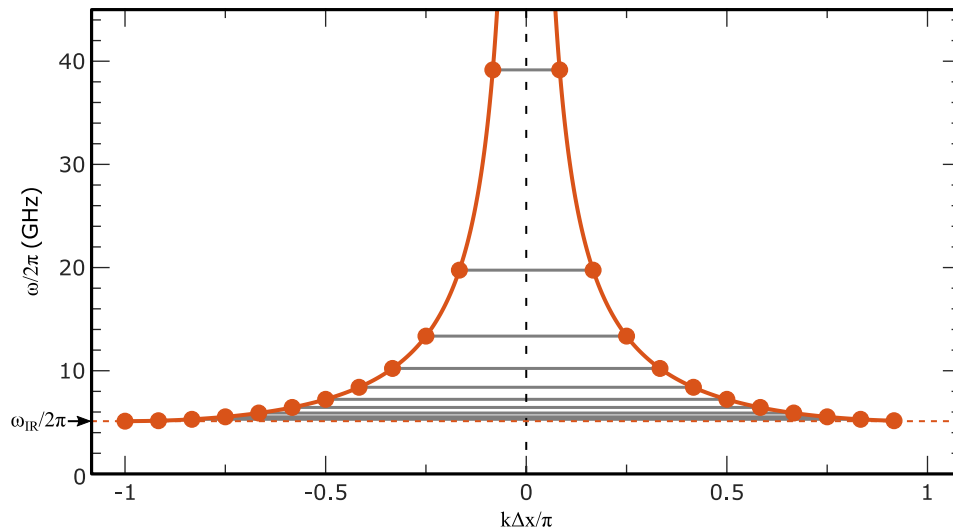


Figure 28: Resonance frequency as a function of mode number for a 24-cell LHTL metamaterial ring resonator. Orange data points show the discrete resonance frequency for each mode. Gray lines connect degenerate resonance modes, only differentiable by phase in an ideal ring resonator

conditions result in two types of propagating waves in the ring resonator: clockwise and counterclockwise. Given that the dispersion relation in Eq. (5.92) depends on $|k|$, waves moving in opposite directions have the same frequency and only differ in phase. In a perfect ring with identical cells and no external coupling, equal combinations of clockwise $|k\rangle$ and counterclockwise $| -k\rangle$ waves define the standing wave of frequency

$\omega(k)$, with even and odd parity $|E\rangle = (|k\rangle + |-k\rangle)/\sqrt{2}$ and $|O\rangle = (|k\rangle - |-k\rangle)/\sqrt{2}$, respectively. The resonance condition for the ring resonator is given by

$$k\Delta x = \frac{2\pi n}{N}. \quad (5.93)$$

This is enforced by the periodic boundary conditions that require continuity of the waveform at the first and last cell of the ring resonator; thus the fundamental resonance corresponds to a wavelength equal to the circumference of the ring. It is clear that the parity is indistinguishable at $k = 0$. Similarly, for the mode at the IR cutoff, when $n = N$, the difference between the clockwise and counterclockwise argument $k\Delta x$ is 2π , thus the two parities are again indistinguishable. This is akin to states at the edge of the Brillouin zone in solid-state systems.

Figure 28 shows the discrete set of resonant frequencies for a 24-cell ideal ring resonator as a function of normalized wavenumber. The ring resonator modes above the IR-cutoff come in pairs of degenerate frequencies, with each pair differing only in the sign of the phase constant. Like the linear LHTL resonator, the $k = 0$ mode diverges for the ring resonator, so it is unmeasurable. The mode at the IR-cutoff frequency is not paired due to the indistinguishable parity. Because of this, the choice to assign a positive value of $k\Delta x$ for the IR-cutoff mode is arbitrary. Thus, a ring resonator with N cells will have $N - 1$ resonant modes with $N/2 - 1$ pairs of degenerate modes above the IR-cutoff.

5.1.1 Stray reactance from lumped circuit elements

As we introduced in Ch. 4, the physical implementation of the lumped circuit elements that comprise the ring resonator have parasitic stray reactances that make the circuit a composite of a left-handed/right-handed ring resonator. The circuit shown in Fig. 29, shows that the series capacitors C_L have stray inductances L_R and the inductors to ground L_L have stray capacitance C_R . As we did for the linear LHRHTL, we can define a self-resonance of the lumped-element capacitors and inductors, given by $\omega_L = 1/\sqrt{C_L L_R}$ and $\omega_C = 1/\sqrt{L_L C_R}$, respectively. The impedance and admittance per unit length for the ring resonator are identical to that of the LHRHTL, so we get an identical expression for the dispersion relation of the ring resonator, given by Eq. (4.91). Figure 30 shows the dispersion for the composite left-handed/right-handed ring compared to a purely left-handed ring as a function of $k\Delta x/\pi$. The dispersion

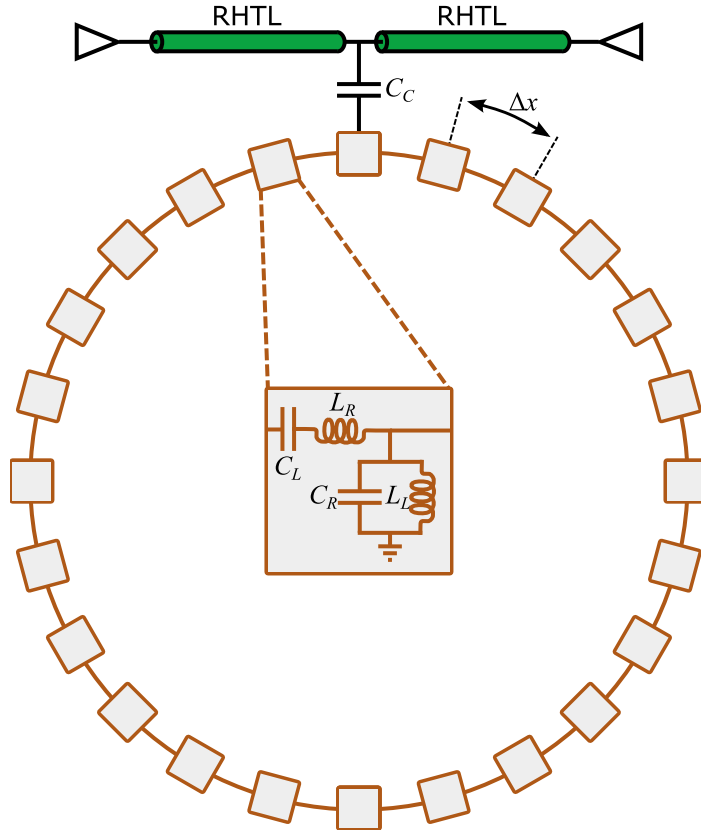


Figure 29: Ring resonator circuit with 24 cells, including parasitic stray reactances. The inset shows a single cell comprised of a series capacitor C_L and inductor L_R shunted to ground by parallel inductor L_L and capacitor C_R .

for the composite left-handed/right-handed ring, accounting for stray reactance, has a discontinuity at $k\Delta x/\pi = 0$ if $\omega_C \neq \omega_L$, where there are no propagating wave solutions. After the zero-crossing point, for $\omega > \max(\omega_C, \omega_L)$, the dispersion transitions from left-handed to right-handed, and k switches sign. Conversely, the ideal ring resonator dispersion diverges as $\pm k\Delta x/\pi$ approaches 0, but this is an unphysical effect as this divergence implies that the group velocity diverges.

5.1.2 Stray reactance from wirebonds

For superconducting microwave devices at the chip scale, chips are mounted or glued to a machined Al sample holder. To ensure a low-impedance microwave ground across the chip, wirebonds are often used to connect the ground plane of the chip to the sample holder. Wirebonds are also used to connect circuit elements on the chip to

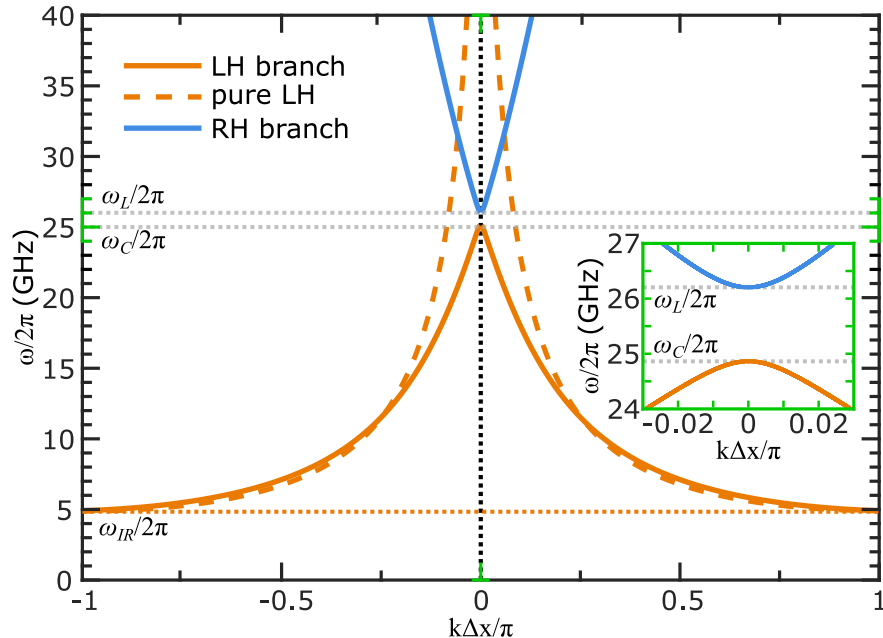


Figure 30: Dispersion relation for a composite left-handed/right-handed ring resonator as a function of normalized mode number with left-handed branches and right-handed branches shown in solid blue and orange lines, respectively. The IR-cutoff frequency ω_{IR} for the ring resonator is shown with an orange dotted line. Orange dashed lines show pure left-handed ring resonator dispersion. The self-resonance of the lumped-element capacitors and inductors, ω_L and ω_C , are shown with gray, dotted lines.

external circuitry [93]. Additional wirebonds can be used to preserve ground-plane continuity between different parts of the chip separated by physical features such as CPW resonators and flux bias lines.

The circuit models shown thus far for the ring resonator, like in Fig. 27, are not optimal designs for physically implementing a ring resonator, because the designs result in a discontinuity in the ground plane depending on which direction the inductors face with respect to the center of the ring. A better method of ensuring that there is a common microwave ground potential across the chip is shown in Fig. 31(a), where a double inductor circuit is used, grounding the ring resonator to both the inside of the ring and the exterior. Similarly, Fig. 31(b) shows a ring resonator cell with double inductors, but also accounting for parasitic stray reactances from the lumped circuit elements. However, even using the double-sided inductor layout shown in Fig. 31(b),

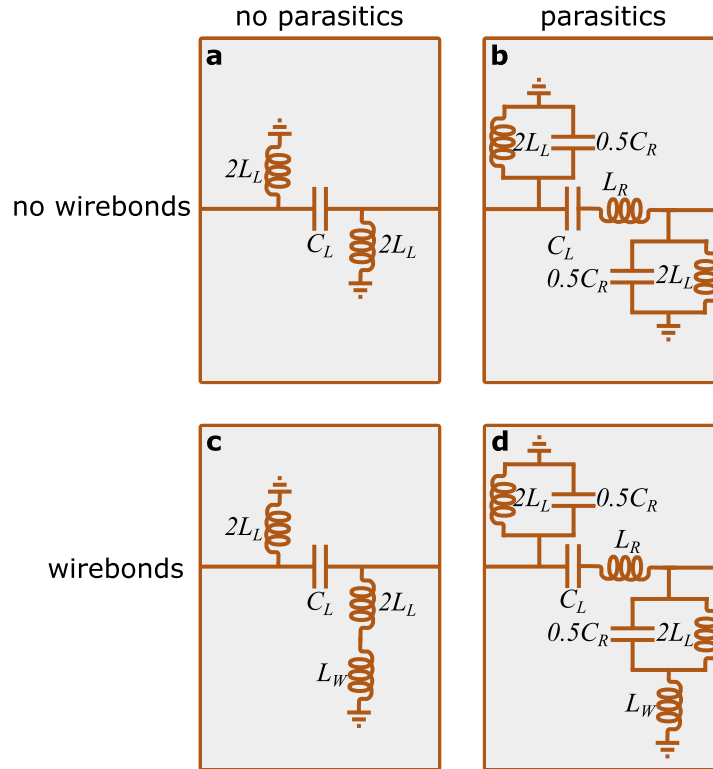


Figure 31: Single-cell circuit schematics for a ring resonator with (c), (d) and without (a), (b) stray inductance from wirebonds and with (b), (d) and without (a), (c) stray parasitic reactance included for the lumped circuit elements.

the lumped-element inductors are discrete and do not provide uniform microwave connectivity between the center of the ring and exterior. Because of this, wirebonds can be applied across the ring resonator to connect the center of the ring to the ground plane exterior to the ring.

Although the superconducting wirebonds provide a zero-resistance dc path connecting the different sections of ground plane, they have a non-negligible inductance and thus contribute stray reactance at microwave frequencies, thus altering the dispersion of electromagnetic waves in the ring resonator. Figure 31(c) and (d) show the single-cell circuits including wirebonds, with and without parasitic reactances from the lumped-element components. If a wirebond is placed across each cell, there is a symmetric change in the dispersion, but as we will show later in this work, when asymmetry is introduced in the circuit via the wirebond position, this results in a lifting of the degeneracy of the even and odd mode frequencies.

5.2 Coupling transmon qubits to a ring resonator

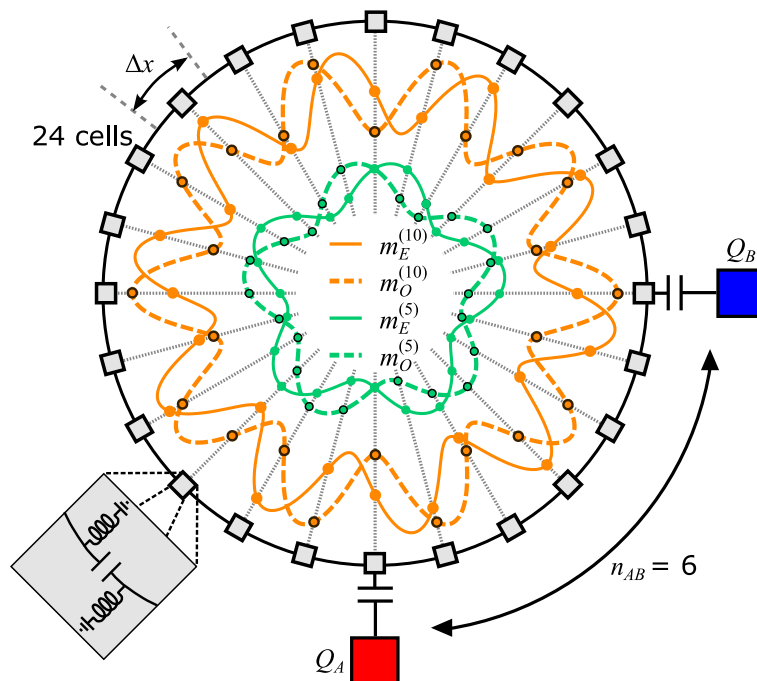


Figure 32: Ring resonator schematic and mode structure for two pairs of degenerate ring resonator modes. The ring resonator model consists of 24 unit cells, shown with gray squares, with each cell containing a capacitor shunted to ground by two inductors. One pair of even (odd) modes with $k\Delta x = 10\frac{2\pi}{N}$ is shown in solid (dashed) orange lines, labeled $m_E^{(10)}$ ($m_O^{(10)}$); a second pair with $k\Delta x = 5\frac{2\pi}{N}$ is depicted with solid (dashed) green lines, labeled $m_E^{(5)}$ ($m_O^{(5)}$). The coupling strength of Q_A and Q_B to each mode is determined by the amplitude of the wave at the cell where the qubit is capacitively coupled to the resonator.

As is the case for a linear LHTL, a left-handed metamaterial ring resonator can be used as a multimode bus to facilitate qubit entanglement, but with the benefit of a small physical footprint and a spectrum that does not depend on matched impedance through the metamaterial, as is the case for a LHTL resonator. The coupling scheme we will discuss is direct, capacitive coupling of the qubits into particular positions around the ring resonator.

Figure 32 shows a circuit comprised of a ring resonator with two qubits capacitively coupled to the ring. In this example, the ring resonator has 24 cells, and the qubit

separation n_{AB} is 6 cells. The mode structures, based on the resonance condition given in Eq. (5.93), for two pairs of degenerate modes are shown for modes with $k\Delta x = 10\frac{2\pi}{N}$ and $k\Delta x = 5\frac{2\pi}{N}$ in orange and green, respectively, with even (odd) parity modes shown with solid (dashed) lines. The g -coupling of the qubits to the multiple modes in the ring resonator depends on the coupling location with respect to the ring resonator cells and with respect to all other externally coupled components around the ring. We will show that g is an oscillatory function with both even and odd solutions corresponding to the even and odd pairs of modes.

5.2.1 Theoretical derivation of Hamiltonian and g -coupling

Given a circuit comprised of a ring resonator with an arbitrary number of cells N and two qubits capacitively coupled around the ring separated by n_{AB} cells, following the derivation performed by our collaborators in Ref. [94] that we reproduce here, we can obtain analytical expressions for the g -coupling values of both qubits to the ring resonator modes. The Lagrangian of the circuit, where we ignore the effect of parasitics and therefore drop the index from C_L and L_L , is given by

$$\begin{aligned} \mathcal{L} = & \frac{1}{2}C \sum_{j=0}^{N-1} (\dot{\phi}_{j+1} - \dot{\phi}_j)^2 - \frac{1}{2L} \sum_{j=0}^{N-1} \phi_j^2 + \frac{1}{2}C_{QM}(\dot{\phi}_{j_A} - \dot{\phi}_A)^2 + \frac{1}{2}C_{QM}(\dot{\phi}_{j_B} - \dot{\phi}_B)^2 \\ & + \frac{1}{2}C_S\dot{\phi}_A^2 + \frac{1}{2}C_S\dot{\phi}_B^2 + E_J^A(\Phi_{ext}^A) \cos\left(\frac{\phi_A}{\Phi_0}\right) + E_J^B(\Phi_{ext}^B) \cos\left(\frac{\phi_B}{\Phi_0}\right). \end{aligned} \quad (5.94)$$

Here, Φ_0 is the magnetic flux quantum, ϕ_j is the flux at node j and $j_{A/B}$ denotes the cell number that is connected to $Q_{A/B}$. In the following we will assume that the number of cells between the two qubits $n_{AB} := j_A - j_B$ is even. This complies with the device setup of $n_{AB} = 6$. Since n_{AB} is even, we can place cell number 0 between the qubits, which now have the indices $j_A = \frac{n_{AB}}{2}$ and $j_B = -\frac{n_{AB}}{2}$. This choice of reference frame is without loss of generality for qubits separated by an even number of cells. As introduced in Ch. 3, since each transmon has a dc SQUID for its Josephson element, the flux-dependent Josephson energy is given by $E_J^q(\Phi_{ext}^q) = E_{J_0}^q \cos\left(\frac{\pi\Phi_{ext}^q}{\Phi_0}\right) \sqrt{1 + d_q^2 \tan^2\left(\frac{\pi\Phi_{ext}^q}{\Phi_0}\right)}$, where $E_{J_0}^q = E_{J_1}^q + E_{J_2}^q$ gives the maximum total Josephson energy for qubit $q = A, B$, accounting for the energy contributions of the two junctions that make up the SQUID loop, $E_{J_1}^q$ and $E_{J_2}^q$. Here, d_q is the junction asymmetry, defined as $d_q = \frac{E_{J_2}^q - E_{J_1}^q}{E_{J_1}^q + E_{J_2}^q}$. The external flux, Φ_{ext}^q , is the flux

coupled to the SQUID loop for each qubit q . C_S is the shunt capacitance of each qubit and C_{QM} is the qubit-resonator coupling capacitance.

We can introduce the canonical variables of Cooper pair numbers $n_j = \frac{1}{2e}Q_j = \frac{1}{2e} \frac{\partial \mathcal{L}}{\partial \dot{\phi}_j}$ and their Fourier transform $n_k = \frac{1}{\sqrt{N}} \sum_j e^{ik\Delta x j} n_j$, where $k\Delta x/\pi \in [-1 + \frac{2}{N}, -1 + \frac{4}{N}, \dots, 1 - \frac{2}{N}, 1]$ form a Brillouin zone. This notation makes it immediately clear that for most k values there is a corresponding $-k$ modes, where positive k values correspond to modes traveling around the ring resonator clockwise and negative k values correspond to counterclockwise moving modes. As previously stated, the values of $k\Delta x/\pi = 1$ and $k\Delta x/\pi = 0$ do not have a corresponding $-k$ value, as they are at the edge and the origin of the first Brillouin zone, respectively. The $k\Delta x/\pi = 1$ state we have identified as the IR mode, is not paired with any other $-k$ state and will show no degeneracy with another mode. A similar argument can be made for the $k\Delta x/\pi = 0$ state, which corresponds to the highest frequency mode. In this derivation only the degenerate states are considered, as they comprise the majority of resonances for which an expression of $g(\omega)$ may be obtained. An equation for the g -coupling of the IR mode needs to be calculated separately, which can be done in a similar manner, but will not be shown here.

For the Fourier-transformed canonical variables, we get

$$\begin{aligned} \dot{\phi}_k = L\omega^2(k) & \left(2en_{-k} + \frac{1}{\sqrt{N}} C_{QM} (\dot{\phi}_{n_{AB}/2} - \dot{\phi}_A) e^{-ik\frac{x_{AB}}{2}} \right. \\ & \left. + \frac{1}{\sqrt{N}} C_{QM} (\dot{\phi}_{-n_{AB}/2} - \dot{\phi}_B) e^{ik\frac{x_{AB}}{2}} \right), \end{aligned} \quad (5.95)$$

with the distance between the qubits given by $x_{AB} = n_{AB}\Delta x$, and the left-handed dispersion relation for $\omega(k)$ given by Eq. (5.92). The scaling with ω^2 is unique to left-handed materials and causes a different frequency dependence for the g values than for a system with qubits coupled to a right-handed set of modes. Here $\dot{\phi}_k$ is expressed in terms of n_{-k} , further highlighting the symmetry between k and $-k$, which is only broken by the qubit terms. Next, we renormalize the flux to $\varphi = \phi/\Phi_0$, ignore the coupling to the IR mode and the highest frequency mode, and only focus on the paired modes. We transform into even and odd modes using the change of

variables

$$n_{k,E/O} = \frac{1}{\sqrt{2}} \left(n_k \pm n_{-k} \right),$$

$$\varphi_{k,E/O} = \frac{1}{\sqrt{2}} \left(\varphi_k \pm \varphi_{-k} \right),$$

and introduce the notation $C_{rat} = \frac{C_{QM}}{C_{QM} + C_S}$. The total Hamiltonian can be broken into components given by $H_{tot} = H_{res} + H_A + H_B + H_{AB}^{int} + H_{mode}^{int} + H_E^A + H_O^A + H_E^B + H_O^B$. All of these Hamiltonian terms will be defined in the remainder of this section. In this derivation, we are assuming that the interaction between resonator modes mediated by the qubits is small with respect to the other terms. This assumption is valid when the magnitude of g is smaller than the mode frequency separation. Our examples have been based on a 24-cell ring resonator, corresponding to our experimental device. In the ideal case, no modes are close enough together to invalidate this assumption when C_{QM} is assumed to correspond to typical coupling strengths used in cQED for coupling qubits to cavities. So, without explicit proof, we use this assumption, but it is not true in general. The Hamiltonian terms for the resonant modes H_{res} and the qubits $H_{A/B}$ are given by

$$H_{res} = 2e^2 \sum_{k>0} L\omega^2(k) (n_{k,E}^2 - n_{k,O}^2) + \frac{\Phi_0^2}{2L} \sum_{k>0} (\varphi_{k,E}^2 - \varphi_{k,O}^2),$$

$$H_{A/B} = \frac{2e^2}{C_S} \left(1 - \frac{1}{1 - s_{AB}^2} K^2 C_{rat}^2 \frac{C_S}{C_{QM}} \right) n_{A/B}^2 - E_J^{A/B} \cos(\varphi_{A/B}),$$

with $\frac{1}{K} = 1 + \frac{C_{QM}}{N}(1 - C_{rat}) \sum_k L\omega^2(k)$ and $s_{AB} = K \frac{C_{QM}}{N} (1 - C_{rat}) \sum_k L\omega^2(k) e^{ikx_{AB}}$. The capacitive interaction between the two qubits, mediated by the ring resonator capacitances can be expressed as

$$H_{AB}^{int} = \frac{4e^2 s_{AB}}{(1 - s_{AB}^2)^2} \frac{K^2 C_{rat}^2}{C_{QM}} n_A n_B.$$

The interaction between one of the qubits and an even and odd mode can be expressed as

$$H_E^{A/B} = \alpha_E^{A/B} \frac{1}{\sqrt{N}} \sum_{k>0} \omega^2(k) \cos\left(k \frac{x_{AB}}{2}\right) n_{k,E} n_{A/B},$$

$$H_O^{A/B} = \pm \alpha_O^{A/B} \frac{1}{\sqrt{N}} \sum_{k>0} \omega^2(k) \sin\left(k \frac{x_{AB}}{2}\right) n_{k,O} n_{A/B},$$

respectively. For $H_O^{A/B}$ the + branch is for qubit A and $-$ is for B . If we assume both qubits have the same shunt capacitance and the same coupling capacitance, the prefactors are independent of the qubits and given by

$$\alpha_E = 2\sqrt{2}e^2L \frac{K^2}{1 - s_{AB}^2} \frac{1}{1 + s_{AB}} C_{rat}(1 - C_{rat}),$$

$$\alpha_O = -2\sqrt{2}e^2L \frac{K^2}{1 - s_{AB}^2} \frac{1}{1 - s_{AB}} C_{rat}(1 - C_{rat}).$$

We can now express the flux and charge operators in terms of creation and annihilation operators a^\dagger and a :

$$\varphi = \varphi_{zpf}(a + a^\dagger),$$

$$n = i n_{zpf}(a - a^\dagger).$$

We can identify the zero point fluctuation of the charge as $n_{zpf} = \sqrt{\frac{\hbar}{2eL\omega}}$, which scales with $1/\sqrt{\omega}$. Similarly, the zero point fluctuations of the charge for each qubit scales with $\sqrt{\omega_{A/B}}$. We redefine the proportionality factors $\alpha_{E/O}^{A/B}$ to include the zero point fluctuations, except for their frequency dependence, and label them as $\alpha_{E/O}^{A/B'}$. By only considering terms that conserve excitation number based on the rotating wave approximation (RWA), the coupling Hamiltonian reduces to

$$H_E^{A/B} = \alpha_E^{A/B'} \frac{1}{\sqrt{N}} \sum_{k>0} \sqrt{\omega_{A/B}} \omega^{\frac{3}{2}}(k) \cos\left(k \frac{x_{AB}}{2}\right) (a_{k,E}^\dagger a_{A/B} + a_{k,E} a_{A/B}^\dagger)$$

$$H_O^{A/B} = \pm \alpha_O^{A/B'} \frac{1}{\sqrt{N}} \sum_{k>0} \sqrt{\omega_{A/B}} \omega^{\frac{3}{2}}(k) \sin\left(k \frac{x_{AB}}{2}\right) (a_{k,O}^\dagger a_{A/B} + a_{k,O} a_{A/B}^\dagger).$$

With this Hamiltonian we arrive at an expression for the g -coupling values as a function of k and $\omega(k)$

$$g_E^{A/B}(k) = \alpha_E^{A/B'} \frac{1}{\sqrt{N}} \sqrt{\omega_{A/B} \omega^3(k)} \cos\left(k \frac{x_{AB}}{2}\right),$$

$$g_O^{A/B}(k) = \pm \alpha_O^{A/B'} \frac{1}{\sqrt{N}} \sqrt{\omega_{A/B} \omega^3(k)} \sin\left(k \frac{x_{AB}}{2}\right).$$

Using the dispersion relation of left-handed materials, we can also express this in terms of the frequency. In the case of a simple dispersion relation without parasitics, this gives us

$$g_E^{A/B}(\omega_{rE}) = \alpha_E^{A/B'} \frac{1}{\sqrt{N}} \sqrt{\omega_{A/B} \omega_{rE}^3} \cos\left(\frac{n_{AB}}{2} \arcsin\left(\frac{\omega_{rE}}{\omega_{rO}}\right)\right),$$

$$g_O^{A/B}(\omega_{rO}) = \pm \alpha_O^{A/B'} \frac{1}{\sqrt{N}} \sqrt{\omega_{A/B} \omega_{rO}^3} \sin\left(\frac{n_{AB}}{2} \arcsin\left(\frac{\omega_{rE}}{\omega_{rO}}\right)\right).$$

Note that the proportionality constants $\alpha_{E/O}^{A/B'}$ and $\alpha_{E/O}^{B/O'}$ can be either positive or negative, but always have the same sign. Therefore we do not determine the actual sign of the g -couplings to the modes without explicit calculation of the proportionality constants, and only the relative sign between the interactions of each mode to Q_A and Q_B is given. We refer to this as the parity of the modes or the parity of the g -couplings. Modes with even parity share the same sign between Q_A and Q_B and modes with odd parity have opposite signs for Q_A and Q_B . We can write a simplified expression that relates the g -coupling for each qubit to the mode frequency and qubit position, given by:

$$g_E^B(k) = g_E^A(k) \propto \frac{\omega^{\frac{3}{2}}(k)}{\sqrt{N}} \cos\left(k \frac{x_{AB}}{2}\right), \quad (5.96)$$

$$-g_O^B(k) = g_O^A(k) \propto \frac{\omega^{\frac{3}{2}}(k)}{\sqrt{N}} \sin\left(k \frac{x_{AB}}{2}\right). \quad (5.97)$$

Here, we have removed the proportionality constant and qubit frequency, but the oscillatory behavior and scaling as a function of mode frequency is preserved. Referring back to the circuit schematic shown in Fig. 32, the solid line is a cosine and the dashed line is a sine mode, or equivalently an even and odd mode. The origin is located in the middle between the qubits, thus clarifying the signs in Eqs. (5.96) and (5.97), as Q_A is connected to cell number $n_{AB}/2$, and Q_B to $-n_{AB}/2$.

From these derivations, we have shown that we can describe a ring resonator that is capacitively coupled to two weakly-anharmonic qubits, Q_A and Q_B , separated by n_{AB} cells around the ring, as shown in Fig. 32. Again, using the standard circuit quantization within the rotating wave approximation, the total Hamiltonian, accounting

for both even and odd ring resonator modes, reads [52]

$$\begin{aligned}
H/\hbar = & \sum_q \left[\omega_q \hat{a}_q^\dagger \hat{a}_q + \frac{\delta_q}{2} \hat{a}_q^\dagger \hat{a}_q (\hat{a}_q^\dagger \hat{a}_q - 1) \right] \\
& + \sum_{|k|,P} \omega(k) \hat{r}_{k,P}^\dagger \hat{r}_{k,P} + \sum_{|k|,P,q} g_P^q(k) (\hat{r}_{k,P}^\dagger \hat{a}_q + \hat{r}_{k,P} \hat{a}_q^\dagger), \tag{5.98}
\end{aligned}$$

with $\hat{a}_q^\dagger(\hat{a}_q)$ being the creation (annihilation) operator of qubit $q = A, B$ and δ_q being the qubit anharmonicity. Here $\hat{r}_{k,P}^\dagger(\hat{r}_{k,P})$ are the creation (annihilation) operator of ring resonator mode k and parity $P = E, O$, and the qubit-resonator mode coupling strengths $g_P^q(k)$ we have just derived is given in Eq (5.96) and (5.97).

Figure 33 shows the oscillatory nature of the g -couplings as a function of mode frequency. Thus far, our examples have dealt with 24-cell left-handed devices, but for better visualization of the oscillations, we consider a ring with $N = 240$ unit cells. To compare these g -coupling values to the circuit schematic shown in Fig 32, the qubit-qubit cell separation is the same, $n_{AB} = 6$. Since the cosine and sine functions that describe g for the two qubits do not depend on N , scaling from $N = 24$ to $N = 240$ does not affect the oscillations, and the solutions only differ by a proportionality constant. In Fig. 33, the analytical expressions of Eqs. (5.96) and (5.97) are compared with numerical values obtained from explicit solutions to the Hamiltonian in Eq. (5.98) for each of the resonant frequencies of the 240-cell ring resonator. These numerical solutions predict the same odd (gray) and even (purple) parity behavior.

In the next chapters, we will experimentally investigate a ring resonator bus coupling two qubits. It is important to note that while the analytic expression and numerical solutions for g have an associated sign, direct measurement of the sign of g is not possible when observing vacuum Rabi splittings, as shown in Fig. 7. Determining the parity of the g -couplings is crucial for calculation of the effective J -coupling between qubits; Eq. (3.52) shows that J depends on the product of the g -coupling strength for each qubit. Additionally, because of the stray reactance from wirebonds used to ground the ring resonator described in Sec 5.1.2, when the distribution of wirebonds is not uniform, variations in the even and odd modes leads to small shifts in g which may be difficult to model. These points will be discussed in the chapters that follow.

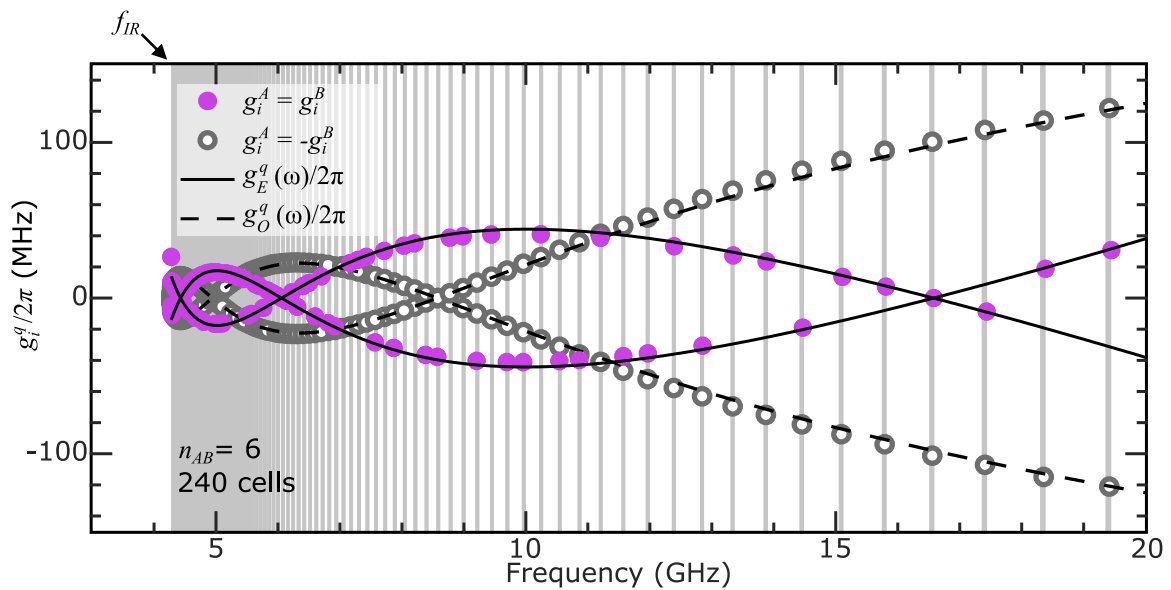


Figure 33: Theoretical g -coupling values for Q_A and Q_B , coupled to a hypothetical 240-cell ring resonator with qubit separation $n_{AB} = 6$. Simulated data points at which the coupling for Q_A , $g_i^A/2\pi$, and for Q_B , $g_i^B/2\pi$, share the same sign for a given mode are shown in purple. Points at which the g_i^A and g_i^B coupling to Q_A and Q_B , respectively, have opposite signs are shown in gray.

Chapter 6

Device Design

Implementing a device comprising a left-handed metamaterial ring resonator coupled to qubits involves numerous design considerations. The following sections outline the details of the physical elements within the device, focusing on the ring resonator and qubit designs individually first, then zooming out to look at the device design as a whole.

6.1 Ring resonator design

Chapter 5 describes a left-handed metamaterial ring resonator implemented with a chain of lumped circuit elements comprised of series capacitors shunted to ground by inductors. The physical implementation of the ring resonator has a number of design constraints.

Design of the inductors and capacitors is guided by fundamental and practical constraints. The infrared cutoff frequency, or the frequency of the first mode in the spectrum, is given by $\omega_{IR} = 1/2\sqrt{C_L L_L}$, where C_L and L_L are the unit cell capacitance and inductance, respectively. The target infrared cutoff frequency is designed such that the infrared cutoff mode and several modes at higher frequencies sit within the bandwidth of the standard microwave electronics ($\sim 2-12$ GHz). Additionally, we will be coupling superconducting qubits into the ring resonator with the intention of coupling several modes from the densest region of the ring resonator spectrum to the qubits. This narrows the range of $\omega_{IR}/2\pi$ to the typical operation frequency range of superconducting qubits, $\sim 4-9$ GHz. In Chapter 3, we discussed flux tunable

Ring resonator cell parameters			
Parameter	Simulation	Theory	Description
L_L (nH)	0.8	1.04	Unit cell inductance
C_L (fF)	303	303	Unit cell capacitance
L_R (nH)	0.12	0.12	Unit cell stray inductance
C_R (fF)	50	50	Unit cell stray capacitance
C_D (fF)	371	371	Center disk capacitance
C_C (fF)	16	16	Coupling capacitance

Table 1: Ring resonator cell parameters obtained via finite element simulation. Unit cell capacitance C_L , total center disk capacitance C_D , and coupling capacitance C_C of the ring to external feedline are obtained using Ansys Q3D software. Unit cell inductance and wirebond inductance, L_L determined using InductEx software. The stray inductance and capacitance, L_R and C_R , were found using Sonnet software to identify the self resonances of the lumped-element unit-cell structures. The values in the theory column come from modeling of the device and adjusting parameters to match the measured ring resonator spectrum. The discrepancy between the theoretical and simulated values for L_L are likely due to imperfect grounding and approximations used in estimating the inductive contributions of the wirebonds based on extracted lengths from microscope images.

transmon qubits and the flux insensitive sweet spots of the qubit transition frequency in which the qubit lifetime is the longest. With this in mind, the ideal ring resonator would have an infrared cutoff frequency above the minimum transition frequency of the coupled qubits. This gives a target infrared cutoff frequency of approximately 5 GHz.

Each unit cell consists of a superconducting island with a capacitor for a series connection to the next unit cell, plus two inductors to ground. The total number of unit cells determines the number of resonant modes in the spectrum. For a left-handed metamaterial ring resonator, there is an infrared cutoff mode, then pairs of degenerate modes with increasing frequency, as discussed in Ch. 5. For a pure, left-handed ring resonator, we expect $N - 1$ modes for a ring resonator with N cells. There

is a practical limit to the number of cells set by the size scale of the lumped circuit elements and the chip size. The lumped elements are implemented from thin-film Nb structures similar to those used in various cQED architectures. The capacitors are an interdigitated design comprised of 15 pairs of $4\text{-}\mu\text{m}$ wide and $110\text{-}\mu\text{m}$ long fingers separated by a $1\text{-}\mu\text{m}$ gap. We use a planar, meander-line inductor design with a trace width of $2\text{-}\mu\text{m}$ and 20 turns. The dimensions of the lumped circuit elements are extracted from finite element simulation and informed by previous left-handed metamaterial designs [37]. Each lumped circuit element has an associated parasitic reactance set by the geometry of the element. These parasitic reactances make the physical implementation of the ring resonator a hybrid left-handed and right-handed resonator. The associated parasitic reactance for C_L and L_L , L_R and C_R , respectively, can be ascertained from finite element simulation of the self-resonance of the lumped circuit element using Sonnet’s electromagnetic solver. The parameters for the left-handed ring-resonator are given in Table 1.

For this device, the ring resonator capacitors are designed with inductors to ground towards both the exterior and interior of the ring to improve grounding of the center disk inside the ring resonator. Accounting for only the unit-cell capacitances and inductances, the IR-cutoff for this device is simulated to be 4.8 GHz.

6.2 Qubit design

Chapter 3 introduced the floating-style transmon widely used in quantum computing applications. The two identical qubits coupled to the ring resonator were designed in this floating-style with inductively coupled on-chip flux lines allowing in situ tuning of the qubit transition frequency. In this section, we share details of the qubit island design as well as select measurements characterizing the qubits. Further details on the measurement setup are given in Chapters 7 and 8.

The qubit details are given in Table 2. We determined $E_{j_0}^A$ and $E_{j_0}^B$ by fitting spectroscopy data to a characteristic asymmetric transmon curve, given by Eq. 3.19. This fit and the spectroscopy data are shown in Fig. 34. This method was implemented because we did not directly measure the qubit maximum transition frequency due to challenges in the chip design. The values for E_C^A and E_C^B were calculated using

Parameter	Value	Description
$E_{J_0}^A/h$	23.8 GHz	Maximum Josephson energy, Q_A
$E_{J_0}^B/h$	25.7 GHz	Maximum Josephson energy, Q_B
E_C^A/h	243 MHz	Charging energy, Q_A
E_C^B	223 MHz	Charging energy, Q_B
d_A	0.38	Junction asymmetry, Q_A
d_B	0.39	Junction asymmetry, Q_B
T_1^A	19.1 μ s	Relaxation time at $\Phi/\Phi_0 = 0.5$, Q_A
T_1^B	19.4 μ s	Relaxation time at $\Phi/\Phi_0 = 0.5$, Q_B
f_C^A	6.358 GHz	Bare cavity frequency, Q_A
f_C^B	6.166 GHz	Bare cavity frequency, Q_B
Q_C^A	3,590	Coupling quality factor of readout cavity, Q_A
Q_C^B	3,290	Coupling quality factor of readout cavity, Q_B
$g_R^A/2\pi$	40 MHz	Coupling between qubit and readout cavity, Q_A
$g_R^B/2\pi$	45 MHz	Coupling between qubit and readout cavity, Q_B
C_S	83 fF	Shunt capacitance
C_{QR}	2.5 fF	Qubit-readout resonator coupling capacitance
C_{QM}	17.5 fF	Qubit-ring resonator coupling capacitance

Table 2: Parameters for two transmon qubits, Q_A and Q_B . Method of determination for each parameter is given in the text.

Hamiltonian modeling of E_C as a function of anharmonicity extracted from independent measurement of the qubit's f_{01} and $f_{02}/2$ transition frequencies, as described in Sec. 3.1. The bare readout cavity frequency for Q_A is 6.358 GHz and 6.166 GHz for Q_B . From the fits of the spectroscopy data for different flux bias to the asymmetric transmon tuning curve, we extract the maximum transition frequencies for Q_A and Q_B to be 6.58 GHz and 6.59 GHz, respectively. The proximity of the qubit upper sweetspot to the readout cavity and nearby mode frequencies results in Purcell loss and broad qubit linewidths, making a direct determination of the maximum transition frequencies of the qubits challenging. The qubit coherence times, T_1^A and T_1^B , are determined via independent measurements with each qubit's flux bias tuned to its flux-insensitive lower sweet spot. We extracted the coupling strength of qubits Q_A

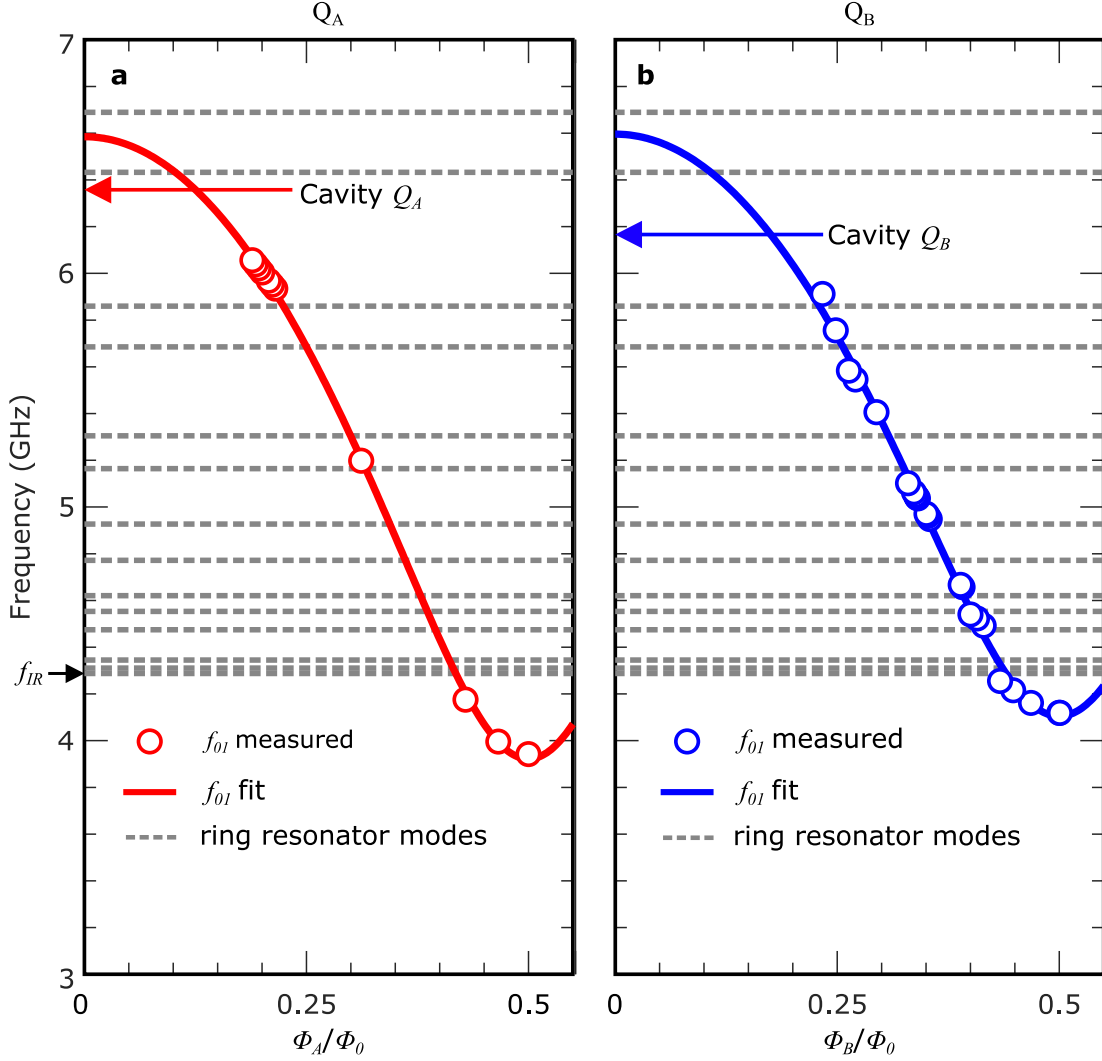


Figure 34: Characteristic transmon curve fit for f_{01} transition of (a) Q_A and (b) Q_B , shown in solid red and blue lines, respectively. Red(blue) circles show spectroscopy data for $Q_A(Q_B)$ used in the fit. Gray, dashed lines denote bare ring resonator mode frequencies.

and Q_B to their respective readout resonators, $g_R^A/2\pi$ and $g_R^B/2\pi$ via dispersive cavity shift measurements. The effective qubit island capacitances, including the shunt capacitance, C_S , and the coupling capacitances of the qubit to the ring resonator and to the qubit readout resonator, C_{QM} and C_{QR} , respectively, are determined using finite element simulation and converting the capacitance matrix for a floating-style qubit to a standard transmon circuit model, as described in Sec. 3.1.

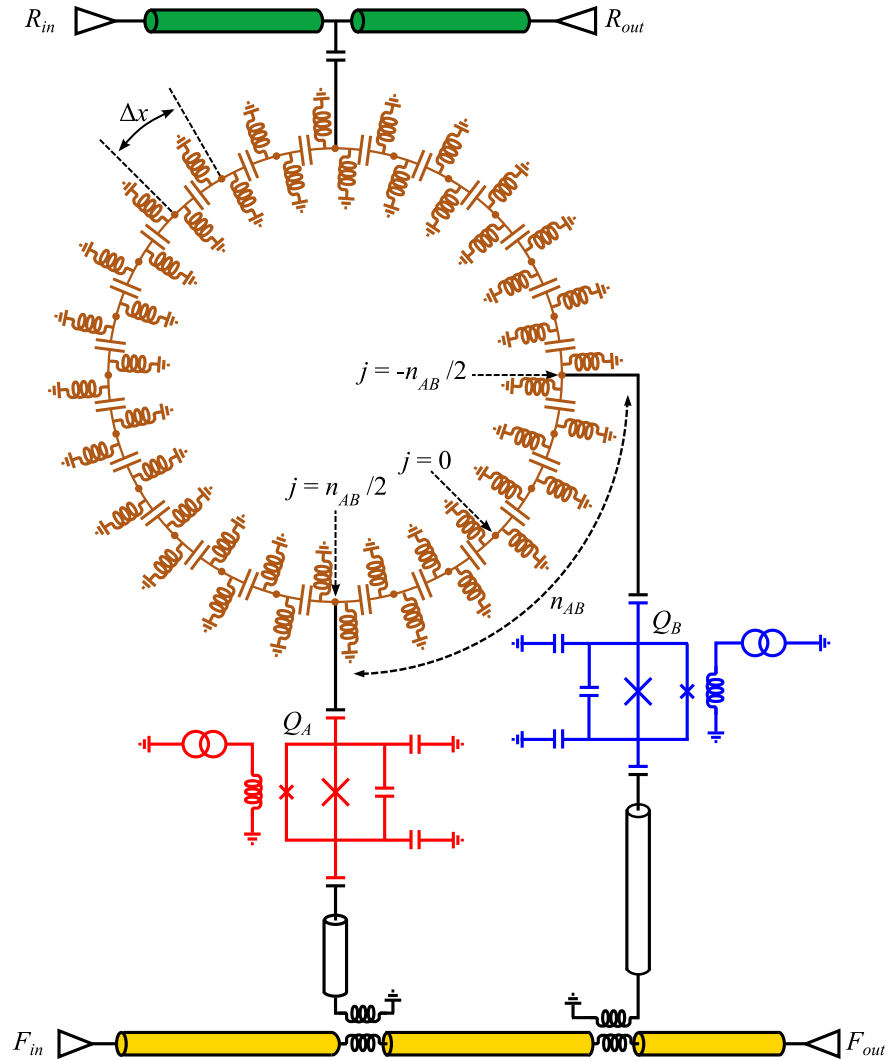


Figure 35: Full circuit schematic. Microwave readout is performed via right-handed transmission lines labeled R_{in}/R_{out} and F_{in}/F_{out} in green and yellow, respectively. The 24-cell ring-resonator circuit is shown in orange. Capacitively coupled qubits, Q_A and Q_B , are shown in red and blue, respectively, and are separated by a distance of $n_{AB} = 6$. Qubit readout cavities are comprised of quarter-wave coplanar waveguide resonators.

6.3 Device layout

The device consists of a 24-cell, left-handed superconducting metamaterial ring-resonator comprised of interdigitated capacitors with double-sided meander-line inductors to ground. A full circuit diagram of the device is shown in Fig. 35. Figure 36

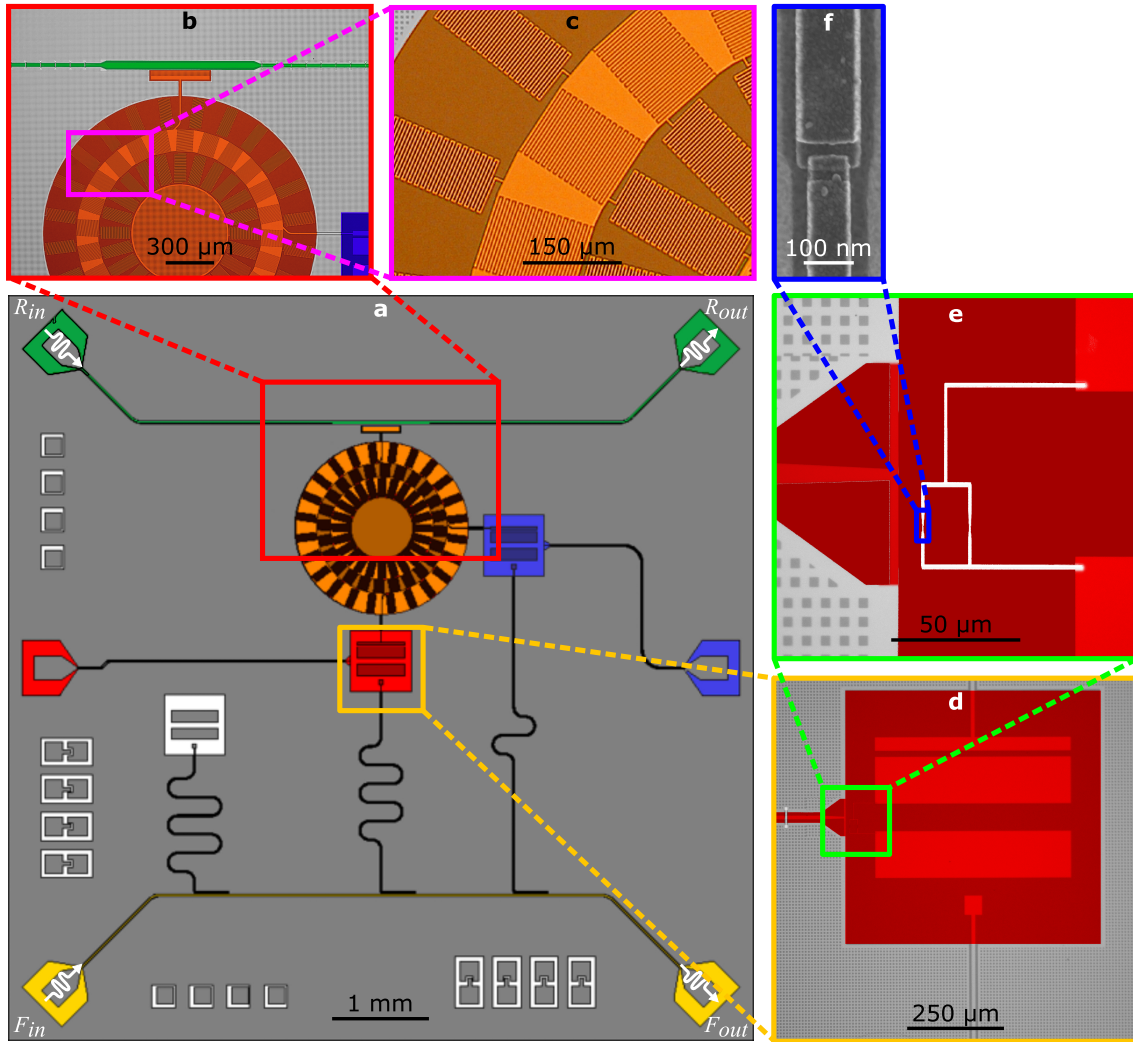


Figure 36: (a) Chip layout for metamaterial ring-resonator device. (b-e) Optical micrographs of device with false-color highlighting. (f) SEM image of Josephson junction in qubit.

shows the chip layout and details of the device features. The ring resonator is capacitively coupled to a feedline, labeled (R_{in}/R_{out}) as shown in Fig. 36(a), for probing ring-resonator modes. Two flux-tunable, floating-style asymmetric transmon qubits [51], Q_A and Q_B , are capacitively coupled to the ring resonator 90 and 180 degrees from the feedline coupling point, respectively. Both qubits have readout resonators inductively coupled to a separate feedline, F_{in}/F_{out} , as well as separate on-chip flux-bias lines for tuning the transition frequency of the qubits.

6.4 Fabrication details

The base layer of the ring resonator device is comprised of 60-nm thick sputtered niobium on a high resistivity ($> 10 \text{ k}\Omega\text{-cm}$) 100-mm silicon wafer. Before sputtering, the silicon wafer undergoes a standard RCA clean process and an oxide etch in a buffered 2% HF solution to remove native oxides. The photolithography patterning is performed by a DUV wafer stepper, and the niobium is etched in an ICP etcher using BCl_3 , Cl_2 , and Ar. All resist is stripped in a TMAH hot strip bath and an oxygen plasma cleaning is performed to remove residual resist residue. We then perform a second 20% buffered HF etch to reduce surface oxides. The device has ground straps along the feedlines labeled R_{in}/R_{out} and F_{in}/F_{out} , as well as the flux-bias lines. Patches of evaporated SiO_2 isolate the straps from the signal traces, and sputtered aluminum provides the electrical ground connection, both patterned via a standard lift-off process. The junctions are patterned using 100 keV electron-beam lithography of a PMMA/MMA bilayer resist stack, then deposited via a conventional double-angle shadow-evaporation process.

6.5 Measurement setup

The fabricated devices are diced into 8-mm chips, then mounted in an aluminum sample box using GE Varnish to adhere the chip to an aluminum shelf within the sample package. The sample is then grounded to the sample package with aluminum wirebonds. Additional wirebonds are added to preserve grounding across features that do not have fabricated crossovers. The feedlines and flux lines are wirebonded to copper circuit boards traces that are mounted in the sample box and soldered to SMA connectors. The mounted and bonded chip can be seen in Fig. 40(a). We connect RF coaxial cables in the cryostat to these SMA connectors. The sample is covered with an aluminum lid to provide a complete electrical enclosure while shielding the device from blackbody radiation from warmer stages of the cryostat. Additionally, because the aluminum of the sample box becomes superconducting, it serves as a Meissner shield to screen out stray magnetic fields.

Measurements are performed on a Bluefors cryogen-free dilution refrigerator below 15 mK. The sample is mounted on a cold-finger made from OFHC copper at the

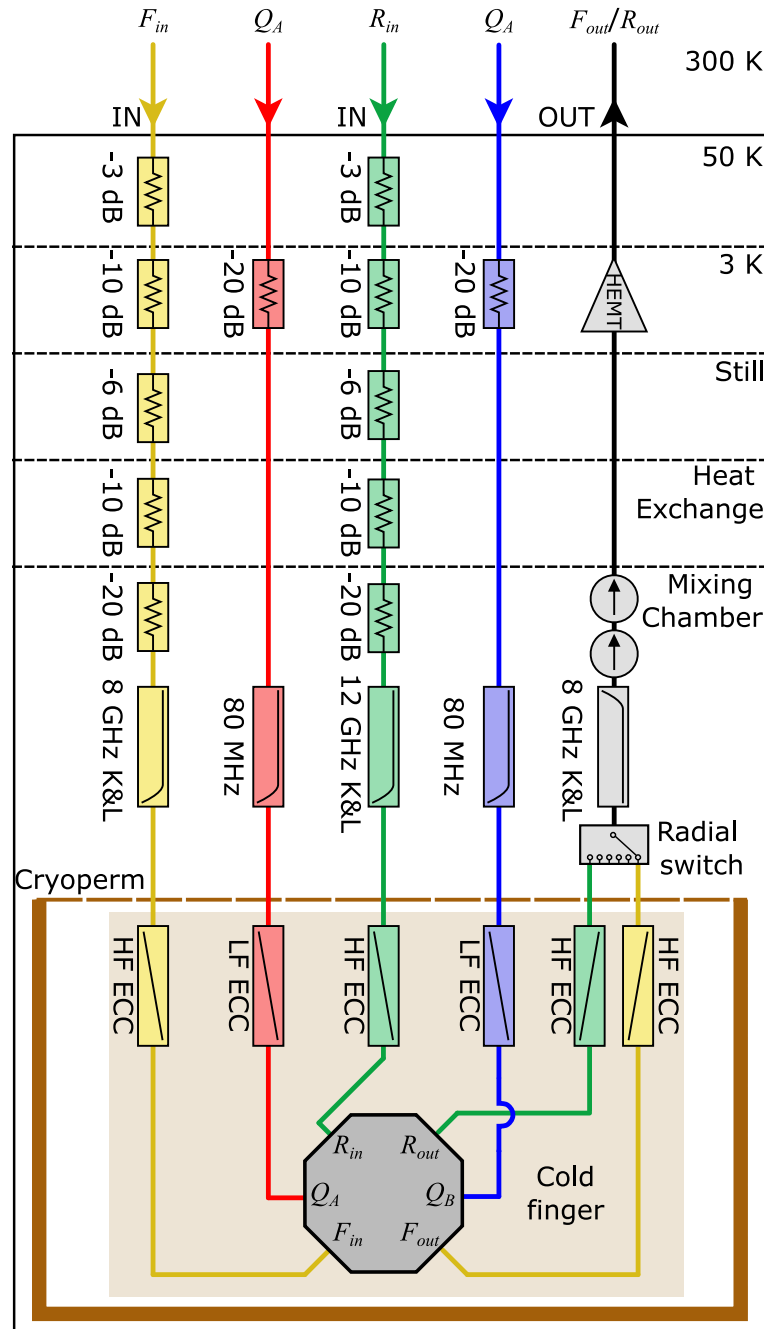


Figure 37: Schematic of the wiring within the dilution refrigerator.

mixing chamber (MXC) stage. A cryoperm shield around the cold-finger provides a layer of magnetic shielding. Figure 37 shows details on the cabling and shielding setup in the dilution refrigerator. An infrared-absorbent layer is applied to the inner surfaces of the Cryoperm magnetic shield and the MXC shield comprised of silica

powder, fine carbon powder, and SiC grains in Stycast low-temperature epoxy [95]. Each temperature stage has a light-tight shield surrounding the lower stages. The room-temperature stage has a mu-metal shield within the vacuum can that provides protection from external magnetic fields. The input lines to the ring resonator and to the qubit feedline are connected to the top of the dilution refrigerator through semi-rigid cables with 49 dB of cold attenuation for thermalization. A Radial relay switch on the output line allows switching between measurements via the two feedlines, R_{in}/R_{out} and F_{in}/F_{out} . This output line is amplified 32 dB with a 4-8 GHz HEMT mounted on the 3 K stage, and amplified again with a room-temperature parametric amplifier (NARDA West) with 35 dB gain.

Measurements are performed using a standard heterodyne readout, shown in Fig. 38, unless otherwise stated. This method uses the interaction between the qubit and readout resonator to encode information about the state of the system. Heterodyne readout allows us to observe both the frequency and phase response through the feedline, allowing us to acquire information about the quantum state of the system through the measured phase. In general, heterodyning is a nonlinear process by which two signals are converted to a third signal at the sum or difference frequency of the original signals. We perform signal up-conversion by mixing an intermediate frequency (IF) with a local oscillator (LO) frequency to produce an RF signal with the desired waveform, envelope, and phase in the range of our measurement setup, 4-8 GHz. This signal is transmitted via the qubit feedline, and the returned signal is down-converted to the MHz frequency range and digitized. To extract information about the qubit state, as we showed in Ch. 3, we can discern the state of the qubit via the qubit state-dependent dispersive cavity shift.

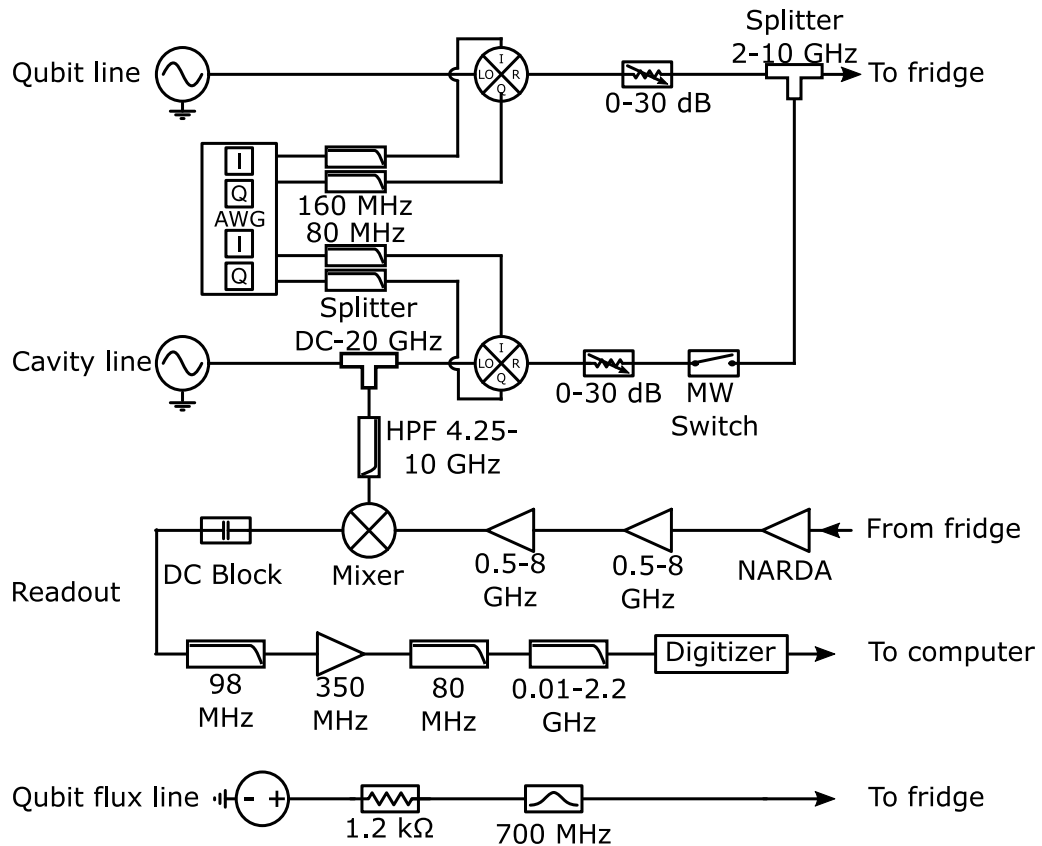
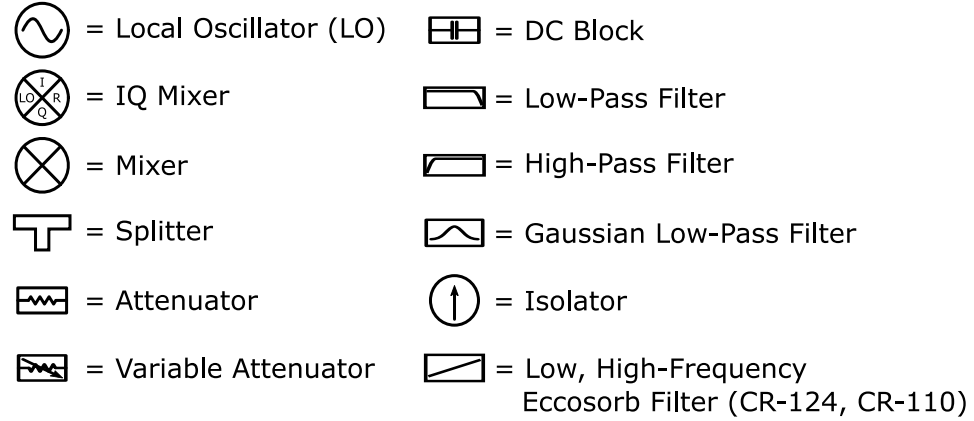
Legend

Figure 38: Wiring diagram for standard heterodyne setup used for readout.

Chapter 7

Ring resonator mode structure and g -coupling

We begin characterization of this device by looking at microwave transmission measurements taken via the ring resonator feedline. The ring resonator is shown to have a dense mode spectrum within the frequency range allowable by our measurement setup, and the spectrum is sensitive to asymmetries in the ring resonator circuit. We then look at the coupling strength between the two qubits to each of the ring resonator modes in the measurement range achievable with our microwave setup. Using these parameters, we can learn more about the inter-qubit interactions mediated by the ring resonator.

7.1 Measurement of ring resonator spectrum

First, we observe the ring resonator spectrum measured via the ring resonator feedline, R_{in}/R_{out} , as shown in the device layout in Fig. 36 in Ch. 6. Transmission measurements via the ring resonator feedline are primarily performed using a vector network analyzer (VNA). The matrix element S_{21} is used for our measurement setup to characterize transmission through the ring resonator. In Eq. (3.47) in Ch. 3, we define S_{21} in terms of scattering parameters for an ideal design with load impedance matched to the source impedance at the input of the resonator.

Figure 39 shows the raw spectrum of the ring resonator measured at high power over a wide frequency span. The ring resonator has an infrared cutoff frequency of

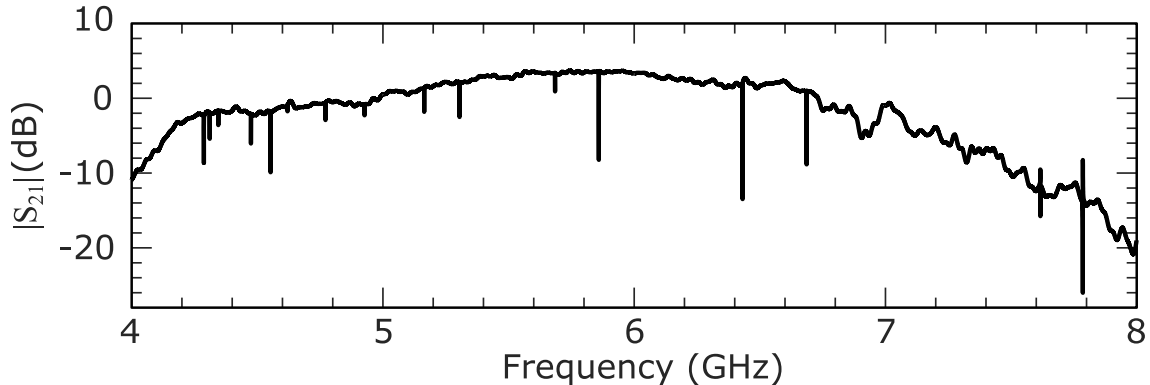


Figure 39: Measured ring resonator spectrum.

4.287 GHz, below which we observe no modes. We can observe 16 ring resonator modes between 4 and 8 GHz. For a left-handed 24-cell ring resonator with parasitic reactances, we expect 24 modes, with an infrared cutoff mode, an ultraviolet cutoff mode, then 11 pairs of degenerate energy modes, meaning a total of 13 resolvable modes should appear in the spectrum in an ideal case. Because we observe 16 modes within this small frequency span, it is clear that the degeneracy between mode pairs has been lifted in the circuit. The bulk of the degeneracy lifting may be attributed to the presence of grounding wirebonds that are unevenly distributed across the ring resonator. Aluminum wirebonds with a 1.25-mil diameter were used to aid in tying the voltage potential of the center disk of the ring resonator to the rest of the ground plane on the chip. These bonds contribute parasitic reactances asymmetrically across the ring, which result in a large lifting of the degeneracy of the modes. There are 11 wirebonds connecting the inner disk within the ring resonator to the ground plane, with lengths of approximately 1.5 mm. The inductive contribution of each wirebond is approximately 1 nH/mm [93]. Thus, we estimate the inductive contribution for each wire bond, L_W , to be approximately 1.5 nH. Figure 40 shows the location of the wirebonds and an effective circuit model that accounts for the parasitic reactances due to the wirebonds [94]. By design, the IR-cutoff frequency of the ring resonator is 4.8 GHz. Due to the parasitic stray reactances of the ring resonator lumped elements and the grounding wirebonds, the measured infrared cutoff frequency is lowered to 4.28 GHz.

Figure 41 shows the effect of the aluminum wirebonds on the ring resonator spectrum. The bonds are not spaced symmetrically due to the adjacent locations of the

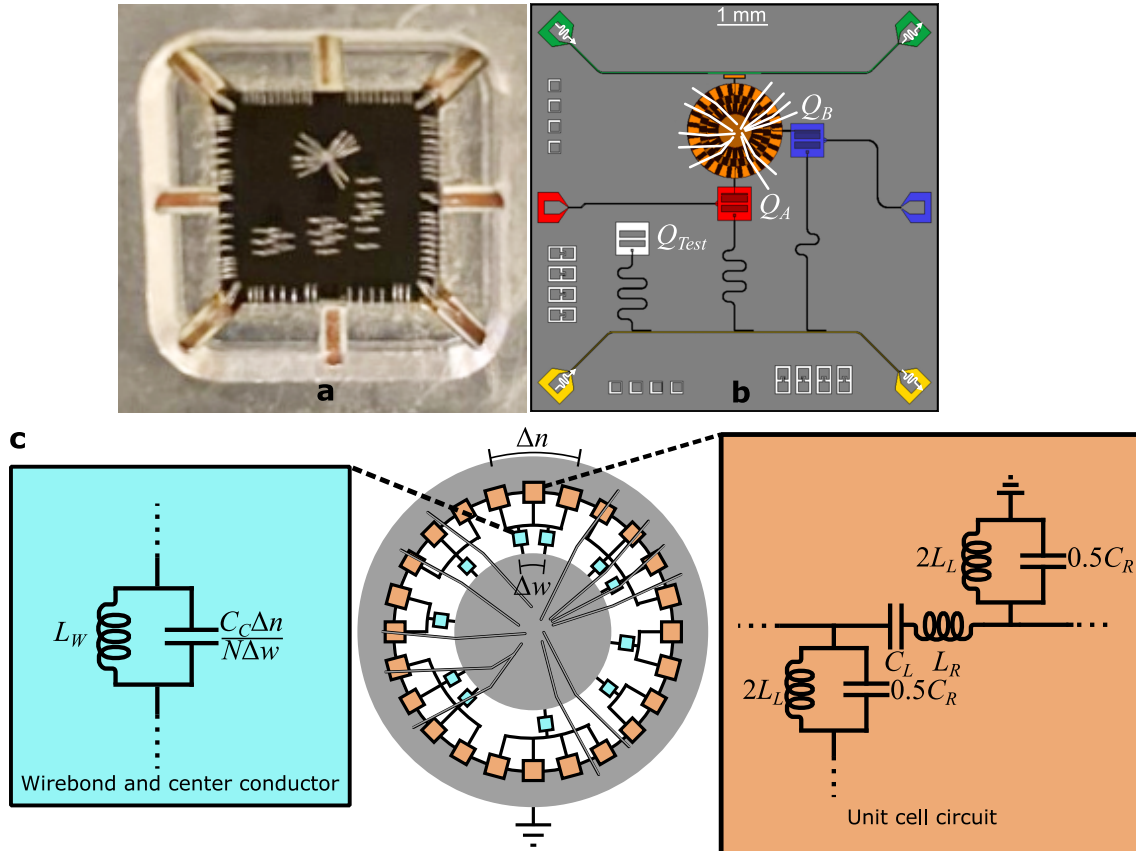


Figure 40: (a) Image of wirebonds used for grounding the device, as well as attachments to signal traces. (b) GDS of device layout including approximate wirebond positions shown with white lines. (c) Theoretical circuit model accounting for aluminum wirebonds.

qubits and feedline, and as such, these wirebonds break the symmetry of the clockwise and counterclockwise propagating waves and lift the degeneracy of the even and odd ring-resonator modes. The size of the degeneracy lifting ranges from ~ 30 MHz near the IR mode to ~ 250 MHz at higher frequencies and is in good agreement with theoretical simulations including a model for the wirebonds, as shown in Fig. 41 in blue. The same simulation without wirebonds fails to reproduce the observed lifting of degeneracies.

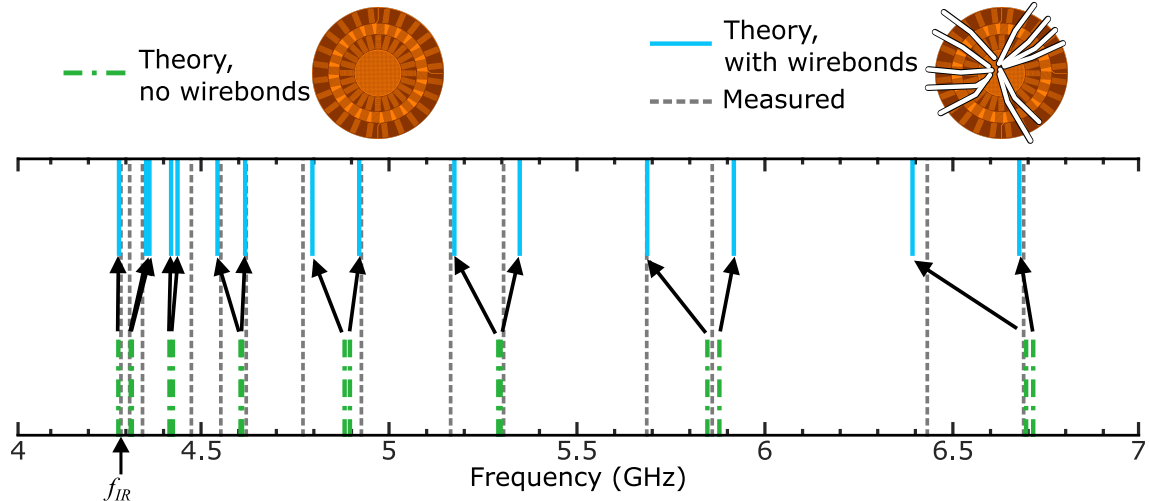


Figure 41: Measured ring resonator mode frequencies are shown with gray dashed lines. Theoretical mode frequencies are shown with green dashed-dotted lines when stray inductance due to wirebonds is not included and any degeneracy lifting is due to the qubits or feedline. Solid blue lines show large degeneracy lifting effect of wirebonds on the ring resonator mode frequencies.

7.2 Measurement of g -coupling

To characterize the coupling strength between each qubit and the different ring resonator modes, we probe the modes by measuring the microwave transmission through the ring resonator feedline, R_{in}/R_{out} , while scanning the flux for one of the qubits. The other qubit is flux-biased at its upper flux-insensitive sweetspot. We perform these measurements for each of the thirteen modes between 4-6.5 GHz. As we introduced in Ch. 3, when there is a coupling between a qubit and a mode, the qubit hybridizes with the ring-resonator mode, resulting in a vacuum Rabi splitting, which appears as an avoided level crossing in the spectrum of either the qubit or the mode. A selection of these measurements for Q_A and Q_B is shown in Fig. 42[a-f]. From these measurements, we can observe that the splittings are larger than the linewidths of the modes, indicating that we are operating in the strong coupling regime [96].

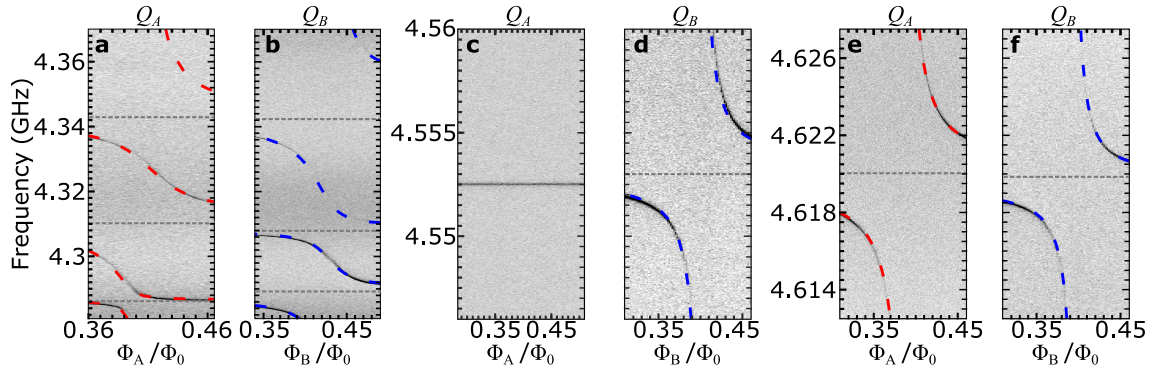


Figure 42: Vacuum Rabi splittings measured via R_{in}/R_{out} , between three ring resonator modes and (a) Q_A , (b) Q_B . Dashed lines in red (blue) show fits to splitting data for Q_A (Q_B) obtained from reduced Hamiltonian including one qubit and the three modes. Horizontal dotted lines show dressed mode frequencies. (c-f) Splittings and reduced Hamiltonian fits for two single modes for each qubit. For all measurements, the spectator qubit is fixed at its upper flux insensitive sweet spot ($\Phi_q/\Phi_0 = 0$). As shown in (c), Q_A has effectively zero coupling to the ring resonator mode at 4.553 GHz, while (d) shows Q_B has a coupling strength of 26.6 MHz.

7.3 Extraction of g -coupling from spectroscopy

To extract the magnitude of g_i^A and g_i^B for our two qubits, Q_A and Q_B , we perform a least-squares minimization to fit each set of splitting data to a reduced Hamiltonian for the ring-resonator mode-qubit system, shown as dashed lines in Fig. 42. In regions where the mode spacing and coupling are comparable, we simultaneously fit multiple modes to extract each g_i^A and g_i^B , as shown in Fig. 42(a,b). To elucidate the need for fitting the modes simultaneously, we highlight that the mode spacing between the infrared cutoff mode and the nearest frequency mode, at 4.287 GHz and 4.311 GHz, respectively, is 24 MHz, while the coupling strength of Q_A and Q_B to the IR-cutoff mode is $g_i^A/2\pi = 13$ MHz and $g_i^B/2\pi = 36.5$ MHz. Even more strikingly, the coupling strength of Q_A and Q_B to the mode at 4.311 GHz is $g_i^A/2\pi = 60$ MHz and $g_i^B/2\pi = 27$ MHz! In this region, we are operating in a super-strong coupling regime [29] in which a hybridized state is formed between the qubits and multiple ring resonator modes, making it impossible to treat the modes as separate oscillators.

In our g -coupling fits, we modeled each mode as an independent harmonic oscillator coupled capacitively to Q_A and Q_B , respectively. Using standard circuit quantization, we developed a reduced Hamiltonian for the circuit in the basis of transmon charge and resonator excitation number, given by

$$\begin{aligned} \hat{H}_{g,red}^q = & \left[\sum_n \left(4E_C^q (n - n_g)^2 |n\rangle\langle n| - \frac{E_J^q(\Phi_{ext}^q)}{2} (|n+1\rangle\langle n| + |n\rangle\langle n+1|) \right) \right] \otimes \hat{\mathbb{I}}_m \\ & + \sum_i \left[\sum_{m_i} \hat{\mathbb{I}}_n \otimes \hbar\omega_i \left(|m_i\rangle\langle m_i| + \frac{1}{2} \right) \right. \\ & \left. + \sum_{n,m_i} \hbar|g_i^q|n|n\rangle\langle n| \otimes \sqrt{m_i+1} (|m_i+1\rangle\langle m_i| + |m_i\rangle\langle m_i+1|) \otimes \hat{\mathbb{I}}_{m_i \neq j} \right] \end{aligned} \quad (7.99)$$

where q is either A or B for Q_A and Q_B , respectively. The variable E_C^q is the transmon charging energy and n_g is the transmon polarization charge; both parameters are defined in Sec. 3.1. The operator $\hat{\mathbb{I}}_m$ is the product of the mode identity operators, $\hat{\mathbb{I}}_{m_i}$ is the i th metamaterial mode identity operator, and $\hat{\mathbb{I}}_n$ is the qubit charge basis identity operator.

A numerical minimization is implemented to fit the relevant eigenvalues of the Hamiltonian to the vacuum Rabi splitting data. We truncate the Hilbert space to include 8 charge states for the qubit, n , and 4 number states, m , for the resonant modes in the Hamiltonian. For groups of modes with large g -coupling with respect to mode spacing, we include as many as three modes simultaneously in the fit. We do not explicitly include the energy contributions of the spectator qubit in the fits, but we do account for the dispersive χ shift of the ring-resonator modes due to the spectator qubit, which we have fixed at $\Phi_{ext}^q = 0$ so that it has a large detuning to these particular modes. The free parameters in the fits are the g_i^q values and $E_{J_0}^q$. We vary $E_{J_0}^q$ because the qubit maximum transition frequency is near the qubit readout cavity frequencies and cannot be observed directly, as explained in Sec. 6.2. All other parameters are determined via independent measurements and modeling.

We construct the variance-covariance matrix by taking numerical derivatives of the Hamiltonian with respect to the fit parameters. We compute 95% confidence intervals to obtain the uncertainties in our fit parameters.

7.4 Theoretical g -coupling

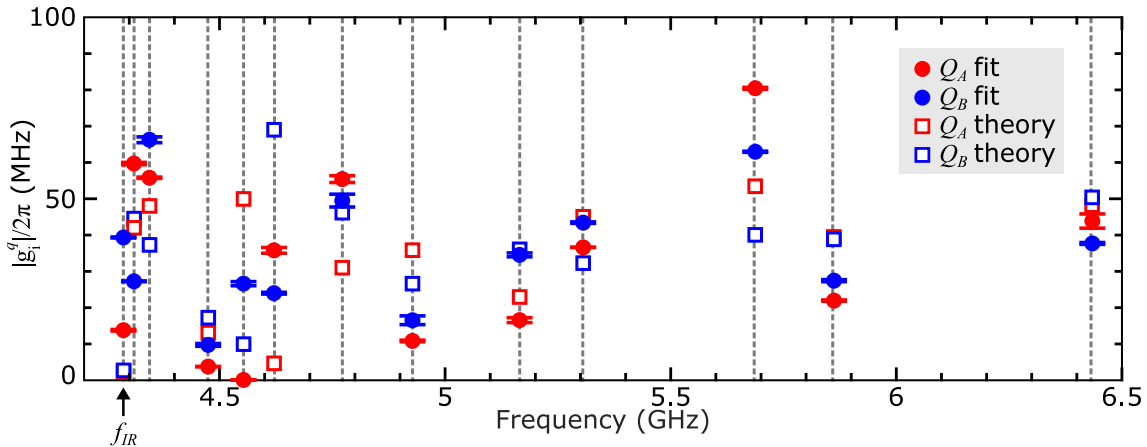


Figure 43: Extracted and theoretical $|g_i^g|/2\pi$ values for each ring-resonator mode i . Error bars on experimental data computed from 95% confidence intervals in g -coupling fits. Vertical dashed lines show bare ring resonator mode frequencies.

In Sec. 5.2, we introduced Eqs. (5.96) and Eqs. (5.97) that showed that the coupling strength of the qubits to the ring resonator modes is an oscillatory function that scales with mode frequency. These equations that define the even- and odd-parity coupling strength have roots which predict that there are multiple modes to which the qubits should not couple based on the geometry. However, there was only a single mode to which a qubit had a g -coupling of zero. For Q_A , one ring-resonator mode near 4.55 GHz has effectively zero coupling, while for Q_B , the extracted magnitude of $g_i^B/2\pi$ is 26.6 MHz to the same mode. Even more surprising, is that while theory predicts zero-coupling can occur, this particular mode is not a root. In the simple model without the feedline and wirebonds, this mode has a nonzero coupling strength to Q_A ; only in the more complex model in which we account for the symmetry breaking contribution of the wirebonds does this mode result in a negligible coupling strength. To accurately predict g -coupling strength, the theoretical calculations must include a model of the feedline and the wirebonds.

A collection of all of the experimental and theoretical values for $g_i^A(g_i^B)$ for $Q_A(Q_B)$ and ring-resonator modes from 4 GHz to 6.5 GHz are shown in Fig. 43. We observe a broad array of coupling magnitudes ranging from 0-80 MHz. While the theoretical

Qubit-ring resonator mode g -coupling values		
Bare frequency (GHz)	$ g_i^A /2\pi$ (MHz)	$ g_i^B /2\pi$ (MHz)
4.2874	13.7	39.3
4.3108	59.7	27.2
4.3449	55.8	66.3
4.4749	3.68	9.68
4.5531	0.0	26.6
4.6206	35.8	24.0
4.7717	55.4	49.5
4.9271	10.8	16.5
5.1642	16.5	34.5
5.3049	36.6	43.4
5.6856	80.5	63.0
5.8599	21.9	27.4
6.4317	43.9	37.3

Table 3: Magnitude of qubit-ring resonator g -coupling parameters for Q_A and Q_B .

model captures the general behavior of $g_i^{A/B}$, a more complete model of the symmetry-breaking perturbations of the ring-resonator circuit is required for better quantitative agreement.

Looking forward to the next set of measurements in which we explore inter-qubit interactions, we note that we cannot directly measure the sign of g by observing the vacuum-Rabi splitting data. Table 3 shows the bare ring resonator mode frequencies and lists the magnitude of g_i^A and g_i^B for each mode. As we will discuss in Ch. 8, the magnitude and parity of the pairs of g_i^A and g_i^B for Q_A and Q_B to each mode i impacts the qubit-qubit interactions that are mediated by the ring resonator. We utilize these extracted g -couplings for each of the modes in the subsequent sections for analyzing our measured qubit-qubit interactions, and ultimately determine the parity of the coupling using a combined theoretical and experimental approach. Details on how the parity of g is determined are given in Ch. 8.

Chapter 8

J-coupling between qubits

Multi-qubit operations have been performed in the field of cQED through various approaches, including direct coupling, tunable coupling, and coupling through a shared cavity. Direct interactions have been realized on a variety of platforms, including capacitively coupling charge qubits and inductively coupling flux qubits [63, 64]. A quantum bus, generally realized using a cavity resonator, can also be used in quantum circuits to entangle distant qubits [69]. In the case of the metamaterial ring resonator, it is comprised of a series of lumped-element capacitors shunted to ground by two inductors and has two distant transmon qubits coupled around the ring. This makes the ring resonator a unique platform that provides direct coupling of two physically distant qubits via lumped element circuitry. In the case of the metamaterial ring resonator, it is a unique quantum bus comprised of multiple modes to which the qubits couple.

In this chapter, we discuss the measurements of the *J*-coupling between the qubits mediated by the ring resonator modes and compare these results with a theoretical model. We introduced the perturbative Schrieffer-Wolff approximation for the *J*-coupling between two qubits coupled to a single resonator in Eq. 3.52. For the multi-mode ring resonator, we must define the exchange coupling as a sum over all of the ring resonator modes, given by

$$J = \frac{1}{2} \sum_{i=1}^N g_i^A g_i^B \left(\frac{1}{\Delta_i^A} + \frac{1}{\Delta_i^B} \right), \quad (8.100)$$

where $\Delta_i^A(\Delta_i^B)$ give the detuning for $Q_A(Q_B)$ to each ring resonator mode i , and $\Delta_i^q = \omega_q - \omega_i$ is the difference between the qubit frequency and the i^{th} mode frequency

for $q = A(B)$, and can be positive or negative depending on where the qubit is positioned in frequency. As Eq. (8.100) shows, the strength of the exchange coupling depends on the parity and strength of the g_i^A and g_i^B , as well as the detuning of Q_A and Q_B to each of the modes. We have shown in Ch. 7 the extracted coupling strength of each qubit to each mode, and using these values and some modeling, we can predict the magnitude and sign of the exchange coupling accurately.

8.1 Measurement of J

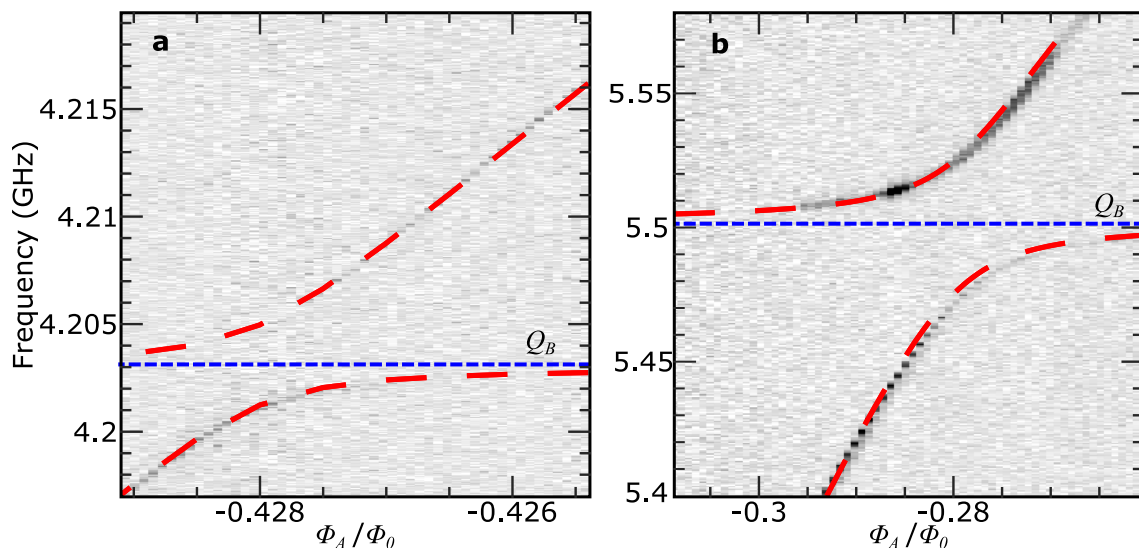


Figure 44: J -coupling spectroscopy data as a function of flux on Q_A . Red dashed lines show fits to splitting data from effective Hamiltonian. The blue dashed line shows the fixed frequency of Q_B . (a) Avoided level crossing between Q_A and Q_B at 4.2 GHz. (b) Avoided level crossing between Q_A and Q_B at 5.5 GHz.

We can measure the transverse exchange coupling between the qubits mediated by virtual photon exchange with the various ring-resonator modes by fixing the transition frequency of one qubit, say Q_B , then using the local flux-biasing capability to vary the frequency of the other qubit (Q_A), while performing spectroscopy on Q_A . A nonzero J -coupling between the qubits results in an anti-crossing in the spectrum when the bare qubit frequencies cross. We can adjust the frequency of the crossing point for the bare qubit frequencies relative to the ring-resonator modes and study the variation of the exchange coupling between the qubits as a function of frequency.

Two such measurements are shown in Fig. 44. We fix the frequency of Q_B at 4.203 GHz, then flux-bias Q_A so that its bare transition frequency crosses the fixed frequency of Q_B . We observe a small anti-crossing of the qubit energies in Fig. 44(a). The IR-cutoff for the ring resonator is at 4.28 GHz, so although the qubits are outside of the range of frequencies of the modes, the lowest frequency modes have sufficiently large couplings to result in an exchange interaction between the qubits when they are 80 MHz detuned from the first ring resonator mode. We can extract the exchange coupling by solving the Hamiltonian for the ring resonator, two-qubit system. The red dashed lines in Fig. 44(a,b) show the fit to the data, from which we determine that the J -coupling is 2.1 MHz in Fig. 44(a). Discussion of the Hamiltonian fits can be found in Sec. 8.2. In Fig. 44(b), Q_B is fixed at 5.5 GHz, well within the range of ring resonator modes, and Q_A is flux-biased so that its bare transition frequency crosses that of Q_B . The J -coupling for this frequency is 27 MHz, more than an order of magnitude larger than in Fig. 44(a).

8.2 Extraction of J -coupling from spectroscopy

The J -coupling fits were achieved by performing a least squares minimization of the spectroscopy data using an effective Hamiltonian

$$H_{J,eff}/\hbar = \frac{\tilde{\omega}_A}{2}\sigma_A^z + \frac{\tilde{\omega}_B}{2}\sigma_B^z + J(\sigma_A^-\sigma_B^+ + \sigma_B^-\sigma_A^+) + \sum_i \omega_r^i a_i^\dagger a_i, \quad (8.101)$$

which reduces the qubits to two-state systems. The summation over modes, i , is reduced to include only the two nearest modes to the crossing of the bare frequencies of Q_A and Q_B . The dressed qubit frequency for Q_A is given by $\tilde{\omega}_A = \omega_A + \sum_i \chi_i^A$. To measure J , the flux bias applied to the SQUID loop of Q_B is fixed while we tune the transition frequency of Q_A , so we assume $\tilde{\omega}_B$ is a fixed value. We obtain $\tilde{\omega}_B$ from independent measurements in which we detune Q_A and perform spectroscopy on Q_B . The transition frequency from the ground to the first excited state of Q_A is given by $\omega_A = \left(\sqrt{8E_J^A E_C^A} - E_C^A\right)/\hbar$. The amplitude of the exchange term for the two qubits, J , and the maximum Josephson energy for Q_A , E_{J0}^A , are the free parameters in the fit. The method for obtaining the magnitudes of the g_i^A and g_i^B couplings is outlined in Sec. 7.4. All other parameters are determined via independent measurements. We

use the same method described in Sec. 7.4 in which we obtain numerical derivatives to compute 95% confidence intervals in our fit parameters.

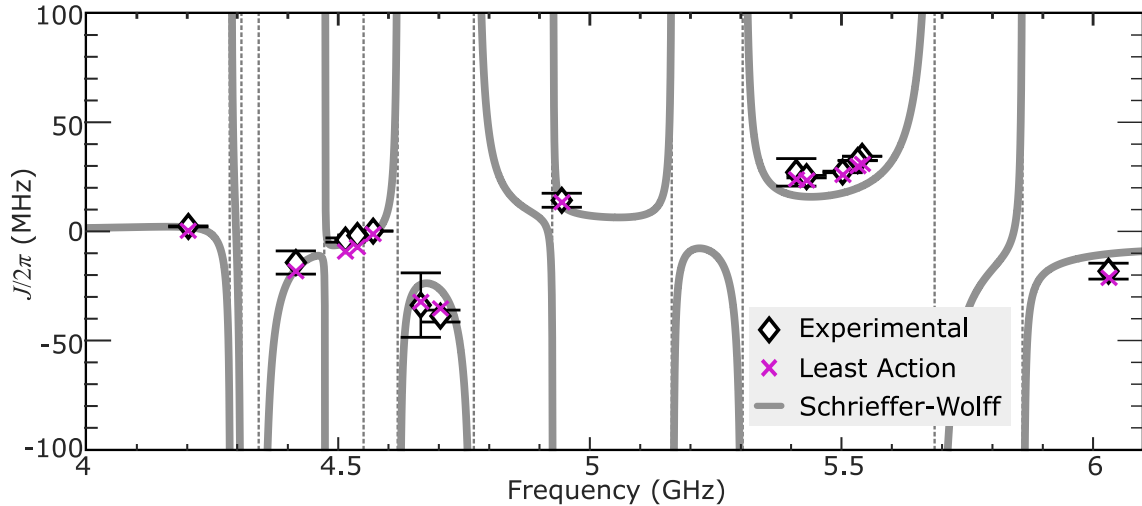


Figure 45: Experimental and theoretical J -coupling values as a function of frequency. Diamonds show experimental values for $J/2\pi$, with error bars computed from 95% confidence intervals in fits. Gray lines and purple crosses show theoretical $J/2\pi$ values calculated using Schrieffer-Wolff and Least Action, respectively. Dotted vertical lines show bare ring-resonator mode frequencies.

Figure 45 shows a selection of extracted J -coupling values compared to theoretical predictions for J for a range of qubit frequencies. Gray lines show the perturbative Schrieffer-Wolff approximation for J , described by Eq. (8.100). The perturbative approximation is an effective predictor of J -coupling when interaction strengths are moderate and at frequencies that are somewhat detuned from the modes. From Fig. 45, we see that in cases where the qubit and resonator frequencies are close, the perturbative model diverges. As such, we also include a non-perturbative Least Action method [78, 74, 97] calculation of the J -coupling at selected frequencies.

8.3 Non-perturbative J calculations

Our collaborators performed a non-perturbative calculation of J by block-diagonalizing our full-system Hamiltonian. The Hamiltonian includes single and double excitations for both qubits and resonator modes, as well as all possible combinations of one qubit

Qubit-ring resonator mode g -coupling values and parity			
Bare mode frequency (GHz)	$ g_i^A /2\pi$ (MHz)	$ g_i^B /2\pi$ (MHz)	Parity
4.2874	13.7	39.3	Even
4.3108	59.7	27.2	Even
4.3449	55.8	66.3	Odd
4.4749	3.68	9.68	Even
4.5531	0.0	26.6	Even
4.6206	35.8	24.0	Odd
4.7717	55.4	49.5	Even
4.9271	10.8	16.5	Even
5.1642	16.5	34.5	Odd
5.3049	36.6	43.4	Even
5.6856	80.5	63.0	Odd
5.8599	21.9	27.4	Odd
6.4317	43.9	37.3	Even

Table 4: Magnitude of qubit-ring resonator g -coupling parameters and parity for Q_A and Q_B . Here, the parity of the g -coupling values between the two qubits is determined by comparing measured versus perturbative theoretical calculations of the exchange coupling for Q_A and Q_B , as described in the main text.

excitation paired with one resonator excitation. Also included are two excitations of ring resonator modes which are not the same mode. The Hamiltonian also includes simultaneous excitation of two different ring resonator modes. The system is restricted by only allowing strongly coupled transitions in the frequency domain we are interested in. The resultant Hamiltonian is then block-diagonalized using the Least Action method, and the resulting J_{00} coupling strength can be extracted. This gives two J values for each anti-crossing between the two qubits. One is slightly before the discontinuity of the dressed frequencies and the other one is slightly after it. These two values are usually very close to each other and we average them to get one value for the anti-crossing. This is then compared to the calculated J -coupling obtained via Schrieffer Wolff and experimentally measured values.

8.4 Predicting the sign of J

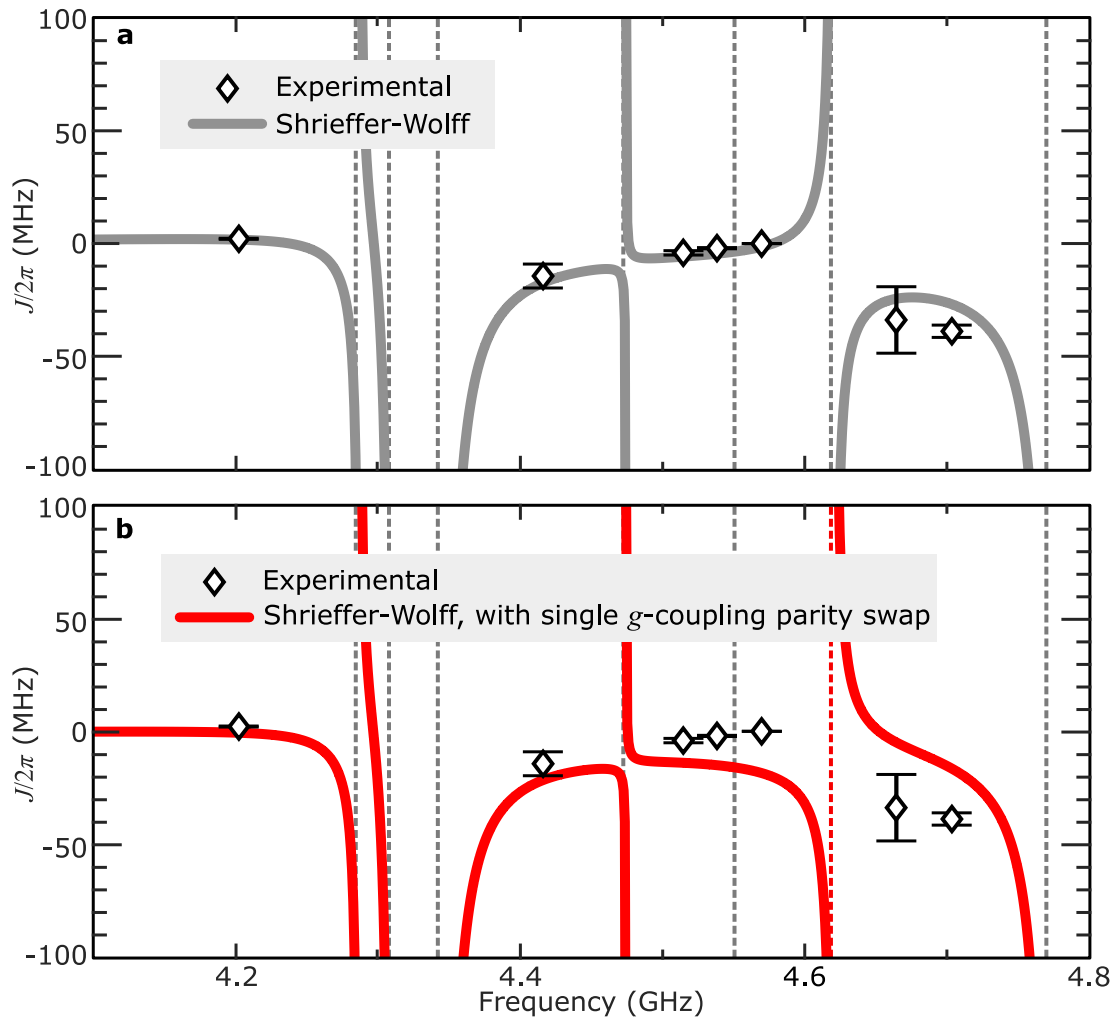


Figure 46: Comparison of experimental and theoretical J -coupling values as a function of frequency when g -coupling parity for Q_A and Q_B is changed for a single mode. Diamonds show experimental values for $J/2\pi$, with error bars computed from 95% confidence intervals in fits. Dotted grey vertical lines show bare ring-resonator mode frequencies. (a) Gray lines show theoretical $J/2\pi$ values calculated using Schrieffer-Wolff. (b) Red dotted line denotes ring resonator mode that has swapped parity of the g -coupling for Q_A and Q_B . Red lines show the theoretical $J/2\pi$ values calculated using Schrieffer-Wolff when the g -coupling is swapped for this single ring resonator mode.

Although our spectroscopy measurements only provide the magnitude of J , using the perturbative theoretical calculations with different possible parities of g_i^A and g_i^B for each mode i , we determine the sign of each qubit-mode coupling that provides the best agreement with the exchange coupling measurements. Table 4 shows the magnitude and parity of the g -couplings measured for this device. Recall, we have an expression for the g -coupling between the qubits and ring resonator modes for even and odd propagating waves, as shown in Eq. (5.96) and Eq. (5.97). From this, we can predict the parity of the coupling strength for the pairs of modes for an ideal circuit. However, this expression excludes parasitic reactances in the circuit from the lumped-element components and the wirebonds, and also ignores imperfect grounding of the center disk. The predictions for the parity are not reliable for small magnitude g -couplings in the real device. These symmetry-breaking effects can cause shifts in g , either positive or negative, and for roots of Eq. (5.96) and Eq. (5.97) in the ideal circuit, this can mean changing the parity by pushing the g to a positive or negative non-zero value in the actual device. This effect is only relevant for the smallest g values, since the asymmetric contributions are not strong enough to shift the g for larger values significantly enough to change the parity. Figure 46 compares experimental and perturbative J -coupling values, with Fig. 46(a) using the parity assumptions we show in Tab. 4 in the perturbative calculation, and Fig. 46(b) changing the parity on the g -coupling for the ring resonator mode at 4.6206 GHz from odd to even. This results in a mismatch between the experimental $J/2\pi$ values and the theoretical values near the mode.

From the experimentally measured J values and the agreement with the theoretical model, it is clear that the exchange coupling can be tuned over a broad range for this system. The extracted magnitudes of J in the frequency range shown in Fig. 45 range from zero and 41 MHz, and the sign of J also varies depending on the detuning between the qubits and the various ring-resonator modes and the parity.

The exchange coupling is an entangling interaction between the two qubits that can be used for implementing a two-qubit gate when there is a mechanism for J to be turned on and off. While we can control J by detuning one qubit from the other, the impact of higher order effects is an important consideration when determining a scheme for implementing a two-qubit gate. Next, we will look at higher order entangling interactions for this ring resonator, qubit device.

Chapter 9

ZZ Interaction between qubits

When two or more qubits are coupled via a coupling element, *ZZ* interactions generally arise between the qubits, where the state of one qubit can shift the transition frequency of the other interacting qubit. In Ch. 3, we described Eq. (3.53) that defines the *ZZ* interaction in terms of the transition energies for the two-qubit system. Such interactions can be problematic in multi-qubit systems and can generate unwanted and uncontrolled entanglement [73, 74].

On the other hand, the *ZZ* coupling can also be used for implementing two-qubit entangling gates, provided the interaction strength can be modulated [98, 99, 100, 101]. In the dense multi-mode spectrum of our metamaterial ring resonator system, we explore the *ZZ* interaction between the two qubits for multiple qubit detunings within different regions of the mode spectrum. We show that the *ZZ* interaction can be modulated over a large range for our system with only small frequency shifts of one of the two qubits.

9.1 Measurement of the *ZZ* interaction

We use the standard Ramsey interferometry technique introduced in Ch. 3, to extract the *ZZ* interaction strength. First, we bias Q_B to a particular transition frequency, then we adjust the bias of Q_A to various frequencies relative to Q_B and the mode spectrum. At each bias point for Q_A , we perform a standard Ramsey fringe sequence while stepping through the drive frequency for the $X/2$ pulses for Q_A , allowing us to identify the transition frequency for Q_A . We then perform a second Ramsey fringe

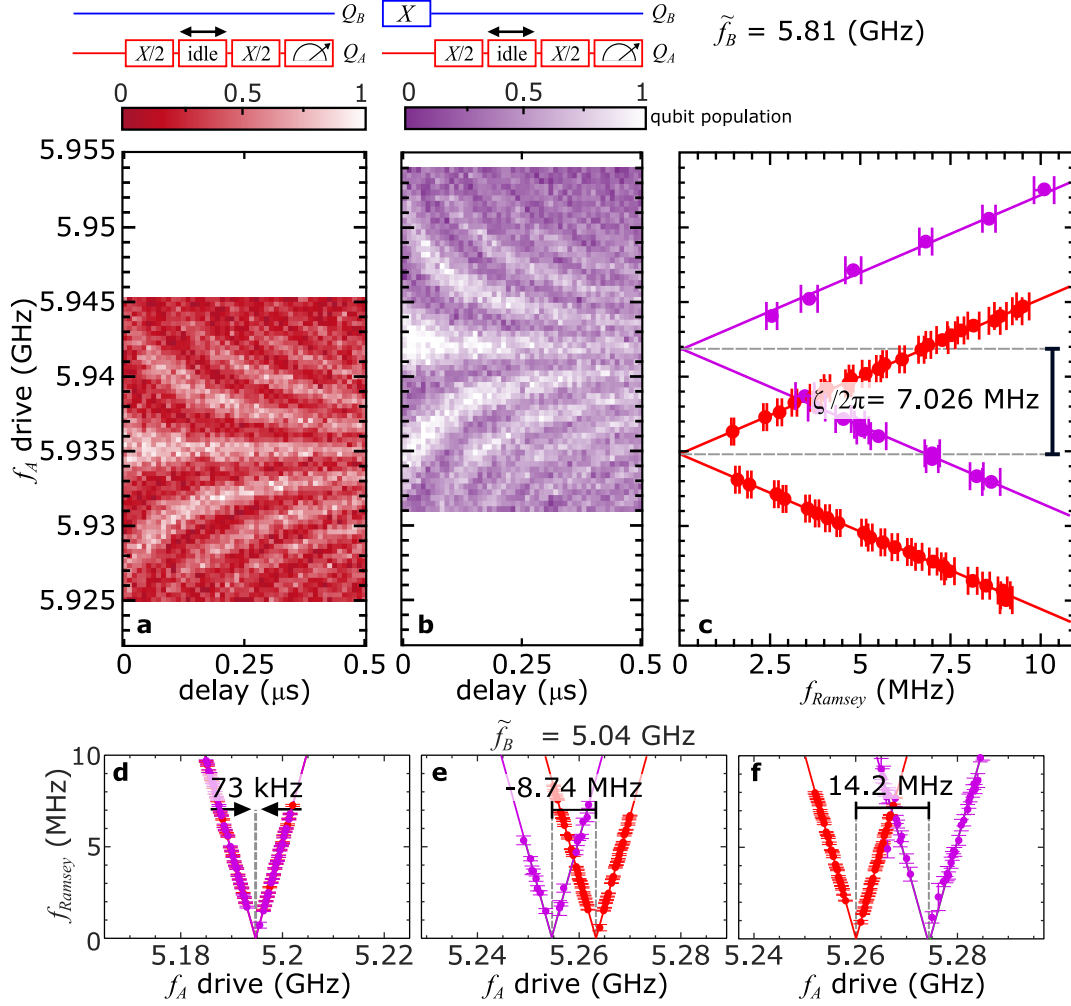


Figure 47: Measurement sequence for obtaining ZZ interaction strength. (a) A Ramsey pulse sequence is performed on Q_A at variable drive frequencies while Q_B is idle. (b) A second Ramsey fringe measurement is performed on Q_A after a π -pulse is applied to Q_B . (c) Horizontal slices of Ramsey fringe measurements are fit to obtain the Ramsey oscillation frequency, f_{Ramsey} , at each drive frequency. The ZZ interaction, denoted $\zeta/2\pi$, is the change in the dressed transition frequency for Q_A , \tilde{f}_A , depending on whether Q_B is in the ground or excited state. (d-f) Three example plots of Ramsey frequency as a function of Q_A drive frequency (f_A drive) for different Q_A bias points with linear fit lines for ZZ measurements taken when Q_B is at 5.04 GHz.

measurement of Q_A , but now with each Ramsey sequence preceded by an X pulse on Q_B . The difference in the transition frequency for Q_A between the two Ramsey fringe sequences corresponds to the strength of the ZZ interaction, ζ .

9.2 Extraction of ZZ

The pulse sequences for extracting the ZZ interaction strength are shown in Fig. 47. The Ramsey fringe fits are performed by taking single horizontal slices of the data shown in Fig. 47(a,b). We then apply damped, oscillatory fit function

$$F(t) = \frac{1}{2} [1 + \cos(2\pi f_{\text{Ramsey}} t) e^{-t/T_2^*}]$$

to the normalized data, with f_{Ramsey} and T_2^* as free parameters in the fit. We remove fits with error greater than 0.4 MHz in the estimation of f_{Ramsey} . We then fit a line through the f_{Ramsey} vs f_A drive data with a slope of one to find the zero point for the Ramsey oscillation frequencies, as shown in Fig. 47[c-f]. We perform these fits for the two pulse sequences with and without the π pulse on Q_B , then calculate the difference in transition frequency for Q_A to extract $\zeta/2\pi$. The error for extracting the f_{Ramsey} values is computed from 95% confidence intervals for the Ramsey fits. The error bars for the $\zeta/2\pi$ values as a function of \tilde{f}_A in Fig. 48 are obtained by finding the 95% confidence intervals for a linear fit with a slope of one to the f_{Ramsey} data.

When performing the ZZ measurements, we fix the bare frequency of Q_B and vary the frequency of Q_A , but the dressed frequency of Q_B varies depending on the frequency of Q_A . To measure the frequency of Q_B with high precision, a Ramsey fringe measurement and fit is performed for Q_B for each frequency tuning of Q_A . The range in \tilde{f}_B is 0.7 MHz (1 MHz) for the measurements in which we quote \tilde{f}_B to be 5.04 GHz (5.81 GHz). These small variations in \tilde{f}_B are due to the effective inter-qubit coupling via the ring resonator modes. In Fig. 48(a,b) we show two series of ZZ measurements as a function of the dressed transition frequency for Q_A for two different bias points of Q_B . We observe that ζ can vary over a wide frequency range, covering both positive and negative values and crossing through zero, both smoothly in some regions and discontinuously in others.

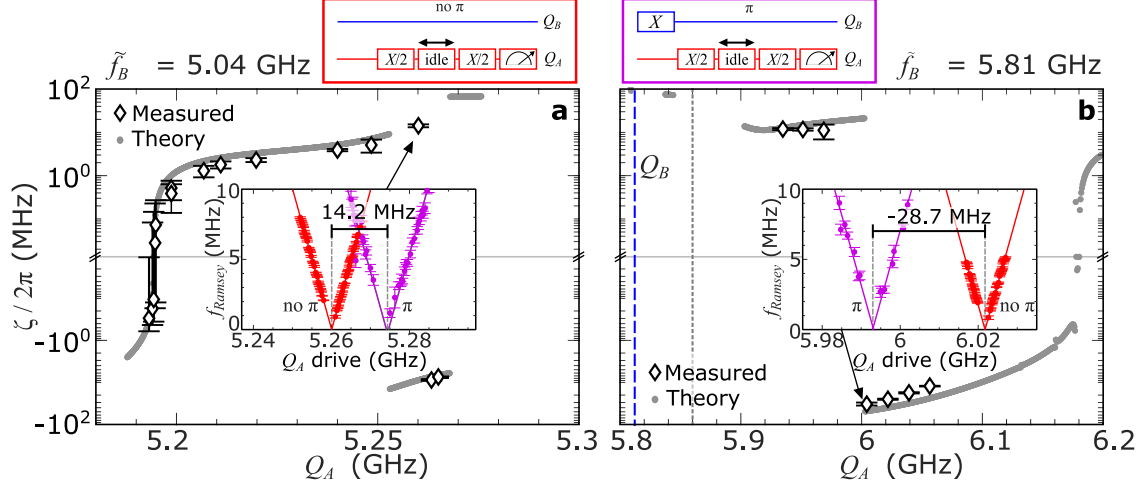


Figure 48: $\zeta/2\pi$ as a function of the dressed frequency of Q_A , \tilde{f}_A , when the dressed frequency of Q_B , \tilde{f}_B , is (a) 5.04 GHz, (b) 5.81 GHz. Measured and theoretical values are shown as diamonds and gray lines, respectively. Vertical dashed lines in blue and gray show the location of Q_B and the ring resonator modes in frequency space, respectively. Insets show Ramsey oscillation frequency fit data as a function of Q_A drive frequency taken from Ramsey fringe measurements. Red data points and fit lines generated by performing a simple Ramsey pulse sequence (shown in red box) on Q_A at multiple detunings and extracting oscillation frequency. Data resulting from pulse sequence in which a π -pulse is applied to Q_B , followed by a Ramsey on Q_A (shown in purple box). Error bars computed from 95% confidence intervals for both Ramsey oscillation fits. Intersection of fit lines where Ramsey oscillation frequency vanishes indicate Q_A frequency, from which we compute $\zeta/2\pi$.

9.3 Theoretical ZZ calculations

We will outline the theoretical ZZ calculations performed by our collaborators. The theoretical curves are calculated by either fully diagonalizing the Hamiltonian given in Eq. (5.98) in Ch. 3, or, using the block-diagonalized Hamiltonian used in the J -coupling fits, only diagonalizing the qubit subspace to save computational cost. After diagonalizing the Hamiltonian, the ZZ interaction strength is then calculated using $\zeta = E_{00} + E_{11} - E_{10} - E_{01}$. While the ZZ interaction only involves energy eigenvalues for when Q_A and Q_B are either in the ground or first excited state, higher non-computational photon states can cause shifts in these energy levels.

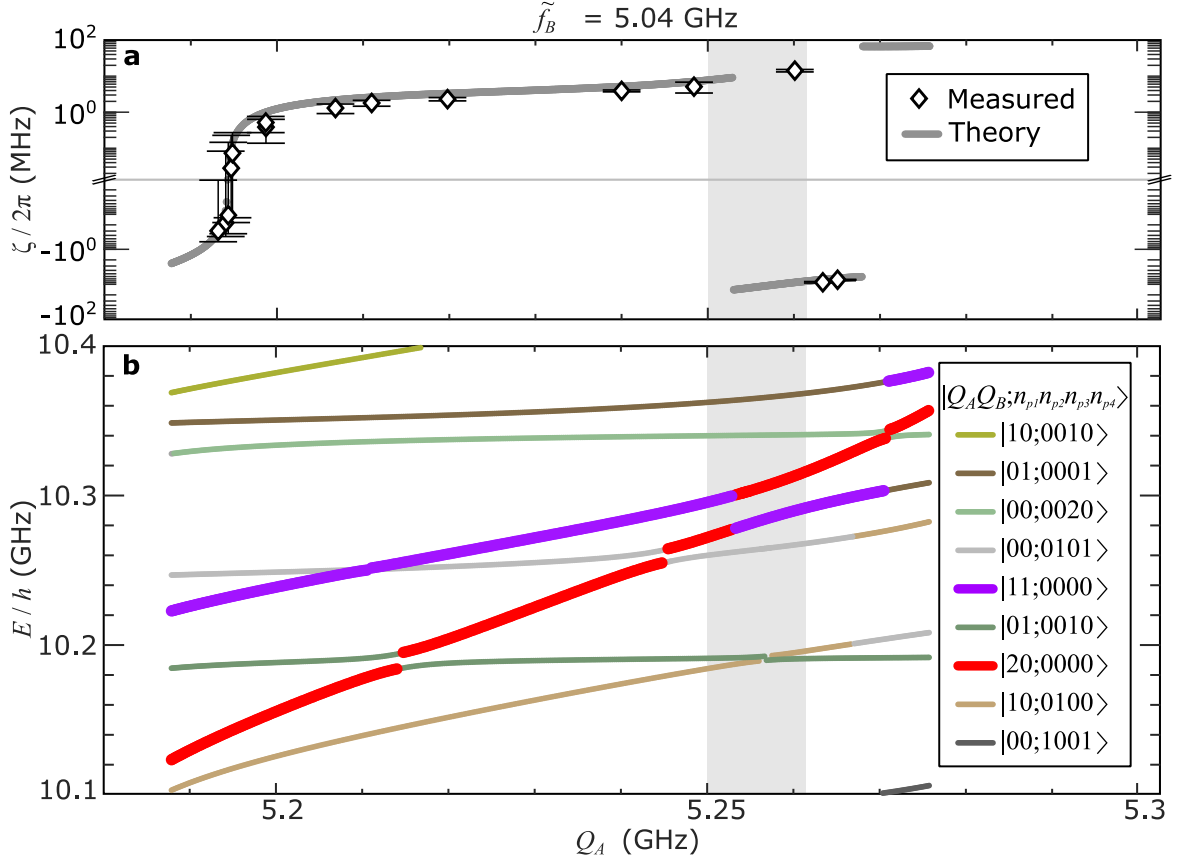


Figure 49: Uncertainty in theoretical ZZ values due to energy level anti-crossings. (a) Experimental and theoretical ZZ interaction $\zeta/2\pi$ as a function of \tilde{f}_A shown with diamonds and grey lines, respectively, with shading added to show region of uncertainty. (b) Multi-photon energies as a function of \tilde{f}_A . The light grey region denotes uncertainty in the theoretical ZZ calculation. The discontinuity of the ZZ interaction around 5.25 GHz is caused by an anti-crossing of the $|11\rangle$ and $|20\rangle$ states.

Figure 48(a) shows that there are discontinuities in $\zeta/2\pi$ for our device consisting of two qubits coupled to multiple modes. To better understand these discontinuities, we can compare the theoretical and measured $\zeta/2\pi$ data as a function of \tilde{f}_A to the theoretical energy spectrum. The dense ring resonator mode spectrum in the 4 – 6 GHz frequency range results in a dense population of two-photon energy states in the 10 GHz region of the energy spectrum. Figure 49(a) shows the same ZZ data from Fig. 48(a) with a grey region designating uncertainty in the theoretical values for $\zeta/2\pi$. Figure 49(b) shows the energy eigenvalues for two-photon states. The

state notation is of the form $|Q_A Q_B; n_{p1} n_{p2} n_{p3} n_{p4}\rangle$, where the first two digits define excitations in Q_A and Q_B , and the four digits after the semi-colon designate photons in the modes at frequencies 4.772 GHz, 4.927 GHz, 5.164 GHz, and 5.305 GHz. The biggest impact on the ZZ strength comes from the E_{11} level interacting with non-computational states. The most important states are $|20; 0000\rangle$ and $|01; 0001\rangle$, which both couple strongly to $|11; 0000\rangle$, since only one exchange of excitation is required for a transition. The anticrossing with $|20; 0000\rangle$ is especially interesting here, since it causes a large shift and discontinuity of E_{11} , which is also observable in the experimental data in Fig. 49(a). However, the experimental drop-off is positioned at 5.26 GHz, while the theoretical one is at 5.253 GHz. This small disagreement can be attributed to small inaccuracies in the model parameters. The anharmonicity of Q_A determines the energy of the $|20; 0000\rangle$ state; an inaccuracy here will result in a frequency shift of the drop-off position. There are also multiple ring resonator modes nearby, and a small variation in the mode frequencies or coupling strengths will impact the position of the discontinuity.

We observe excellent agreement between our experimental results and theoretical calculations of the variation in the ZZ interaction, capturing both the regions where ζ changes sign smoothly and where it jumps discontinuously. For our multimode ring resonator, a quite small change in the frequency of one qubit, of the order of a few MHz for Q_A in this case, results in a change in $\zeta/2\pi$ from zero to tens of MHz. This significant change is due to the large effective coupling between the two qubits, which is mediated by the high mode density. This large coupling causes a strong repulsion of the $|11\rangle$ and $|20\rangle$ states, leading to large changes in ζ .

Chapter 10

Future and ongoing work

We have shown that a left-handed metamaterial ring resonator used as a coupling bus for two transmon qubits has interesting properties with broad applications. In this work, we presented measurements and modeling of the interactions between the qubits and the ring resonator modes, as well as the inter-qubit entangling interactions mediated by the multimode system. We have shown that the system shows extreme versatility in coupling parameters due to the unique wave structure of the modes in the ring. In this section, we outline future and ongoing work related to this experiment.

10.1 Implementing a two-qubit gate with a ring resonator bus

As we discussed in Ch. 9, the ring resonator is a promising platform for implementing two-qubit gates due to the ZZ -interactions between qubits being tunable with high contrast over a small frequency range. Prior work on two-qubit gates based on in situ modulation of the ZZ interaction using tunable couplers has required tuning of at least one circuit element over a frequency range of the order of GHz [102, 103]. Fast tuning over such a large range introduces the risk of fidelity degradation through leakage to other modes, both intentional and spurious, within this frequency window. By contrast, the orders of magnitude smaller tuning range required for moving between the on and off regimes of the ZZ interaction for our multimode ring resonator provides a promising pathway for implementing a high-fidelity two-qubit entangling gate.

It is feasible to implement a ZZ -based gate, such as a CZ gate, using the device

measured in this work. As we show in Ch. 9, when the frequency of Q_B is fixed at 5.04 GHz, the ZZ -interaction can be varied from zero to tens of MHz when the frequency of Q_A is tuned over an order of tens of MHz. Additionally, a non- ZZ -based gate, such as a cross-resonance (CR) gate, could be implemented when the ZZ interaction is at or near zero if the device was redesigned with two separate feedlines for control and readout of the two qubits. To implement a CR gate, if two qubits have a J -coupling and are detuned in frequency from each other, driving one qubit, the control qubit, at the transition frequency of the other qubit, the target qubit, switches on the ZX interaction [77]. By tuning the qubits to frequencies at which the ZZ interaction goes to zero, the ZZ interaction would no longer contribute to infidelity when implementing a two-qubit gate like the CR gate or the \sqrt{i} SWAP gate. However, the coherence times of the qubits are Purcell-limited when the qubits are tuned above the IR-cutoff frequency of the ring resonator [37]. As such, future devices could be designed without external coupling of the ring resonator to a feedline to reduce Purcell losses to the ring resonator modes and thus improve qubit coherence.

10.2 Coupling in more qubits to the ring resonator bus

The majority of current superconducting qubit-based architectures allow for only nearest neighbor connectivity [22, 104]. There are examples of long-range connectivity for superconducting qubits, such as a right-handed ring resonator that has been proposed as an architecture for implementing non-nearest neighbor coupling between qubits [43]. This right-handed ring resonator was shown experimentally to support four all-to-all coupled qubits and theoretically could support twelve qubits, with each qubit coupled to nine other qubits. We have shown that the left-handed metamaterial ring resonator bus architecture can be used to couple two physically separated qubits, and we would like to investigate the connectivity of three or more qubits coupled via the ring resonator in future experiments. The inter-qubit coupling is mediated by the ring resonator modes, and because these left-handed metamaterial ring resonators have a dense spectrum in the frequency range of the qubit, it is not a significant consideration to position the qubits at an antinode of a particular mode of the resonator. The compact ring geometry allows for coupling multiple modes to more than two qubits, and we would like to experimentally investigate the variability of the ZZ

interaction between each pair of qubits with selective flux control of each qubit. Additionally, the left-handed metamaterial design has a smaller physical footprint than a right-handed ring resonator, particularly compared to the 3D waveguide design in Ref. [43].

Another proposed coupling scheme presented in Ref. [43] is a multi-ring architecture, where rings are connected via $\lambda/2$ transmission line segments with a characteristic impedance equal to half that of the right-handed ring resonators. It would be interesting to create a multi-ring architecture with left-handed metamaterial ring resonators connected together with two or more qubits coupled around each left-handed metamaterial ring resonator. Because of the more compact design and relative ease of fabrication, in the case of the left-handed metamaterial ring resonator, this long-range qubit coupling scheme could be an alternative way to scale the device to include more long-range qubit interactions.

10.3 Symmetry-breaking around the ring resonator

Wirebonds placed across the ring resonator break the symmetry of the device and lift the degeneracy between clockwise and counter-clockwise modes. We are interested in exploring the spectrum of the ring resonator and the qubit coupling when the symmetry of the circuit is preserved. To ensure uniform grounding, we plan to utilize a flip-chip design that uses indium pillars placed uniformly around the chip to create a unified ground plane connecting the two chips that comprise the flip-chip design. A novel focus could be observing qubit interactions on resonance with degenerate pairs of modes. The J -coupling depends on $1/\Delta$, where Δ is the detuning between the qubit and modes, so having pairs of degenerate modes changes the parameter space for the J -coupling and ZZ interaction, and we are interested in exploring this space. Engineering intentional asymmetry into the ring resonator circuit could allow for a spectrum with pairs of modes arbitrarily close together in frequency. This could be a path for generating multipartite entanglement between the qubit and a pair, or pairs, of these modes.

Bibliography

- [1] Philip Krantz, Morten Kjaergaard, Fei Yan, Terry P Orlando, Simon Gustavsson, and William D Oliver. A quantum engineer’s guide to superconducting qubits. *Applied physics reviews*, 6(2), 2019.
- [2] Haozhi Wang. *Fabrication and Characterization of Superconducting Metamaterial Resonators*. PhD thesis, Syracuse University, 2018.
- [3] Alan Mathison Turing et al. On computable numbers, with an application to the entscheidungsproblem. *J. of Math*, 58(345-363):5, 1936.
- [4] Gordon E Moore. Cramming more components onto integrated circuits. *Proceedings of the IEEE*, 86(1):82–85, 1998.
- [5] Michael A Nielsen and Isaac L Chuang. *Quantum computation and quantum information*. Cambridge university press, 2010.
- [6] Samuel K Moore. Intel’s stacked nanosheet transistors could be the next step in moore’s law. *IEEE Spectrum*, 2020.
- [7] John Preskill. Quantum computing in the nisq era and beyond. *Quantum*, 2:79, 2018.
- [8] John Preskill. The physics of quantum information. *arXiv preprint arXiv:2208.08064*, 2022.
- [9] David Deutsch. Quantum theory, the church–turing principle and the universal quantum computer. *Proceedings of the Royal Society of London. A. Mathematical and Physical Sciences*, 400(1818):97–117, 1985.

- [10] Peter W Shor. Polynomial-time algorithms for prime factorization and discrete logarithms on a quantum computer. *SIAM review*, 41(2):303–332, 1999.
- [11] Yasunobu Nakamura, Yu A Pashkin, and JS Tsai. Coherent control of macroscopic quantum states in a single-cooper-pair box. *nature*, 398(6730):786–788, 1999.
- [12] Denis Vion, A Aassime, Audrey Cottet, Pl Joyez, H Pothier, C Urbina, Daniel Esteve, and Michel H Devoret. Manipulating the quantum state of an electrical circuit. *Science*, 296(5569):886–889, 2002.
- [13] Jens Koch, Terri M. Yu, Jay Gambetta, Andrew A Houck, David I Schuster, Johannes Majer, Alexandre Blais, Michel H Devoret, Steven M Girvin, and Robert J Schoelkopf. Charge-insensitive qubit design derived from the cooper pair box. *Physical Review A*, 76(4):042319, 2007.
- [14] Rainer Blatt and David Wineland. Entangled states of trapped atomic ions. *Nature*, 453(7198):1008–1015, 2008.
- [15] Emanuel Knill, Raymond Laflamme, and Gerald J Milburn. A scheme for efficient quantum computation with linear optics. *nature*, 409(6816):46–52, 2001.
- [16] Juan M Arrazola, Ville Bergholm, Kamil Brádler, Thomas R Bromley, Matt J Collins, Ish Dhand, Alberto Fumagalli, Thomas Gerrits, Andrey Goussev, Lukas G Helt, et al. Quantum circuits with many photons on a programmable nanophotonic chip. *Nature*, 591(7848):54–60, 2021.
- [17] Mark Saffman, Thad G Walker, and Klaus Mølmer. Quantum information with rydberg atoms. *Reviews of modern physics*, 82(3):2313, 2010.
- [18] Antoine Browaeys and Thierry Lahaye. Many-body physics with individually controlled rydberg atoms. *Nature Physics*, 16(2):132–142, 2020.
- [19] Rutger Vrijen, Eli Yablonovitch, Kang Wang, Hong Wen Jiang, Alex Balandin, Vwani Roychowdhury, Tal Mor, and David DiVincenzo. Electron-spin-resonance transistors for quantum computing in silicon-germanium heterostructures. *Physical Review A*, 62(1):012306, 2000.

- [20] Jun Yoneda, Kenta Takeda, Tomohiro Otsuka, Takashi Nakajima, Matthieu R Delbecq, Giles Allison, Takumu Honda, Tetsuo Koderu, Shunri Oda, Yusuke Hoshi, et al. A quantum-dot spin qubit with coherence limited by charge noise and fidelity higher than 99.9%. *Nature nanotechnology*, 13(2):102–106, 2018.
- [21] Davide Castelvecchi. Ibm releases first-ever 1,000-qubit quantum chip. *Nature*, 624(7991):238–238, 2023.
- [22] Frank Arute, Kunal Arya, Ryan Babbush, Dave Bacon, Joseph C Bardin, Rami Barends, Rupak Biswas, Sergio Boixo, Fernando GSL Brandao, David A Buell, et al. Quantum supremacy using a programmable superconducting processor. *Nature*, 574(7779):505–510, 2019.
- [23] Rami Barends, Julian Kelly, Anthony Megrant, Andrzej Veitia, Daniel Sank, Evan Jeffrey, Ted C White, Josh Mutus, Austin G Fowler, Brooks Campbell, et al. Superconducting quantum circuits at the surface code threshold for fault tolerance. *Nature*, 508(7497):500–503, 2014.
- [24] Alexandre Blais, Arne L Grimsmo, Steven M Girvin, and Andreas Wallraff. Circuit quantum electrodynamics. *Reviews of Modern Physics*, 93(2):025005, 2021.
- [25] Alexandre Blais, Ren-Shou Huang, Andreas Wallraff, Steven M Girvin, and R Jun Schoelkopf. Cavity quantum electrodynamics for superconducting electrical circuits: An architecture for quantum computation. *Physical Review A*, 69(6):062320, 2004.
- [26] Thomas Niemczyk, F Deppe, H Huebl, EP Menzel, F Hocke, MJ Schwarz, JJ Garcia-Ripoll, D Zueco, T Hümmer, E Solano, et al. Circuit quantum electrodynamics in the ultrastrong-coupling regime. *Nature Physics*, 6(10):772–776, 2010.
- [27] Sal J Bosman, Mario F Gely, Vibhor Singh, Daniel Bothner, Andres Castellanos-Gomez, and Gary A Steele. Approaching ultrastrong coupling in transmon circuit qed using a high-impedance resonator. *Physical Review B*, 95(22):224515, 2017.

- [28] Neereja M Sundaresan, Yanbing Liu, Darius Sadri, László J Szócs, Devin L Underwood, Moein Malekakhlagh, Hakan E Türeci, and Andrew A Houck. Beyond strong coupling in a multimode cavity. *Physical Review X*, 5(2):021035, 2015.
- [29] Roman Kuzmin, Nitish Mehta, Nicholas Grabon, Raymond Mencia, and Vladimir E Manucharyan. Superstrong coupling in circuit quantum electrodynamics. *npj Quantum Information*, 5(1):20, 2019.
- [30] RK Naik, N Leung, S Chakram, Peter Groszkowski, Y Lu, Nathan Earnest, DC McKay, Jens Koch, and David I Schuster. Random access quantum information processors using multimode circuit quantum electrodynamics. *Nature Communications*, 8(1):1904, 2017.
- [31] J Ignacio Cirac and Peter Zoller. Goals and opportunities in quantum simulation. *Nature Physics*, 8(4):264–266, 2012.
- [32] Seiji Armstrong, Jean-François Morizur, Jiri Janousek, Boris Hage, Nicolas Treps, Ping Koy Lam, and Hans-A Bachor. Programmable multimode quantum networks. *Nature communications*, 3(1):1026, 2012.
- [33] VG Veselago. Electrodynamics of media with simultaneously negative electric permittivity and magnetic permeability. *Advances in Electromagnetics of Complex Media and Metamaterials*, pages 83–97, 2002.
- [34] George V Eleftheriades, Ashwin K Iyer, and Peter C Kremer. Planar negative refractive index media using periodically LC loaded transmission lines. *IEEE transactions on Microwave Theory and Techniques*, 50(12):2702–2712, 2002.
- [35] Christophe Caloz and Tatsuo Itoh. Transmission line approach of left-handed (LH) materials and microstrip implementation of an artificial LH transmission line. *IEEE Transactions on Antennas and Propagation*, 52(5):1159–1166, 2004.
- [36] H Wang, A.P. Zhuravel, S Indrajeet, Bruno G Taketani, M.D. Hutchings, Y Hao, F Rouxinol, FK Wilhelm, M.D. LaHaye, A.V. Ustinov, and B.L.T Plourde. Mode structure in superconducting metamaterial transmission-line resonators. *Physical Review Applied*, 11(5):054062, 2019.

- [37] S Indrajeet, H Wang, M.D. Hutchings, B.G. Taketani, Frank K Wilhelm, M.D. LaHaye, and B.L.T. Plourde. Coupling a superconducting qubit to a left-handed metamaterial resonator. *Physical Review Applied*, 14(6):064033, 2020.
- [38] Linbo Shao, Mengjie Yu, Smarak Maity, Neil Sinclair, Lu Zheng, Cleaven Chia, Amirhassan Shams-Ansari, Cheng Wang, Mian Zhang, Keji Lai, et al. Microwave-to-optical conversion using lithium niobate thin-film acoustic resonators. *Optica*, 6(12):1498–1505, 2019.
- [39] Anshuman Singh, Qing Li, Shunfa Liu, Ying Yu, Xiyuan Lu, Christian Schneider, Sven Höfling, John Lawall, Varun Verma, Richard Mirin, et al. Quantum frequency conversion of a quantum dot single-photon source on a nanophotonic chip. *Optica*, 6(5):563–569, 2019.
- [40] Hongliang Ren, Chang-Ling Zou, Jin Lu, Lin-Lin Xue, Shuqin Guo, Yali Qin, and Weisheng Hu. Highly sensitive intensity detection by a self-interference micro-ring resonator. *IEEE Photonics Technology Letters*, 28(13):1469–1472, 2016.
- [41] Tobias J Kippenberg, Alexander L Gaeta, Michal Lipson, and Michael L Gorodetsky. Dissipative kerr solitons in optical microresonators. *Science*, 361(6402):eaan8083, 2018.
- [42] Galan Moody, Volker J Sorger, Daniel J Blumenthal, Paul W Juodawlkis, William Loh, Cheryl Sorace-Agaskar, Alex E Jones, Krishna C Balram, Jonathan CF Matthews, Anthony Laing, et al. 2022 roadmap on integrated quantum photonics. *Journal of Physics: Photonics*, 4(1):012501, 2022.
- [43] Sumeru Hazra, Anirban Bhattacharjee, Madhavi Chand, Kishor V Salunkhe, Sriram Gopalakrishnan, Meghan P Patankar, and R Vijay. Ring-resonator-based coupling architecture for enhanced connectivity in a superconducting multiqubit network. *Physical Review Applied*, 16(2):024018, 2021.
- [44] M. H. Ansari. Superconducting qubits beyond the dispersive regime. *Physical Review B*, 100:024509, Jul 2019.

- [45] Farzan Jazaeri, Arnout Beckers, Armin Tajalli, and Jean-Michel Sallese. A review on quantum computing: From qubits to front-end electronics and cryogenic mosfet physics. In *2019 MIXDES-26th International Conference "Mixed Design of Integrated Circuits and Systems"*, pages 15–25. IEEE, 2019.
- [46] John Bardeen, Leon N Cooper, and John Robert Schrieffer. Theory of superconductivity. *Physical review*, 108(5):1175, 1957.
- [47] Michael Tinkham. *Introduction to superconductivity*. Courier Corporation, 2004.
- [48] John M Martinis, Michel H Devoret, and John Clarke. Quantum josephson junction circuits and the dawn of artificial atoms. *Nature Physics*, 16(3):234–237, 2020.
- [49] Vinay Ambegaokar and Alexis Baratoff. Tunneling between superconductors. *Physical Review Letters*, 10(11):486, 1963.
- [50] John Clarke. Squid fundamentals. In *SQUID sensors: fundamentals, fabrication and applications*, pages 1–62. Springer, 1996.
- [51] M.D. Hutchings, Jared B Hertzberg, Yebin Liu, Nicholas T Bronn, George A Keefe, Markus Brink, J.M. Chow, and B.L.T. Plourde. Tunable superconducting qubits with flux-independent coherence. *Physical Review Applied*, 8(4):044003, 2017.
- [52] Alexandre Blais, Jay Gambetta, Andreas Wallraff, David I Schuster, Steven M Girvin, Michel H Devoret, and Robert J Schoelkopf. Quantum-information processing with circuit quantum electrodynamics. *Physical Review A*, 75(3):032329, 2007.
- [53] Frederick Williams Cummings. Comparison of quantum and semiclassical radiation theories with application to the beam maser. *Ph. D. Thesis*, 1962.
- [54] Martin Göppl, A Fragner, M Baur, R Bianchetti, Stefan Filipp, Johannes M Fink, Peter J Leek, G Puebla, L Steffen, and Andreas Wallraff. Coplanar waveguide resonators for circuit quantum electrodynamics. *Journal of Applied Physics*, 104(11), 2008.

- [55] David M Pozar. *Microwave engineering*. John wiley & sons, 2011.
- [56] Koki Watanabe, Keiji Yoshida, and Takeshi Aoki Kohjiro. Kinetic inductance of superconducting coplanar waveguides. *Japanese journal of applied physics*, 33(10R):5708, 1994.
- [57] Thomas H Lee. *Planar microwave engineering: a practical guide to theory, measurement, and circuits*, volume 1. Cambridge university press, 2004.
- [58] Irfan Siddiqi. Engineering high-coherence superconducting qubits. *Nature Reviews Materials*, 6(10):875–891, 2021.
- [59] Chen Wang, Christopher Axline, Yvonne Y Gao, Teresa Brecht, Yiwen Chu, Luigi Frunzio, MH Devoret, and Robert J Schoelkopf. Surface participation and dielectric loss in superconducting qubits. *Applied Physics Letters*, 107(16), 2015.
- [60] Brooks Foxen, Charles Neill, Andrew Dunsworth, Pedram Roushan, Ben Chiaro, Anthony Megrant, Julian Kelly, Zijun Chen, Kevin Satzinger, Rami Barends, et al. Demonstrating a continuous set of two-qubit gates for near-term quantum algorithms. *Physical Review Letters*, 125(12):120504, 2020.
- [61] Abhinav Kandala, Ken X Wei, Srikanth Srinivasan, Easwar Magesan, S Carnevale, GA Keefe, D Klaus, O Dial, and DC McKay. Demonstration of a high-fidelity cnot gate for fixed-frequency transmons with engineered z z suppression. *Physical Review Letters*, 127(13):130501, 2021.
- [62] Zhiyuan Li, Pei Liu, Peng Zhao, Zhenyu Mi, Huikai Xu, Xuehui Liang, Tang Su, Weijie Sun, Guangming Xue, Jing-Ning Zhang, et al. Error per single-qubit gate below 10^{-4} in a superconducting qubit. *arXiv preprint arXiv:2302.08690*, 2023.
- [63] Tsuyoshi Yamamoto, Yu A Pashkin, Oleg Astafiev, Yasunobu Nakamura, and Jaw-Shen Tsai. Demonstration of conditional gate operation using superconducting charge qubits. *Nature*, 425(6961):941–944, 2003.

- [64] JB Majer, FG Paauw, ACJ Ter Haar, CJPM Harmans, and JE Mooij. Spectroscopy on two coupled superconducting flux qubits. *Physical review letters*, 94(9):090501, 2005.
- [65] BLT Plourde, J Zhang, KB Whaley, FK Wilhelm, TL Robertson, T Hime, S Linzen, PA Reichardt, C-E Wu, and John Clarke. Entangling flux qubits with a bipolar dynamic inductance. *Physical Review B*, 70(14):140501, 2004.
- [66] Travis Hime, PA Reichardt, BLT Plourde, TL Robertson, C-E Wu, AV Ustinov, and John Clarke. Solid-state qubits with current-controlled coupling. *science*, 314(5804):1427–1429, 2006.
- [67] Fei Yan, Philip Krantz, Youngkyu Sung, Morten Kjaergaard, Daniel L Campbell, Terry P Orlando, Simon Gustavsson, and William D Oliver. Tunable coupling scheme for implementing high-fidelity two-qubit gates. *Physical Review Applied*, 10(5):054062, 2018.
- [68] Daniel L Campbell, Archana Kamal, Leonardo Ranzani, Michael Senatore, and Matthew D LaHaye. Modular tunable coupler for superconducting circuits. *Physical Review Applied*, 19(6):064043, 2023.
- [69] Johannes Majer, JM Chow, JM Gambetta, Jens Koch, BR Johnson, JA Schreier, L Frunzio, DI Schuster, Andrew Addison Houck, Andreas Wallraff, et al. Coupling superconducting qubits via a cavity bus. *Nature*, 449(7161):443–447, 2007.
- [70] Robert McDermott, RW Simmonds, Matthias Steffen, Ken B Cooper, Katarina Cicak, KD Osborn, Seongshik Oh, David P Pappas, and John M Martinis. Simultaneous state measurement of coupled josephson phase qubits. *Science*, 307(5713):1299–1302, 2005.
- [71] Andreas Dewes, Florian R Ong, Vivien Schmitt, R Lauro, N Boulant, P Bertet, D Vion, and D Esteve. Characterization of a two-transmon processor with individual single-shot qubit readout. *Physical review letters*, 108(5):057002, 2012.

- [72] Leonardo DiCarlo, Jerry M Chow, Jay M Gambetta, Lev S Bishop, Blake R Johnson, DI Schuster, J Majer, Alexandre Blais, Luigi Frunzio, SM Girvin, et al. Demonstration of two-qubit algorithms with a superconducting quantum processor. *Nature*, 460(7252):240–244, 2009.
- [73] Sarah Sheldon, Easwar Magesan, J.M. Chow, and J.M. Gambetta. Procedure for systematically tuning up cross-talk in the cross-resonance gate. *Physical Review A*, 93(6):060302, 2016.
- [74] Easwar Magesan and Jay M Gambetta. Effective hamiltonian models of the cross-resonance gate. *Physical Review A*, 101(5):052308, 2020.
- [75] Pranav Mundada, Gengyan Zhang, Thomas Hazard, and Andrew Houck. Suppression of qubit crosstalk in a tunable coupling superconducting circuit. *Physical Review Applied*, 12(5):054023, 2019.
- [76] X Li, T Cai, H Yan, Z Wang, X Pan, Y Ma, W Cai, J Han, Z Hua, X Han, et al. Tunable coupler for realizing a controlled-phase gate with dynamically decoupled regime in a superconducting circuit. *Physical Review Applied*, 14(2):024070, 2020.
- [77] Jaseung Ku, Xuexin Xu, Markus Brink, David C McKay, Jared B Hertzberg, Mohammad H. Ansari, and B.L.T Plourde. Suppression of unwanted ZZ interactions in a hybrid two-qubit system. *Physical Review Letters*, 125(20):200504, 2020.
- [78] Xuexin Xu and M.H. Ansari. ZZ freedom in two-qubit gates. *Physical Review Applied*, 15:064074, Jun 2021.
- [79] Jerry Moy Chow. *Quantum information processing with superconducting qubits*. Yale University, 2010.
- [80] Jason Valentine, Shuang Zhang, Thomas Zentgraf, Erick Ulin-Avila, Dentcho A Genov, Guy Bartal, and Xiang Zhang. Three-dimensional optical metamaterial with a negative refractive index. *nature*, 455(7211):376–379, 2008.

- [81] Zhengyou Liu, Xixiang Zhang, Yiwei Mao, YY Zhu, Zhiyu Yang, Che Ting Chan, and Ping Sheng. Locally resonant sonic materials. *science*, 289(5485):1734–1736, 2000.
- [82] Xiaoyu Zheng, Howon Lee, Todd H Weisgraber, Maxim Shusteff, Joshua DeOtte, Eric B Duoss, Joshua D Kuntz, Monika M Biener, Qi Ge, Julie A Jackson, et al. Ultralight, ultrastiff mechanical metamaterials. *Science*, 344(6190):1373–1377, 2014.
- [83] Andrew Zangwill. *Modern electrodynamics*. Cambridge University Press, 2013.
- [84] Viktor G Veselago. Reviews of topical problems: the electrodynamics of substances with simultaneously negative values of ϵ and μ . *Soviet Physics Uspekhi*, 10(4):R04, 1968.
- [85] John David Jackson. *Classical electrodynamics*, 1999.
- [86] Richard A Shelby, David R Smith, and Seldon Schultz. Experimental verification of a negative index of refraction. *science*, 292(5514):77–79, 2001.
- [87] Javier Puertas Martínez, Sébastien Léger, Nicolas Gheeraert, Rémy Dassonneville, Luca Planat, Farshad Foughi, Yuriy Krupko, Olivier Buisson, Cécile Naud, Wiebke Hasch-Guichard, et al. A tunable josephson platform to explore many-body quantum optics in circuit-qed. *npj Quantum Information*, 5(1):19, 2019.
- [88] Mohammad Mirhosseini, Eunjong Kim, Vinicius S Ferreira, Mahmoud Kalaei, Alp Sipahigil, Andrew J Keller, and Oskar Painter. Superconducting metamaterials for waveguide quantum electrodynamics. *Nature communications*, 9(1):3706, 2018.
- [89] Daniel J Egger and Frank K Wilhelm. Multimode circuit quantum electrodynamics with hybrid metamaterial transmission lines. *Physical review letters*, 111(16):163601, 2013.
- [90] Wenhui Huang, Yuxuan Zhou, Ziyu Tao, Libo Zhang, Song Liu, Yuanzhen Chen, Tongxing Yan, and Dapeng Yu. A superconducting coplanar waveguide

- ring resonator as quantum bus for circuit quantum electrodynamics. *Applied Physics Letters*, 118(18):184001, 2021.
- [91] Michael C Ricci and Steven M Anlage. Single superconducting split-ring resonator electrodynamics. *Applied physics letters*, 88(26), 2006.
- [92] Neil W Ashcroft and N David Mermin. *Solid state physics*. Cengage Learning, 2022.
- [93] James Wenner, Matthew Neeley, Radoslaw C Bialczak, Michael Lenander, Erik Lucero, Aaron D O’Connell, Daniel Sank, Haohua Wang, Martin Weides, Andrew N Cleland, et al. Wirebond crosstalk and cavity modes in large chip mounts for superconducting qubits. *Superconductor Science and Technology*, 24(6):065001, 2011.
- [94] T McBroom-Carroll, A Schlaves, X Xu, J Ku, B Cole, S Indrajeet, MD LaHaye, MH Ansari, and BLT Plourde. Entangling interactions between artificial atoms mediated by a multimode left-handed superconducting ring resonator. *arXiv preprint arXiv:2307.15695*, 2023.
- [95] Rami Barends, James Wenner, Michael Lenander, Yu Chen, Radoslaw C Bialczak, Julian Kelly, Erik Lucero, Peter O’Malley, Matteo Mariantoni, Daniel Sank, et al. Minimizing quasiparticle generation from stray infrared light in superconducting quantum circuits. *Applied Physics Letters*, 99(11):113507, 2011.
- [96] David Isaac Schuster. *Circuit quantum electrodynamics*. Yale University, 2007.
- [97] L S Cederbaum, J Schirmer, and H D Meyer. Block diagonalisation of hermitian matrices. *Journal of Physics A: Mathematical and General*, 22(13):2427, 1989.
- [98] Xuexin Xu and M.H. Ansari. Parasitic-free gate: An error-protected cross-resonance switch in weakly tunable architectures. *Physical Review Applied*, 19:024057, Feb 2023.
- [99] Michele C Collodo, Johannes Herrmann, Nathan Lacroix, Christian Kraglund Andersen, Ants Remm, Stefania Lazar, Jean-Claude Besse, Theo Walter, Andreas Wallraff, and Christopher Eichler. Implementation of conditional

- phase gates based on tunable ZZ interactions. *Physical Review Letters*, 125(24):240502, 2020.
- [100] Ming Hua, Ming-Jie Tao, Fu-Guo Deng, and Gui Lu Long. One-step resonant controlled-phase gate on distant transmon qutrits in different 1D superconducting resonators. *Scientific Reports*, 5(1):14541, 2015.
- [101] Eyob A Sete, Angela Q Chen, Riccardo Manenti, Shobhan Kulshreshtha, and Stefano Poletto. Floating tunable coupler for scalable quantum computing architectures. *Physical Review Applied*, 15(6):064063, 2021.
- [102] Yuan Xu, Ji Chu, Jiahao Yuan, Jiawei Qiu, Yuxuan Zhou, Libo Zhang, Xinsheng Tan, Yang Yu, Song Liu, Jian Li, et al. High-fidelity, high-scalability two-qubit gate scheme for superconducting qubits. *Physical Review Letters*, 125(24):240503, 2020.
- [103] J Stehlik, DM Zajac, DL Underwood, T Phung, J Blair, S Carnevale, D Klaus, GA Keefe, A Carniol, Muir Kumph, et al. Tunable coupling architecture for fixed-frequency transmon superconducting qubits. *Physical Review Letters*, 127(8):080505, 2021.
- [104] Petar Jurcevic, Ali Javadi-Abhari, Lev S Bishop, Isaac Lauer, Daniela F Bogorin, Markus Brink, Lauren Capelluto, Oktay Günlük, Toshinari Itoko, Naoki Kanazawa, et al. Demonstration of quantum volume 64 on a superconducting quantum computing system. *Quantum Science and Technology*, 6(2):025020, 2021.

Tianna (McBroom) Carroll

Columbia, MD | tianna.mcbroom@gmail.com

EDUCATION

Syracuse University

PhD, Physics

- Research Excellence Doctoral Fellowship, 2020

Syracuse, NY

August 2018 – Present

University of Missouri – St. Louis

BS, Physics

- Minor in Mathematics
- GPA: 4.0
- Summa Cum Laude, with Honors and Distinction
- Student Marshall for the College of Arts & Science

St. Louis, MO

August 2014 — May 2018

PUBLICATIONS

McBroom-Carroll, T., Schlages, A., Xu, X., Ku, J., Cole, B., Indrajeet, S., LaHaye, M.D., Ansari, M. H., Plourde, B. L. T. (2023) *Entangling interactions between artificial atoms mediated by a multimode left-handed superconducting ring resonator*. ArXiv:2307.15695. Accepted.

Liu, C-H, Ballard, A., Olaya, D., Schmidt D. R., Biesecker, J., Lucas, T., Ullom J., Patel, S., Rafferty, O., Opremack, A., Dodge, K., Iaia, V., **McBroom, T.**, et al. (2023) *Single Flux Quantum-Based Digital Control of Superconducting Qubits in a Multi-Chip Module*. PRX Quantum 4, 030310.

Osborn, D., **McBroom, T.**, and Fraundorf, P. (2017). *Sensitivity of TEM data on lightspeed to camera-length's voltage variation*. Microscopy and Microanalysis, 23(S1), 2308-2309.

EXPERIENCE

Graduate Dissertation Research: Quantum computing

Syracuse University

Supervisor: Professor Britton Plourde

- Focus: Characterizing interactions between qubits and multimode metamaterial resonators with left-handed dispersion

Fall 2019 – Present

Syracuse, NY

Graduate Research Assistant: Laser power converters

Syracuse University

Supervisor: Professor Eric Schiff

- Focus: Enhancing photon recycling via optical coating in GaAs laser power converters

Spring 2018 – Fall 2020

Syracuse, NY

Undergraduate Research Assistant: Hydrogen storage

University of Missouri – St. Louis

Supervisor: Professor Eric Mazjoub

Summer 2017 – Summer 2018

St. Louis, MO

- Focus: Investigate properties of silicon-based complex hydrides using density functional theory calculations

Acquisitions Intern

Summer 2018 – Summer 2020

National Geospatial Intelligence Agency

St. Louis, MO

Supervisor: Paul Vento

- Performed data analysis, earned value management (EVM)
- Assisted with launch of competitive contracts, coordinated and communicated with contractors

Student Coordinator of Astronomy Outreach

Fall 2016 – Winter 2018

University of Missouri – St. Louis

St. Louis, MO

Supervisor: Bruce Wilking

- Organized, designed, and orchestrated planetarium shows
- Presented physics demonstrations for grade school students
- [See article](#)

Statistical Analysis Intern

Summer 2016

Eurofins Bioanalytics

St. Louis, MO

Supervisor: Jennifer Walsh

VOLUNTEER EXPERIENCE

Volunteer Science Educator

August 2015 – August 2017

St. Louis Science Center

St. Louis, MO

- Assisted with planetarium shows
- Designed and performed science demonstrations